

UNIVERSITY OF BELGRADE
FACULTY OF TECHNOLOGY AND METALLURGY

Asma Juma Albrbar

**Synthesis and characterization of nanostructured
photocatalysts based on the nitrogen- and sulfur-doped titania
for the water pollutants degradation under visible light**

Doctoral Dissertation

Belgrade, 2017

UNIVERZITET U BEOGRADU
TEHNOLOŠKO-METALURŠKI FAKULTET

Asma Juma Albrbar

**Sinteza i karakterizacija nanostrukturnih fotokatalizatora na
bazi azotom i sumporom dopiranog titan(IV)-oksida za
razgradnju zagađujućih supstanci u vodi pod dejstvom
vidljive svetlosti**

doktorska disertacija

Beograd, 2017.

Supervisor

**Dr Rada Petrović, Full Professor, Faculty of
Technology and Metallurgy,
University of Belgrade, Belgrade**

Committee Members

**1. dr Đorđe Janačković, Full Professor, Faculty of
Technology and Metallurgy,
University of Belgrade, Belgrade**

**2. dr Jelena Miladinovic, Full Professor, Faculty of
Technology and Metallurgy
University of Belgrade, Belgrade**

**3. dr Veljko Đokić, Research Associate, Innovation center,
Faculty of Technology and Metallurgy,
University of Belgrade, Belgrade**

Date of Defense:

Acknowledgments

First, I wish to express my gratitude to God and to thank Him for giving me enough wisdom and strength to successfully complete this thesis.

I would like to express my sincere gratitude to my advisor Prof. Dr. Rada Petrović for her continuous support during my Ph.D studies and research, for her patience, motivation, enthusiasm, and immense knowledge. Her guidance helped me through the time of research and writing of this thesis.

I would like to thank Prof. Dr. Jelena Miladinovic for her help during the thesis completion and also to all the Professors and Doctors from whom I gained knowledge. Also, thanks go to all the colleagues from my internship for their wonderful support and collaboration and special thanks are going to Veljko and Andjelika for assisting and helping me in the analysis and work on this thesis.

Furthermore, I would also like to thank my parents for their love, prayer and never-ending support and encouraging me all the time.

Word fail me to express my appreciation to my husband Abdusalam and to my children Yousef, Porog and Lamia for their patience, understanding and love during the whole period, thanks a lot for everything.

Thanks go to my sisters and brothers and to all of my friends. They were always supporting me with their best wishes.

Finally, I am very grateful to all the Department members that I have met, for their valuable suggestions and comments and also for their friendship.

Asma Juma Albrbar

Synthesis and characterization of nanostructured photocatalysts based on the nitrogen- and sulfur-doped titania for the water pollutants degradation under visible light

Abstract

A nonmetal-doped titania has attracted considerable attention in recent years due to its photocatalytic activity in the visible part of the solar spectrum, which is beneficial with regards to pure TiO₂. Among the explored nonmetal dopants, nitrogen and sulfur have been shown to be the most promising for the enhancement of photocatalytic activity of TiO₂ under visible light. These nonmetals can be introduced to the TiO₂ lattice by employing various precursors and preparation methods.

In this dissertation, non-hydrolytic sol–gel method coupled with solvothermal treatment, starting from titanium(IV) chloride and titanium(IV) isopropoxide dissolved in different aprotic solvents, was applied for the synthesis of undoped and N,S-doped titania photocatalysts. The photocatalytic efficiency of the synthesized titania powders was tested by measuring the photocatalytic degradation of the azo dye C.I. Reactive Orange 16, under UV or visible light. The efficiency of undoped powder, synthesized by using carbon tetrachloride and by gel annealing in air at 500 °C for 3 h, was investigated in different types of water in comparison to the efficiency of commercial photocatalyst P25, under UV light. Undoped powders were synthesized also by using chloroform and cyclohexane, and annealing at different temperatures was applied to achieve the best performances of the photocatalyst and to avoid using of toxic solvent for the synthesis. For doping by sulfur, solvent dimethyl sulfoxide (DMSO) was used, while annealing of gel or powder in ammonia or ammonia/air mixture at 500 °C for 3 h was applied for N-doping. The ammonia-treated powders were post-annealed in air at different conditions to attain the best visible-light activity.

The efficiency of undoped titania, synthesized by using CCl₄ as a solvent, was slightly better than the efficiency of a standard TiO₂ powder Degusa P25, under UV irradiation, in deionized water, as well as in saline waters. Both photocatalysts had significantly lower efficiency in natural and artificial seawater than in deionized water.

Photodegradation rate constant for these photocatalysts, obtained from the dependence of the initial degradation rate on the initial dye concentration, had similar values in all types of water due to similar properties of the photocatalysts. According to the textural properties, crystallite sizes, morphology and photocatalytic efficiency of the powders obtained by using carbon tetrachloride, chloroform, or cyclohexane, it was concluded that type of aprotic solvent had no influence on the titania properties if the solvents are of similar boiling points.

Significant S-doping was achieved by using DMSO as a solvent, where S(IV+) and/or S(VI+) substituted Ti^{4+} . However, this substitution caused a very small band-gap narrowing and just slightly better visible-light activity in comparison to the undoped titania. Doping with nitrogen provided a much better photocatalytic activity than the S-doping, regardless of the lower quantity of incorporated nitrogen. It was shown that annealing of the gel in ammonia flow was much more efficient way for nitrogen incorporation in the TiO_2 structure than the annealing of crystalline titania powder. The XPS analysis revealed that nitrogen was incorporated interstitially in the titania structure as N^{3-} anion. Post-annealing in air of the samples obtained by annealing in ammonia or ammonia/air mixture was necessary in order to achieve a good visible-light activity. Treatment in static air atmosphere at 400 °C for 30 min was determined as the optimal for the post-annealing. The highest photocatalytic activity under visible light was achieved with N,S-co-doped titania, as a result of high specific surface area, appropriate mesoporosity and efficient N,S-co-doping.

Keywords: Titania, Non-hydrolytic sol-gel method, Aprotic solvents, Mesoporosity, Annealing, Photocatalysis, UV light, N-doping, Ammonia, S-doping, Dimethyl sulfoxide, N,S-co-doping, Visible-light activity, C.I. Reactive Orange 16, Textural properties, XPS, Optical properties.

Scientific field: Technical engineering

Major in: Chemical engineering

UDC number: 620.3:544.526.5:546.17:546.22:546.82:628.196

Sinteza i karakterizacija nanostrukturnih fotokatalizatora na bazi azotom i sumporom dopiranog titan(IV)-oksida za razgradnju zagađujućih supstanci u vodi pod dejstvom vidljive svetlosti

Izvod

Dopiranjem titan(IV)-oksida nemetalima omogućuje se fotokatalitička aktivnost pod dejstvom vidljive svetlosti, što predstavlja veliku prednost dopiranog u odnosu na čist TiO_2 . Najznačajniji nemetalni dopanti su azot i sumpor, koji se mogu inkorporirati u strukturu TiO_2 primenom različitih prekursora i postupaka sinteze.

U ovoj disertaciji je za sintezu fotokatalizatora na bazi nedopiranog i N,S-dopiranog TiO_2 primenjen nehidrolitički sol-gel postupak u kombinaciji sa solvotermalnim tretmanom, polazeći od titan(IV)-hlorida i titan(IV)-izopropoksida u različitim neprotionskim rastvaračima. Fotokatalitička efikasnost sintetisanih prahova je ispitana merenjem stepena fotokatalitičke razgradnje azo-boje C.I. Reactive Orange 16, pod dejstvom UV zračenja ili vidljive svetlosti. Efikasnost nedopiranog praha, koji je sintetisan korišćenjem ugljenik(IV)-hlorida i kalcinacijom dobijenog gela na $500\text{ }^\circ\text{C}$ u toku 3 h, je ispitivana u različitim vrstama vode, u poređenju sa efikasnošću komercijalnog fotokatalizatora P25, pod dejstvom UV zračenja. Nedopirani prahovi su takođe sintetisani korišćenjem hloroforma i cikloheksana, pri čemu su gelovi kalcinisani na različitim temperaturama, da bi se postigla najbolja fotokatalitička efikasnost i izbeglo korišćenje toksičnih rastvarača. Za dopiranje sumporom korišćen je rastvarač dimetil-sulfoksid (DMSO), dok je dopiranje azotom izvedeno kalcinacijom gelova ili kristalnog TiO_2 praha u struji amonijaka ili mešavine amonijaka i vazduha, na $500\text{ }^\circ\text{C}$ u toku 3 h. Prahovi kalcinisani u atmosferi amonijaka su naknadno kalcinisani u atmosferi vazduha, pri različitim uslovima, da bi se obezbedila najbolja aktivnost prahova pod dejstvom vidljive svetlosti.

Efikasnost nedopiranog TiO_2 , sintetizovanog korišćenjem CCl_4 kao rastvarača, je nešto veća od efikasnosti standardnog fotokatalizatora Degusa P25, pod dejstvom UV zračenja, u dejonizovanoj vodi, kao i u slanim vodama. Efikasnost oba fotokatalizatora je bila značajno manja u slanim vodama nego u dejonizovanoj vodi. Konstanta brzine fotokatalitičke razgradnje, određena iz zavisnosti početne brzine razgradnje od početne

koncentracije boje, je bila približno ista u svim tipovima vode, zahvaljujući sličnim svojstvima fotokatalizatora. Na osnovu teksturalnih svojstava, veličine kristalita, morfologije i fotokatalitičke efikasnosti prahova koji su sintetisani korišćenjem ugljenik(IV)-hlorida, hloroforma ili cikloheksana zaključeno je da vrsta neprotonskog rastvarača nema bitnog uticaja na svojstva sintetisanog praha ako su tačke ključanja rastvarača približno iste.

Korišćenjem DMSO kao rastvarača postignuto je značajno dopiranje TiO_2 sumporom, pri čemu je Ti^{4+} zamenjen četvorovalentnim i/ili šestovalentnim sumporom. Međutim, ova supstitucija je dovela do veoma malog sužavanja zabranjene zone i malog povećanja fotokatalitičke efikasnosti pod dejstvom vidljive svetlosti u poređenju sa nedopiranim TiO_2 . Dopiranje azotom je obezbedilo mnogo bolju aktivnost TiO_2 pod dejstvom vidljive svetlosti nego dopiranje sumporom, bez obzira na manji stepen dopiranja. Pokazano je da je kalcinacija gela u struji amonijaka mnogo efikasniji način inkorporiranja azota u strukturu TiO_2 nego kalcinacija kristalnog praha. XPS analiza je pokazala da je azot inkorporiran intersticijski, kao N^{3-} anjon. Post-kalcinacija u vazduhu prahova koji su dobijeni kalcinacijom u struji amonijaka ili mešavine amonijaka i vazduha je bila neophodna da bi se postigla dobra aktivnost pod dejstvom vidljive svetlosti. Utvrđeno je da su optimalni uslovi post-kalcinacije tretman u statičkoj atmosferi vazduha na $400\text{ }^\circ\text{C}$ u toku 30 min. Najveća fotokatalitička aktivnost pod dejstvom vidljive svetlosti je postignuta u slučaju istovremenog dopiranja azotom i sumporom, zahvaljujući velikoj specifičnoj površini dobijenog praha, odgovarajućoj mezoporoznosti i efikasnom istovremenom N,S-dopiranju.

Ključne reči: Titan(IV)-oksid, nehidrolitički sol-gel postupak, neprotonski rastvarači, mezoporoznost, kalcinacija, fotokataliza, UV zračenje, N-dopiranje, amonijak, S-dopiranje, Dimetil sulfoksid (DMSO), N,S-kodopiranje, Aktivnost pod dejstvom vidljive svetlosti, C.I. Reactive Orange 16, Teksturalna svojstva, XPS, Optička svojstva.

Naučna oblast: Tehnološko inženjerstvo

Uža naučna oblast: Hemijsko inženjerstvo

UDC broj: 620.3:544.526.5:546.17:546.22:546.82:628.196

List of Figures

Figure 1. Mechanism of semiconductor photocatalysis	5
Figure 2. Band positions of several semiconductors in contact with aqueous electrolyte at pH 1 (red colour - the lower edge of the conduction band, green colour - upper edge of the valence band)	7
Figure 3. Crystalline structures of anatase and rutile. The bond length and angles of the octahedrally coordinated Ti atoms are indicated and the stacking of the octahedral in both structures is shown on the right side	9
Figure 4. Schematic illustration for energetics and primary reaction mechanism of TiO ₂ photocatalysis	12
Figure 5. The dependence of photocatalytic reaction rate on: a) light wavelength, b) light intensity	17
Figure 6. Energy states in TiO ₂ after being doped by Fe, Cr and V ions	30
Figure 7. Mechanisms of non-metal doped TiO ₂ photocatalysis	32
Figure 8. The possible origin of visible light absorption in doped TiO ₂ by non-metal doping	34
Figure 9. Substitutional (a) and interstitial (b) incorporation of nitrogen in TiO ₂ lattice	34
Figure 10. Electronic band structure for: a) pure anatase, b) substitutional N-doped anatase, and c) interstitial N-doped anatase TiO ₂	35
Figure 11. Electronic band schematics of photocatalytic degradation of benzene for substitutional N-TiO ₂ (A), pure TiO ₂ (B) and interstitial N-TiO ₂	40
Figure 12. Electronic structure of Ti _{1-x} S _x O _{2-y} N _y	45
Figure 13. The structure of dye C.I. Reactive Orange 16	48
Figure 14. Experimental set-up used for the photodegradation of RO16 under: (a) UV light. (b) visible light	56
Figure 15. Scanning electron micrographs (SEM) of: a) P160/500 and b) P25	59
Figure 16. Photocatalytic degradation of dye RO16 by P25 powder in: a) DIW, b) NSW and c) ASW (UV irradiation at room temperature; P25 concentration was 1 g dm ⁻³). The corresponding linear plots of the photocatalytic decolorization kinetics are given in the insets	60

- Figure 17.** Photocatalytic degradation of dye RO16 by P160/500 powder in: a) DIW, b) NSW and c) ASW (UV irradiation at room temperature; P160 concentration was 1 g dm^{-3}). The corresponding linear plots of the photocatalytic decolorization kinetics are given in the insets **61**
- Figure 18.** Effect of initial RO16 dye concentration on its initial photodegradation rate with: a) P25 and b) P160/500 in DIW, NSW and ASW (UV irradiation at room temperature; RO16 concentration was in the range of $20 - 80 \text{ mg dm}^{-3}$; TiO_2 concentration was 1 g dm^{-3}) **66**
- Figure 19.** XRD patterns of TiO_2 powders synthesized using CCl_4 , annealed at different temperatures **68**
- Figure 20.** XRD patterns of TiO_2 powders synthesized using CHCl_3 , annealed at different temperatures **69**
- Figure 21.** XRD patterns of TiO_2 powders synthesized using C_6H_{12} , annealed at different temperatures **69**
- Figure 22.** a) N_2 adsorption-desorption isotherms, b) pore size distribution of TiO_2 powders synthesized using CCl_4 **71**
- Figure 23.** a) N_2 adsorption-desorption isotherms, b) pore size distribution of TiO_2 powders synthesized using CHCl_3 **71**
- Figure 24.** a) N_2 adsorption-desorption isotherms, b) pore size distribution of TiO_2 powders synthesized using C_6H_{12} **72**
- Figure 25.** SEM micrographs of TiO_2 powders: (a) P160/500(CCl_4), (b) P160/500(CHCl_3), (c) P160/500(C_6H_{12}) **74**
- Figure 26.** Adsorption and photocatalytic degradation of RO16 dye under UV light irradiation in the presence of the powders synthesized by using CCl_4 , CHCl_3 and C_6H_{12} annealed at: a) $350 \text{ }^\circ\text{C}$, b) $400 \text{ }^\circ\text{C}$ and c) $500 \text{ }^\circ\text{C}$ **75**
- Figure 27.** Photocatalytic degradation of RO16 dye under UV light irradiation in the presence of the powders synthesized by using CCl_4 , CHCl_3 and C_6H_{12} annealed at: a) $350 \text{ }^\circ\text{C}$, b) $400 \text{ }^\circ\text{C}$ and c) $500 \text{ }^\circ\text{C}$ **76**
- Figure 28.** Photocatalytic efficiency of undoped powder P160/500(C_6H_{12}), N- TiO_2 powders obtained at different post-annealing conditions and powder obtained without post-annealing **79**

Figure 29. Plot of UV–Vis diffuse reflectance spectra (a) and Tauc plots (b) for the N-TiO ₂ powders obtained at different post-annealing conditions in static air atmosphere	80
Figure 30. SEM micrographs of the powders: a) obtained by G160(C ₆ H ₁₂) calcination in ammonia at 500 °C for 3 h, without post-annealing b) P160DN/350(30min), c) P160DN/400(30min) and d) P160DN/450(30min)	81
Figure 31. The efficiency of N-TiO ₂ powders obtained by post-annealing at 400 °C in static and dynamic air atmosphere	82
Figure 32. The visible-light activity of N-TiO ₂ powders obtained by annealing in air/NH ₃ mixtures at 500 °C and post-annealed at 400	83
Figure 33 XRD patterns of theTiO ₂ powders	85
Figure 34. a) N ₂ adsorption-desorption isotherms, b) pore size distribution of TiO ₂ powders	87
Figure 35. SEM images of the samples: a) P160DN and b) P160PDN	88
Figure 36. SEM images of the samples: a) P200DS and b) P200DNS	89
Figure 37. TEM and HRTEM images of samples: P160 (a, e), P160DN (b, f), P160PDN (c, g) and P200DNS (d, h)	90
Figure 38. XPS survey spectra from the sample P200DNS	91
Figure 39. XPS spectra of: a) S 2p from P200DS and P200DNS, b) N 1s from P160DN and P200DNS, where the curve fittings are shown as dashed lines	92
Figure 40 XPS spectra of Ti 2p from all the TiO ₂ powders	94
Figure 41. FTIR spectra of the TiO ₂ powders	96
Figure 42 Plot of UV–Vis diffuse reflectance spectra (a) and Tauc plots (b) for the TiO ₂ powders	97
Figure 43 Photocatalytic degradation of dye C.I. Reactive Orange 16 in the presence of TiO ₂ powders	99

List of Tables

Table 1. Standard electrochemical reduction potentials of common oxidants	6
Table 2. The general characteristics of dye C.I. Reactive Orange 16 (λ_{\max} - the wavelength of the most intense UV/Vis absorption, M_w – molecular weight)	48
Table 3. Ionic composition of NSW	49
Table 4. The k_{app} values of photodegradation of RO16 by P25 and P160/500 in DIW depending on the initial dye concentration (UV irradiation at room temperature; TiO_2 concentration was 1 g dm^{-3})	62
Table 5. The k_{app} values of photodegradation of RO16 by P25 and P160/500 in NSW depending on the initial dye concentration (UV irradiation at room temperature; TiO_2 concentration was 1 g dm^{-3})	62
Table 6. The k_{app} values of photodegradation of RO16 by P25 and P160/500 in ASW depending on the initial dye concentration (UV irradiation at room temperature; TiO_2 concentration was 1 g dm^{-3})	63
Table 7. The parameters k and K obtained by fitting the experimental data of the photocatalytic dye degradation by P25 and P160/500 in DIW, SW and ASW (UV irradiation at room temperature; RO16 concentration was in the range of 20 - 80 mg dm^{-3} ; TiO_2 concentration was 1 g dm^{-3})	67
Table 8. Crystallites sizes of TiO_2 powders	70
Table 9. Textural characteristics TiO_2 powders synthesized using CCl_4	72
Table 10. Textural characteristics TiO_2 powders synthesized using CHCl_3	72
Table 11. Textural characteristics TiO_2 powders synthesized using C_6H_{12}	73
Table 12. The k_{app} values of photocatalytic degradation of RO16 dye under UV light irradiation by the powders synthesized by using CCl_4 , CHCl_3 and C_6H_{12} annealed at: a) 350 °C, b) 400 °C and c) 500 °C	76
Table 13 The experimental conditions for the TiO_2 samples preparation	84
Table 14 Crystallite sizes of TiO_2 powders	85
Table 15 Textural properties of TiO_2 powders	87

CONTENT

1. Introduction	1
2. Heterogeneous photocatalysis	4
2.1. Fundamentals of heterogeneous photocatalysis	4
2.2. Structure and photocatalytic properties of titania	8
2.2.1. <i>Structure of titania</i>	8
2.2.2. <i>Photocatalytic properties of titania</i>	10
2.3. Influence of some fundamental parameters on the TiO₂ photocatalysis	13
2.3.1. <i>Properties of the photocatalyst</i>	13
2.3.2. <i>Photocatalyst concentration</i>	14
2.3.3. <i>Initial compound concentration</i>	15
2.3.4. <i>Temperature</i>	16
2.3.5. <i>Light wavelength and intensity</i>	17
2.3.6. <i>pH</i>	17
2.3.7. <i>Oxygen</i>	18
2.3.8. <i>Water quality</i>	19
3. Synthesis of titania powders	20
3.1. Production of the TiO₂ powders by sol-gel method	21
3.1.1. <i>Hydrolytic sol-gel method</i>	22
3.1.2. <i>Non-hydrolytic sol-gel method</i>	24
3.2. Production of mesoporous titania	25
4. Development of visible light active photocatalysts by titania modifications	28
4.1. Mechanism of photoactivity of TiO₂ doped with metal cations	29
4.2. Mechanism of photoactivity of TiO₂ doped with nonmetal species	31
4.2.1. <i>Nitrogen doped TiO₂ (N-TiO₂)</i>	32
4.2.1.1. <i>Electronic structure of nitrogen-doped TiO₂</i>	33
4.2.1.2. <i>Incorporation of nitrogen in TiO₂ matrix</i>	34
4.2.1.3. <i>Synthesis of nitrogen-doped TiO₂</i>	36

4.2.1.4.	<i>Synthesis and photoactivity of substitutional and interstitial N-doped TiO₂</i>	38
4.2.2.	<i>Sulfur doped TiO₂ (S-TiO₂)</i>	40
4.2.2.1.	<i>Chemical nature and structural location of sulphur in TiO₂</i>	41
4.2.2.2.	<i>Synthesis and photoactivity of S-doped TiO₂</i>	42
4.2.3.	<i>Non-metal co-doping</i>	44
5.	Experimental procedure	48
5.1.	Materials and reagents	48
5.2.	Synthesis of undoped TiO₂ powders	50
5.3.	Synthesis of doped TiO₂ powders	50
5.3.1.	<i>Doping by sulfur</i>	50
5.3.2.	<i>Doping by nitrogen</i>	51
5.3.2.1.	<i>Annealing in ammonia flow</i>	51
5.3.2.2.	<i>Post-annealing in air</i>	51
5.3.2.3.	<i>Annealing in ammonia flow followed by annealing in air flow</i>	51
5.3.2.4.	<i>Annealing in a mixture of air and ammonia</i>	52
5.4.	Characterization methods	52
5.4.1.	<i>X-ray diffraction (XRD) analysis</i>	52
5.4.2.	<i>Nitrogen adsorption-desorption isotherms</i>	52
5.4.3.	<i>Field emission scanning electron microscopy (FESEM)</i>	54
5.4.4.	<i>Transmission electron microscopy (TEM) and high-resolution transmission electron microscopy (HR-TEM)</i>	54
5.4.5.	<i>X-ray photoelectron spectroscopy (XPS)</i>	54
5.4.6.	<i>Fourier transform infrared (FTIR) spectroscopy</i>	55
5.4.7.	<i>UV–Vis diffused reflectance spectra</i>	55
5.5.	Photocatalytic activity determination under UV and visible light	91
6.	Results and discussion	58
6.1.	Comparison of photocatalytic efficiency of powder P160/500 synthesized by nonhydrolytic sol-gel method and commercial P25	58
6.1.1.	<i>The comparison of the photocatalysts efficiency in different types of water</i>	59

6.1.2. <i>The influence of initial dye concentration on the initial photodegradation rate</i>	65
6.2. Characterization and photocatalytic activity of undoped TiO₂ synthesized by using different solvents	68
6.2.1. <i>X-ray diffraction analysis</i>	68
6.2.2. <i>Textural parameters</i>	70
6.2.3. <i>SEM analysis</i>	73
6.3. Photocatalytic activity under UV light	75
6.4. Optimization of conditions of nitrogen-doping	77
6.4.1. <i>Post-annealing in static air atmosphere</i>	77
6.4.1.1. <i>Visible-light activity of N-TiO₂ powders obtained at different post-annealing conditions</i>	77
6.4.1.2. <i>DRS analysis of the N-TiO₂ powders obtained at different post-annealing conditions</i>	80
6.4.1.3. <i>Morphology of the N-TiO₂ powders obtained at different post-annealing conditions</i>	80
6.4.2. <i>Visible-light activity of N-TiO₂ powders obtained by post-annealing in dynamic air atmosphere</i>	82
6.4.3. <i>Visible-light activity of N-TiO₂ powders annealed in air/NH₃ mixture followed by post-annealing in static air atmosphere</i>	82
6.5. Characterization of doped TiO₂	84
6.5.1. <i>X-Ray diffraction analysis</i>	85
6.5.2. <i>Textural parameters</i>	86
6.5.3. <i>SEM analysis</i>	88
6.5.4. <i>TEM analysis</i>	89
6.5.5. <i>XPS analysis</i>	91
6.5.6. <i>FTIR analysis</i>	95
6.5.7. <i>DRS analysis</i>	96
6.6. Photocatalytic activity under visible light	98
7. Conclusion	101
8. References	103
Curriculum Vitae	128

1. Introduction

The heterogeneous photocatalysis is an efficient, economical and environmentally friendly advanced oxidation process (AOP) for the degradation and mineralization of a wide range of organic contaminants in water. It is based on the formation of very reactive radicals as a result of photo-induced charge separation in the photocatalyst [1-4]. Metal oxides and sulphides (TiO_2 , ZnO , Fe_2O_3 , CdS , ZnS etc.) represent a class of semiconductor materials suitable for photocatalytic purposes. Among them, TiO_2 has proven to be the most promising photocatalyst because of its strong oxidizing power, cost effectiveness, high catalytic activity, long-term stability, lack of toxicity, high photochemical corrosive resistance, and abundance of the raw materials needed [5,6]. The photocatalytic activity of TiO_2 as a solid material is unavoidably influenced by the structural and textural properties, such as: phase composition, crystallinity, crystallite size, specific surface area, pore size distribution and morphological characteristics, which are dependant on the synthesis conditions. In addition, the efficiency of a photocatalyst depends on environmental factors, in other words some components found in water that processed may affect the efficiency [7].

The applicability of pure TiO_2 is limited by its large band gap (3.0 eV for rutile TiO_2 and 3.2 eV for anatase TiO_2), meaning it can be activated only under UV irradiation ($\lambda < 380$ nm) [8-10]. To overcome this drawback, the doping of TiO_2 by nonmetals, such as N, S, P, C and F, has been applied in order to shift the absorption onset of TiO_2 from UV to the visible region [11-16]. Among the explored nonmetal dopants, nitrogen and sulfur have been shown to be the most promising for the enhancement of photocatalytic activity of TiO_2 under visible light. Nitrogen can be incorporated in TiO_2 structure as a N^{3-} anion, interstitially or by substituting O^{2-} anions, while sulfur can be incorporated either as a S^{2-} anion, substituting the lattice oxygen, or as a cation $\text{S}(\text{IV}+)/\text{S}(\text{VI}+)$, substituting Ti^{4+} [17-19]. Apart from studies about N-doped and S-doped TiO_2 , recently a focus has been placed on N,S-co-doped TiO_2 , which can further extend the absorption range into the visible-light region improving the photocatalytic efficiency as a result of the synergy effect of the multiple ions [20–22].

Nitrogen and sulfur can introduced to the TiO_2 lattice by employing various precursors and preparation methods. In general, S-doped titania powders are synthesized

by different wet-chemical methods, using mainly thiourea as a source of sulfur [23,24], while N-doped TiO₂ can be synthesized by either gas phase annealing (usually in ammonia atmosphere) [25-27] or by wet-chemical routes, using urea, thiourea, ammonia, hydrazine etc. as a source of nitrogen [28,29]. Among the wet-chemical methods for titania preparation, the sol-gel techniques [30-32] have been widely applied because of the simplicity, low-cost and possibility to control the synthesis conditions. In addition, the sol-gel methods can provide appropriate textural properties of titania, i.e. high specific surface area and porous frameworks, which is essential for the photocatalytic efficiency. Since the small pore size hinders the diffusion of the large molecules of the organic pollutant into microporous titania, the synthesis of mesoporous titania is highly desirable to achieve a good photocatalytic degradation of organic pollutants in water [33-35]. It was shown [7,36] that nonhydrolytic sol-gel process coupled with solvothermal treatment may produce mesoporous nanocrystalline titania powders of narrow particle and pore size distributions, with a high photocatalytic activity under the UV irradiation [33-35].

In this dissertation, a non-hydrolytic sol-gel method was applied for the synthesis of undoped and N,S-doped and co-doped mesoporous titania. The photocatalytic activity under UV light of the undoped powder in saline waters and the influence of the type of solvent used in the synthesis on the properties and photocatalytic efficiency of the titania, were also investigated. As a precursor for S-doping, an aprotic solvent dimethyl sulfoxide (DMSO) was used during the gel synthesis, while the annealing in ammonia stream was applied for N-doping. The common precursors for N and/or S (i.e. urea, thiourea) were not used during the gel preparation, because of their low solubility in aprotic solvents used in the synthesis. The post-annealing in air of ammonia treated TiO₂ was optimized in order to achieve the best photocatalytic activity under visible light [37].

The scientific goals of the research in this dissertation were:

- synthesis of mesoporous TiO₂ powders by non-hydrolytic sol-gel process combined with solvothermal treatment for the application in the photocatalytic degradation of organic substances in water under UV and visible light
- investigation of the influence of the type of solvent used in the synthesis on the properties and photocatalytic efficiency of undoped powders under UV light,

- investigation of the influence of some ions present in saline water on the photocatalytic efficiency of undoped powders under UV light,
- investigation of the influence of the type of doping (N-doping, S-doping or N,S-co-doping) and method of N-doping (gel or powder annealing, annealing in pure ammonia or in a mixture ammonia/air at different ratios) on the properties and photocatalytic efficiency of the powders under visible light
- investigation of the influence of conditions of post-annealing in air after annealing in ammonia on the properties and photocatalytic efficiency of the powders under visible light
- determination of the mechanism of TiO₂ doping.

THEORETICAL PART

2. Heterogeneous photocatalysis

Heterogeneous photocatalysis is one of the advanced oxidation processes (AOPs) that involves a semiconductor photocatalyst for the production of radicals, having stronger oxidation power than ordinary oxidants normally used in water treatment. When a semiconductor is irradiated by light with energy matching or greater than its band gap, conduction band electrons (e_{CB}^-) and valence band holes (h_{VB}^+) are generated. These excited charge carriers are mobile and capable of initiating many chemical redox reactions at the semiconductor surface. The excited electrons and holes, however, tend to recombine quickly, dissipating the energy as heat. Therefore, the photocatalytic activity of semiconductors is largely dependent on the competition between the surface charge-carrier transfer and the electron-hole recombination. Thus, in order to carry out effective semiconductor photocatalysis, two essential criteria need to be satisfied: (1) optimum light absorption by the semiconductor; and (2) sufficiently long-lived photoexcited charge carriers to enable the occurrence of the desired reactions [38].

Among a wide spectrum of semiconductors, titanium dioxide (TiO_2) has proven to be the most promising photocatalyst for a wide range of applications because of its high photoreactivity under UV light irradiation, relatively low cost, nontoxicity, chemical and biological inertness, and long-term stability against photocorrosion [4,39]. Like other semiconductors, TiO_2 bears the inherent drawback of a rapid electron-hole recombination, and its photocatalytic activity is thus limited. To improve the photoefficiency of TiO_2 photocatalysis, the $e_{CB}^- - h_{VB}^+$ recombination rate must be reduced. In addition, TiO_2 is a solid-state material, thus its photocatalytic activity is influenced by particle size and particle size distribution, surface area, crystal and surface structure. Hence, the strategy to design and prepare TiO_2 -based photocatalysts with high photoefficiency has become a major topic leading to intensive research in the field [38].

2.1. Fundamentals of heterogeneous photocatalysis

A semiconductor (SC) is characterized by an electronic band structure in which the highest occupied energy band, called valence band (VB), and the lowest empty

band, called conduction band (CB), are separated by a bandgap, i.e. a region of forbidden energies in a perfect crystal [40]. When a semiconductor absorbs a photon of energy equal to or higher than its bandgap, an electron is promoted from its VB to its CB, within a femtosecond timescale (pathway a in **Fig. 1**):



The electrons and holes can be trapped in surface states where they can react with donor (D) (pathway c in **Fig. 1**), or acceptor (A) (pathway d in **Fig. 1**) species adsorbed or close to the surface of the particle (interfacial charge transfer). In the absence of suitable electron and hole scavengers, the stored energy is dissipated as heat within a few nanoseconds by recombination on the surface (pathway e in **Fig. 1**) or in the bulk of the particle (pathway b in **Fig. 1**) [40,41]:

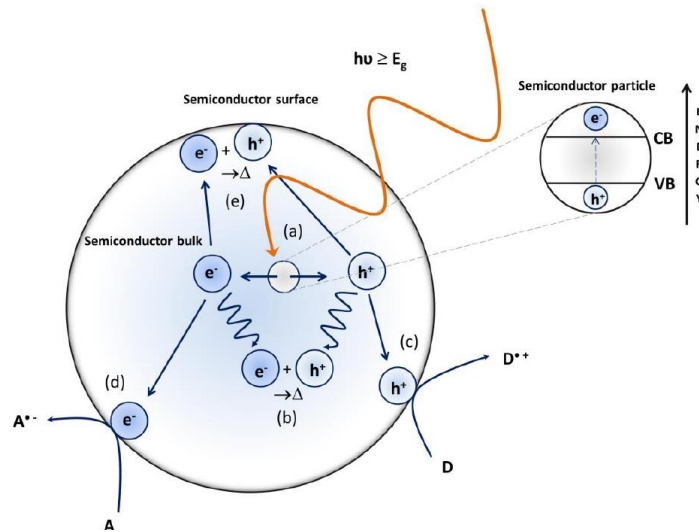
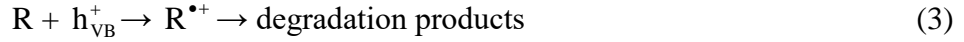


Fig. 1. Mechanism of semiconductor photocatalysis [42].

If a suitable scavenger or surface defect state is available to trap the electron or hole, recombination is prevented and redox reactions may occur. The valence band holes are powerful oxidants (+1.0 to +3.5 V vs. normal hydrogen electrode, NHE, depending on the semiconductor and pH), while the conduction-band electrons are good reductants (+0.5 to -1.5 V vs. NHE). Most organic (R) photodegradation reactions utilize the oxidizing power of the holes either directly or indirectly:

Direct oxidation:



Indirect oxidation:

Oxidation of adsorbed water:



Oxidation of adsorbed OH^- :

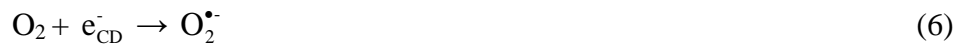


Hydroxyl radicals are extremely powerful oxidants (**Table 1**) that react rapidly with organic species with mineralization producing mineral salts, CO_2 and H_2O [43].

Table 1. Standard electrochemical reduction potentials of common oxidants [43]

Oxidant	Half-cell reaction	Oxidation potential (V)
OH^\bullet	$OH^\bullet + H^+ + e^- \rightarrow H_2O$	2.80
O_3	$O_3 + 2H^+ + 2e^- \rightarrow O_2 + H_2O$	2.07
H_2O_2	$H_2O_2 + 2H^+ + 2e^- \rightarrow 2H_2O$	1.77
Cl_2	$Cl_2 + 2e^- \rightarrow 2 Cl^-$	1.49
$HClO$	$2HClO + 2H^+ + 2e^- \rightarrow Cl_2 + 2H_2O$	1.36

However, to prevent a buildup of charge during the holes reactions, it is necessary to provide a reducible species to react with the electrons [41]. The electrons can be rapidly trapped by molecular oxygen adsorbed on the SD particle [43], which is reduced to form superoxide radical anion ($O_2^{\bullet-}$) (Eq. 6) that may further react with H^+ to generate hydroperoxyl radical (HO_2^\bullet) (Eq. 7) and further electrochemical reduction yields H_2O_2 (Eq. 8). These reactive oxygen species may also contribute to the oxidative degradation of a pollutant.



The probability and rate of the interfacial charge transfer processes for electrons and holes depends upon the respective positions of the band edges for the conduction and valence bands and the redox potential levels of the adsorbate species [44]. The energy level at the bottom of the CB is actually the reduction potential of photoelectrons and the energy level at the top of the VB determines the oxidizing ability of photoholes [40]. The relevant potential level of the acceptor species (species that are reduced) is thermodynamically required to be below (more positive than) the conduction band potential of the semiconductor. The potential level of the donor (species that are oxidized) needs to be above (more negative than) the valence band position of the semiconductor in order to donate an electron to the vacant hole [44]. The lower edge of the conduction band, upper edge of the valence band, and band gap of some semiconductors, are presented in **Fig. 2** [44]. The energy scale is indicated in electron volts using either the normal hydrogen electrode (NHE) or the vacuum level as a reference. On the right side, the standard potentials of several redox couples are presented against the standard hydrogen electrode potential.

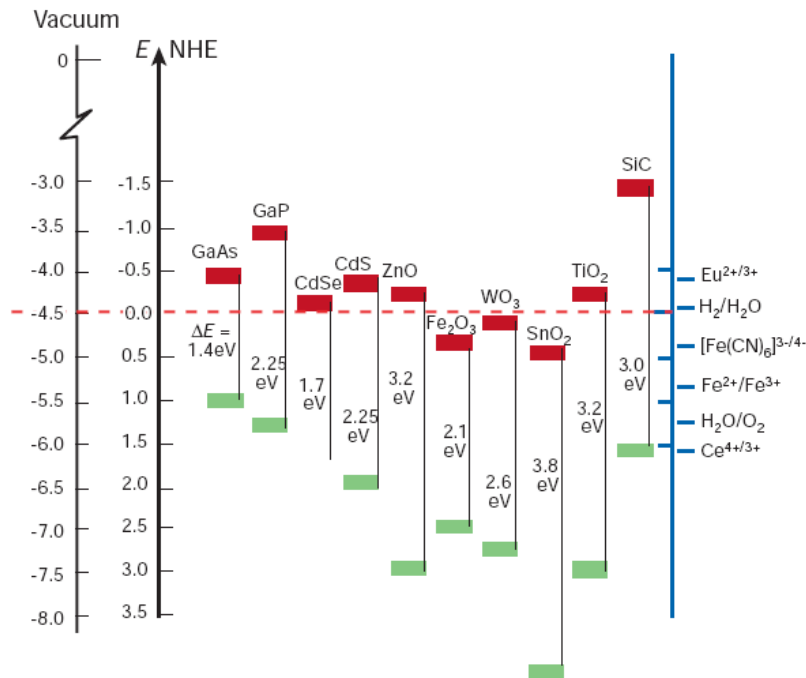


Fig. 2. Band positions of several semiconductors in contact with aqueous electrolyte at pH 1 (red colour - the lower edge of the conduction band, green colour - upper edge of the valence band). [44]

Apart from possessing suitable band gap energy, an ideal semiconductor should also be easy to produce and use cost effective, photo stable, nonhazardous for humans and the environment, effectively activated by solar light and able to catalyze the reaction effectively [45,46]. TiO_2 is close to being an ideal photocatalyst and the benchmark for photocatalysis performance: it is cheap, photostable in solution and nontoxic; its holes are strongly oxidizing and redox selective. The single drawback of TiO_2 as a photocatalyst is that it does not absorb visible light. To overcome this problem, several approaches including dye sensitization, doping, coupling and capping of TiO_2 have been studied extensively [45,46].

2.2. Structure and photocatalytic properties of titania

2.2.1. Structure of titania

TiO_2 exists in nature in several crystallographic forms: anatase, rutile, brookite and $\text{TiO}_2(\text{B})$, where brookite and $\text{TiO}_2(\text{B})$ are much rare polymorphs. Besides these crystallographic forms, two additional high-pressure forms have been synthesized from the rutile phase. These are $\text{TiO}_2(\text{II})$ with a PbO_2 structure and $\text{TiO}_2(\text{H})$, with a hollandite structure [45,46].

Rutile and anatase have been able to be synthesizing in pure form at low temperatures until recent days, while other polymorphs are synthesized only under sensitive conditions [47,48]. Therefore, only rutile and anatase play any role in the applications of TiO_2 .

The local order in each phase is represented by an octahedron constituting oxygen ions at its vertices and titanium atoms at the center with different spatial arrangements sharing the edges and corners in a different manner [48]. Rutile is composed of corner-sharing octahedra with each octahedron surrounded by ten octahedra, in which two are edge-shared and eight are corner-shared (**Fig. 3**). In anatase, $[\text{TiO}_6]$ octahedron is surrounded by eight octahedra (four edge-shared and four corner-shared) (**Fig. 3**). Thus, the fraction of edge-sharing octahedra required to form anatase is greater compared to rutile [48,49]. The tetragonal unit cell of rutile has the dimensions a

$a = b = 4.587 \text{ \AA}$ and $c = 2.953 \text{ \AA}$, while the one of anatase $a = b = 3.782 \text{ \AA}$ and $c = 9.502 \text{ \AA}$. These differences in lattice structures cause different mass densities and electronic band structures between the two forms of TiO_2 [50]: the density of rutile is higher (4.25 g cm^{-3}) than of anatase (3.894 g cm^{-3}), while the band gap is narrower (3.0 eV) than of anatase (3.2 eV).

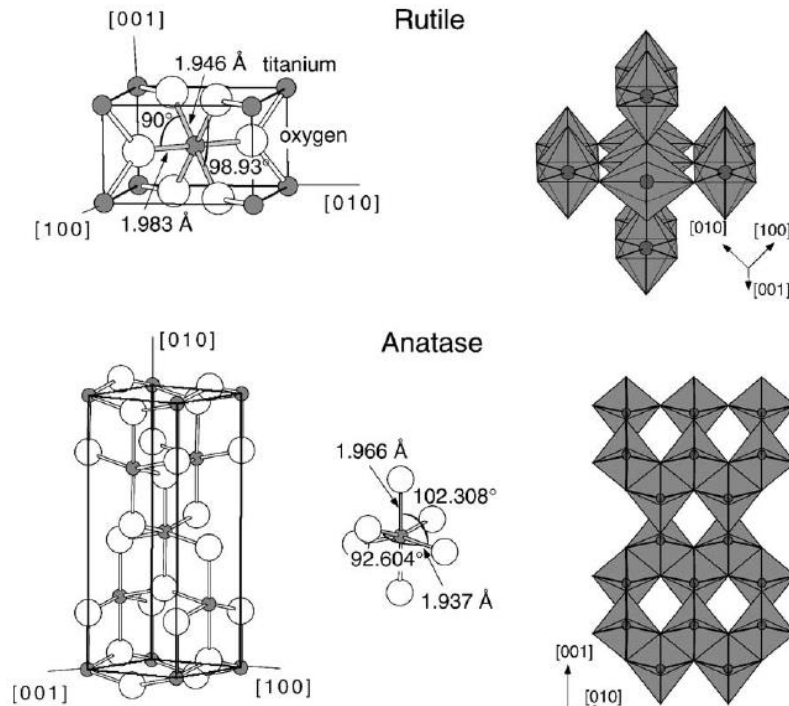


Fig. 3. Crystalline structures of anatase and rutile. The bond length and angles of the octahedrally coordinated Ti atoms are indicated and the stacking of the octahedral in both structures is shown on the right side [49].

Rutile is thermodynamically the most stable phase at all temperatures and pressures up to 60 kbar, where $\text{TiO}_2(\text{II})$ becomes the thermodynamic favourable phase. The small differences in the Gibbs free energy ($4\text{--}20 \text{ kJ}\cdot\text{mole}^{-1}$) between the rutile and anatase suggest that anatase is almost as stable as rutile at normal pressures and temperatures. The relative phase stability may reverse when particle sizes decrease to sufficiently low values due to surface-energy effects [45,46]. Anatase is kinetically stable, i.e., its transformation into rutile at room temperature is so slow that the transformation practically does not occur. The transformation reaches a measurable speed at $T > 600 \text{ }^\circ\text{C}$ [51,52], which could explain its higher surface area and its higher

surface density of active sites for adsorption and for catalysis. The reaction rate of anatase→rutile transformation is determined by different parameters, such as particle shape/size [53], the properties of starting material [54], atmosphere [55], reaction conditions [56], purity [57], surface defect concentration [58], grain boundary concentration [59], etc.

Inorganic additives, such as alumina [60], and zirconia [61], have been successfully used to control the anatase→rutile phase transformation in the preparation of titania. However, it is difficult to remove the additives from the final products and/or avoid the possible influence of additives on photocatalytic activity. Recently, authors investigated controllable synthesis processes of crystalline nanosized titania without any inorganic additives. Luo et al. [62] synthesized some bicrystalline (anatase and rutile) and tricrystalline (anatase, rutile, and brookite) mesostructured titania by varying the solvent and cosolvent (methanol, ethanol, 1-butanol, or 1-octanol, with or without water). Wang et al. [63] synthesized pure anatase, pure rutile and their mixed phases under alcohol solvothermal conditions. The amount and configuration of CH₂ in alcohols and the reaction temperature play two key roles in controlling the crystal structures, grain sizes and morphologies of the final products. Petrović et al. [7] synthesized mesoporous nanocrystalline titania powders by nonhydrolytic sol–gel process coupled with solvothermal treatment. The solvothermal treatment temperature had manifold influences on the structural, textural and photocatalytic properties of the gels and titania powders obtained by gel calcination. It was shown that by altering the gelation and calcination temperatures, it is possible to influence and, practically, control the phase transformation anatase→rutile.

2.2.2. *Photocatalytic properties of titania*

TiO₂ is a wide-bandgap semiconductor that requires the excitation light wavelength shorter than 386 nm for anatase and 416 nm for rutile. The absorption edge (threshold) of anatase is therefore in the near UV range, while the absorption of rutile is extended to visible range. The mentioned values concern single crystals or well-crystallized samples. Higher values are usually obtained for weakly crystallized thin

films or nanosized materials. This so-called blue shift of the fundamental absorption edge in TiO₂ nanosized materials has been observed amounting to 0.2 eV for crystallite sizes in the range 5–10 nm [64,65].

The band positions of TiO₂ (**Fig. 4**) are suitable for achieving the redox transformation of environmental pollutants. The TiO₂ VB places far lower (more positive) than the oxidation potentials of most organic and inorganic compounds (electron donors). Most metal oxide semiconductors have the similar E_{VB} potential edge because VB is primarily composed of O 2p atomic orbitals [66]. Nevertheless, TiO₂ is considered the most active among the metal oxide semiconductors probably because of the proper position of E_{CB} for the facile transfer of e_{CB}^- to O₂. In fact, the CB electron transfer to dissolved oxygen molecule has been considered as the rate-determining step in semiconductor photocatalysis. Therefore, the presence of alternative stronger electron acceptor often enhances the photocatalytic reactions significantly. Higher driving force of electron transfer to O₂ for anatase than for rutile, because of the higher E_{CB} of anatase by ~0.2 eV (**Fig. 4**), is probably reason for the higher photocatalytic activity of anatase for most reactions, regardless of the wider band gap. Reactions in which both crystalline phases have the same photoreactivity or rutile a higher one, are also reported. Furthermore, there are also studies, which claim that a mixture of anatase (70–75%) and rutile (30–25%) is more active than pure anatase. The disagreement of the results may lie in the intervening effect of various coexisting factors, such as specific surface area, pore size distribution, crystal size, and preparation methods, or in the way the activity is expressed [46].

In the **Fig. 4**, primary reaction mechanism of TiO₂ photocatalysis is presented:

- 1- bandgap excitation and electron–hole charge pair creation (Eq. 1),
- 2: the charge pair recombination (Eq. 2),
- 3: electron transfer to electron acceptor (A is usually dissolved oxygen, but some substrates may undergo the reductive transformation through their direct reaction with CB electrons),
- 4: electron transfer to oxygen molecule (Eq. 6),
- 5: formation of hydroperoxyl radical (Eq. 7),
- 6: formation of hydrogen peroxide (Eq. 8),

- 7: formation of hydroxyl radicals through the reactions of hydrogen peroxide with the CB electrons
- 8: hole transfer to electron donor (D is usually organic pollutant) (Eq. 3),
- 9: hole transfer to surface hydroxyl group (adsorbed water or OH⁻) to generate OH radicals (Eqs. 4 and 5)
- 10: hydroxyl radical-mediated oxidation of organic substrate (DH).

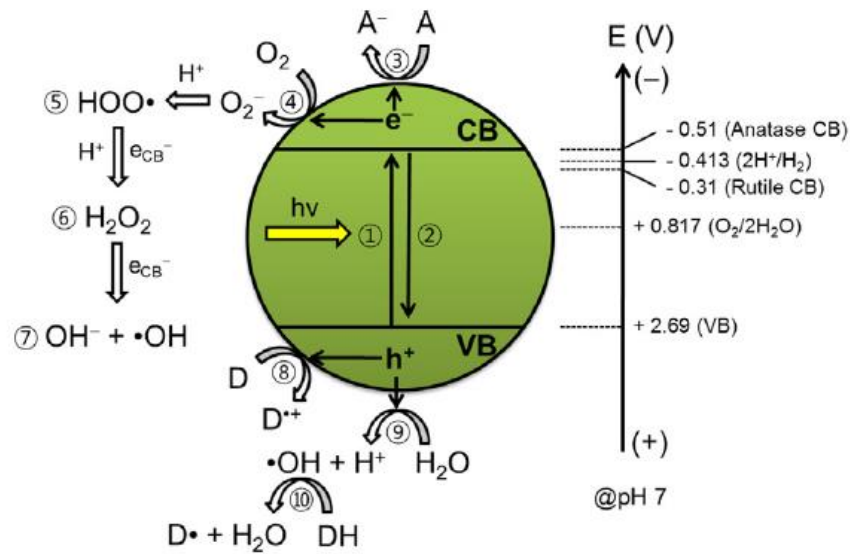


Fig. 4. Schematic illustration for energetics and primary reaction mechanism of TiO₂ photocatalysis [66]

As it shown in **Fig. 4**, organic substances can be oxidized directly by holes or by radicals. Generally, strongly adsorbed molecules tend to be oxidized directly by h_{VB}^+ , while weakly adsorbed ones can be more favorably degraded by OH radicals.

The processes 1-10 take places at different rates. The band gap excitation creates electrons and holes in femtosecond time scale, which are subsequently trapped in 100 ps (shallow trap) to 10 ns (deep trap) and recombines with each other in the range of 10–100 ns:

Charge-carrier trapping:



(shallow trap, dynamic equilibrium)



(deep trap, irreversible)

Surface charge-carrier recombination:



Environmental applicability of semiconductor photocatalysts is directly related to the interfacial charge transfers of (trapped) holes and electrons, which occur more slowly in 100 ns and ms ranges, respectively:



Obviously, the slow interfacial charge transfer (Eqs. 14 and 15), especially the electron transfer to oxygen, limits the overall photocatalytic reaction rate.

2.3. Influence of some fundamental parameters on the TiO₂ photocatalysis

Photocatalytic activity of TiO₂ depends primarily on structural and textural properties of the photocatalyst, such as phase composition, crystallite size, surface area, pore size distribution and morphological characteristics. In addition to the nature of the photocatalyst, it has been demonstrated that catalyst dosage, character and initial concentration of the target compound, coexisting compound, light intensity, oxygen concentration, presence of supplementary oxidizable substance, temperature, circulating flow rate and pH of aqueous treatments, are the main parameters affecting the photocatalysis rate.

2.3.1. Properties of the photocatalyst

The photocatalytic activity is not necessarily dependent on catalyst surface area, but rather on the availability of active sites. Therefore, properties like crystalline

structure, pore size, density of OH groups, surface acidity, number and nature of trap sites (both in lattice and at surface), and adsorption/desorption characteristics play an important role in photocatalytic efficiency [46].

A large surface area can be the determining factor in certain photodegradation reactions, as a large amount of adsorbed organic molecules promotes the reaction rate.

However, powders with a large surface area are usually associated with large amounts of crystalline defects, which favour the recombination of electrons and holes leading to a poor photoactivity. Then, a balance between surface area and crystallinity must be found in order to obtain the highest photoactivity.

Particle size is an important parameter for photocatalytic efficiency, since the predominant way of electron–hole recombination may be different depending on the particle size. Small variations in particle diameters lead to great modifications in the surface/volume ratio, thus modifying the significance of volume and surface electron–hole recombinations. Experimental investigations support the existence of an optimum particle size of TiO₂, where photocatalytic oxidation rates of organic substrates are maximized.

The surface hydroxyl groups play an important role in the photodegradation process due to: i) direct participation in the reaction mechanism by trapping of photogenerated holes that reach the catalyst surface producing surface HO[•], and ii) a change in the adsorption of reactant molecules both by acting itself as active sites for pollutant adsorption and by covering the sites where electron trapping by adsorbed oxygen takes place. This process is not only important for producing oxygen radicals but also for hindering electron–hole recombination.

2.3.2. *Photocatalyst concentration*

The overall photocatalytic reaction rate is directly proportional to the amount of TiO₂ [1], in both (i) the complete-mixed slurry batch reactor where TiO₂ particles are suspended in the aqueous solution, and (ii) the fixed media reactor where TiO₂ particles are attached onto stationary surfaces within the reactor [67]. The increase in the photocatalyst concentration increases the number of photons absorbed on the

photocatalyst surface and also increases the number of the organic compound adsorbed on the surface of photocatalyst and facilitates the photocatalytic activity. However, when the photocatalyst dosage increases above the optimum level, the photocatalytic activity decreases due to:

- Aggregation of TiO₂ particles that leads to decrease in the number of surface active sites [68]
- Increase in turbidity of the solution, which reduces the light transmission through the solution [69].
- When all organic compound molecules are adsorbed on the surface of the catalyst, the addition of photocatalyst quantities will have no effect on the degradation efficiency [70].

For applications, this optimum mass of catalyst has to be chosen in order to avoid excess of catalyst and to ensure a total absorption of efficient photons. The optimum amount of catalyst for efficient degradation depends mainly on the geometry and working conditions of the photo-reactor, type of the organic compound and the morphology and textural properties of the catalyst [71].

2.3.3. *Initial compound concentration*

Photocatalytic reaction rate is dependent on the concentration of the compound to be treated: under similar operating conditions, a variation in the initial concentration of the compound will result in different irradiation time necessary to achieve reaction completion. Owing to the photonic nature of the photocatalytic reaction, excessively high concentration of organic substrate is known to simultaneously saturate the TiO₂ surface and reduce the photonic efficiency leading to photocatalyst deactivation [72,73,74]

Generally, the kinetics of photocatalytic reactions follows a Langmuir-Hinshelwood (L-H) mechanism [75-78], confirming the heterogeneous catalytic character of the system with a reaction rate r varying proportionally to the fraction of surface covered θ by the reactant:

$$r = -\frac{dC}{dt} = k\theta = k \frac{K \cdot C}{1 + K \cdot C} \quad (16)$$

where k is the rate constant, which is dependent on the diffusion of the reactant into the pores and the reaction at the interface [41], C is the concentration of the reactant at time t and K is the Langmuir adsorption to desorption equilibrium constant.

According to the L-H model, the reaction rate is maximum and of the zero order ($r = k$) at high reactant concentrations ($KC \gg 1$). When the adsorption is relatively weak and/or the reactant concentration is low ($KC \ll 1$), Eq. (16) can be simplified to the pseudo-first order kinetics with an apparent first-order rate constant k_{app} [79-81]:

$$-\ln\left(\frac{C}{C_0}\right) = kKt = k_{app}t \quad (17)$$

where C_0 is the initial concentration of the reactant and C is the concentration after illumination time t .

2.3.4. Temperature

An increase in temperature is found to be detrimental to the process of photocatalysis for two main reasons: i) it promotes recombination of photogenerated electrons and holes, and ii) it promotes desorption of adsorbed reactants [82]. The increase in temperature above 80 °C highly enhances recombination of charge carriers and desorption process of adsorbed reactant species, resulting in high decrease of photocatalytic activity. On the contrary, a temperature below 80 °C favours adsorption, which is a spontaneous exothermic phenomenon, resulting in enhancing the adsorption of final reaction products. A further reaction in temperature down to 0 °C will cause an increase in the apparent activation energy. As a consequence, the optimum reaction temperature for photocatalysis is reported to be in the range of 20- 80 °C [83].

2.3.5. Light wavelength and intensity

The variations of the reaction rate r as a function of the wavelength λ follows the absorption spectrum of the catalyst (**Fig. 5a**), with a threshold E_G corresponding to its band-gap energy ($E_G = hc/\lambda$).

Intensity of light affects the rate of transfer of electrons from its VB to CB, and hence the rate of formation of e-/h+ pair. Higher the intensity, higher is this rate and so is the rate of photocatalysis. However, with increase in light intensity beyond an optimum, the rate of photogeneration of e- and h+ becomes more than the rate of the subsequent redox reactions. The rate of photogeneration is then no longer the controlling step and hence it gradually becomes less dependent on the intensity of light [82], so the linear dependency of reaction rate on light intensity is changed to a square-root dependency above certain threshold value (**Fig. 5b**). At high intensities, the dependency of the photocatalytic reaction rate on radiant flux reduced to zero. The optimal light power utilization corresponds to the domain where the degradation rate is proportional to light intensity.

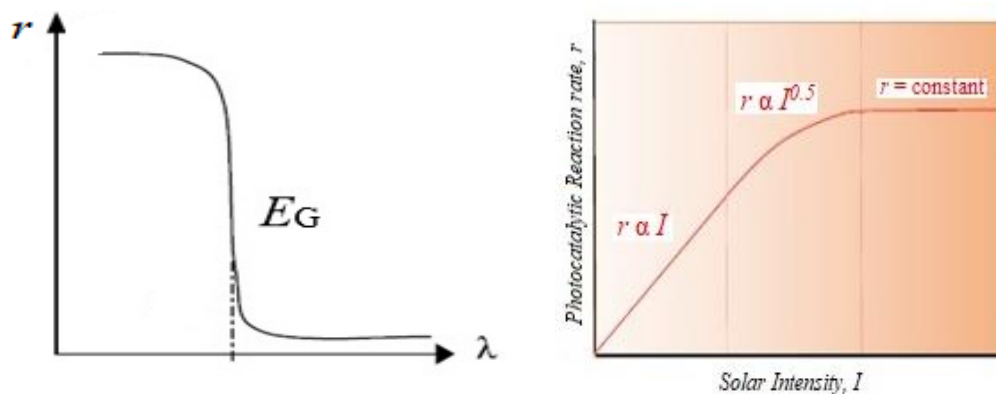


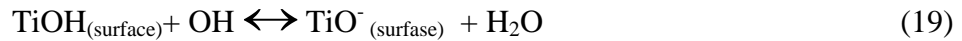
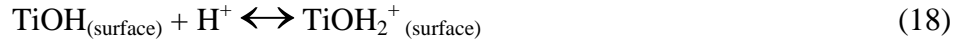
Fig. 5. The dependence of photocatalytic reaction rate on: a) light wavelength, b) light intensity [82].

2.3.6. pH

In heterogeneous photocatalytic water system, pH is one of the most important operating parameters that affect the charge on the catalyst particles, size of catalyst aggregates and the positions of conduction and valence bands.

Catalyst surface charge is determined by solution pH value and value of point of zero charge, pH_{pzc} . The solution pH value at which the surface charge density of the catalyst is equal to zero is called the point of zero charge. The point of zero charge for TiO_2 particles is $\text{pH}_{\text{pzc}} = 6.8$ [84].

The surface titanol groups of TiO_2 ($>\text{Ti-OH}$) undergoes the following acid–base equilibrium reaction.



When operating $\text{pH} < \text{pH}_{\text{pzc}}$, the surface of the catalyst becomes positively charged and gradually exerts an electrostatic attraction force towards the negatively charged compounds. Such polar attractions between catalyst and charged anionic organic compounds can intensify the adsorption onto the photon activated catalyst surface for subsequent photocatalytic reactions [85]. At $\text{pH} > \text{pH}_{\text{pzc}}$, the catalyst surface will be negatively charged and repulse the anionic compounds in water.

Besides, the interaction between the catalyst particles itself also exists and is dependent on the operating pH. At $\text{pH} = \text{pH}_{\text{pzc}}$, the neutral surface charge of the catalyst particles is unable to produce the interactive rejection for solid - liquid separation. Thus, this induces catalyst aggregation where the catalyst particles become larger, leading to catalyst sedimentation.

The solution pH also alters the TiO_2 energy levels according to the Nernstian behavior (-59 mV/pH) due to the pH-dependent surface charge [66]:

$$E_{\text{CB}}(\text{V vs. NHE}) = -0.1 - 0.059\text{pH} \quad (20)$$

2.3.7. Oxygen

Dissolved oxygen plays an important role in photocatalysis reactions because molecular oxygen acts as a conduction band electron scavenger, suppressing totally or partially the surface electron-hole recombination. The superoxide radical ($\text{O}_2^{\bullet-}$) formed in this way (Eq. 6) is an effective oxidant agent, as well as hydrogen peroxide (Eq. 7)

hydroxyl radicals (Eq. 8). But, higher concentrations of oxygen lead to a downturn of the reaction rate, which is attributed to the fact that the TiO₂ surface becomes highly hydroxylated to the extent of inhibiting the adsorption of pollutant at active sites [46].

The total amount of dissolved oxygen in a reactor depends on a few technical considerations. For the complete-mixed slurry batch photoreactor, the total delivered dissolved oxygen not only acts as an electron sink but also provides sufficient buoyant force for complete suspension of TiO₂ particles. Photoreactor sparging with pure oxygen in TiO₂ slurry reactor is usually a cost-ineffective solution, as the amount of dissolved oxygen being held-up is a function of the photoreactor geometry. The difference between the two sparging media of air and oxygen is usually not very drastic as the mass transfer of oxygen to the close vicinity of the surface is the rate dependent step. Generally the Henry's law can be assumed to give a good approximation of the amount of oxygen dissolved under the experimental conditions. In this equilibrium law, it is also necessary to account for the decrease in oxygen solubility with increasing reaction temperature. As discussed, it is preferential to operate the photoreactor under ambient conditions to prevent the elevated cost of air or oxygen sparging for enhanced electron sink [72].

2.3.8. *Water quality*

The efficiency of the photocatalyst could be greatly influenced by the components found in water that processed.

Turbidity is determined by the presence and quantity of contaminants which lead to losing the water its transparency, and therefore affect the TiO₂ photocatalyst process where reduce the penetration of UV light by strong scattering and absorption of the rays [86]. The suspended solids in the target water that are retained on the filter medium after filtration, high concentrations of organic matter and high catalyst concentrations lead to decline the overall photocatalytic efficiency for water treatment, so the pre-treatment methods as sedimentation, rapid and slow sand filters, chemical coagulation and flocculation, and ceramic filters are necessary to reduce turbidity before TiO₂ photocatalytic processes.

To ensure rapid photocatalytic reaction rate, the turbidity of the targeted water should be kept below 5 nephelometric turbidity units (NTU) for optimal UV light utilization and photocatalytic reaction. The limit of 5 NTU is arbitrary and depends on the receiving water bodies and the treatment levels required [87].

Inorganic ions: A number of studies have been conducted on the effects of different inorganic anions or cations on TiO₂ photocatalysis. To date, the effects of both inorganic cations (i.e. Na⁺, K⁺, Ca²⁺, Cu²⁺, Mn²⁺, Mg²⁺, Ni²⁺, Fe²⁺, Zn²⁺, Al³⁺) and inorganic anions (i.e. Cl⁻, NO₃⁻, HCO₃⁻, ClO₄⁻, SO₄²⁻, HPO₄²⁻, PO₄³⁻) on the photocatalytic water treatment have been investigated [88,89]. A general consensus from these studies concludes that Cu²⁺, Fe²⁺, Al³⁺, Cl⁻, PO₄³⁻ at certain levels may decrease photocatalysis reaction rates, while Ca²⁺, Mg²⁺, Zn²⁺ may have negligible effects.

Several mechanisms for fouling effects of inorganic ions on TiO₂ photoactivity have been proposed. These include UV screening, competitive adsorption to surface active sites, competition for photons, surface deposition of precipitates and elemental metals, radical and hole scavenging [90,91] and direct reaction with the photocatalyst.

To resolve TiO₂ photocatalyst fouling issue, preventative or regenerative strategies can be adopted, depending on the nature of the photocatalysts deactivation in the water matrix. Fouling preventative strategies by means of water pretreatment, complexation and photocatalyst surface modifications can be addressed, while rinsing the TiO₂ surface with different chemical solutions constitutes the regenerative strategies.

3. Synthesis of titania powders

The performance of titania materials is strongly dependent on their structural characteristics, i.e. crystal phase, particle and pore sizes and surface structure, which is closely related to the method of synthesis. Thus, the synthesis of titania materials has received increasing attention in recent years [92], because the properties of TiO₂ can be manipulated via careful monitoring of the processing conditions. Among the several wet and dry methods, synthesis from a homogeneous solution seems to be very promising as

multiple reaction parameters like precursor concentration, chelating agents, solvents, mineralizer, pH of the solution, aging time, reaction temperature, and kinetics of precursor hydrolysis, can be easily adjusted to tailor the intrinsic properties of the final product. The solution approach offers the possibility to control the reaction pathways on a molecular level during the transformation of precursor species into final products, enabling the synthesis of well-defined crystal polymorphs and morphologies, without impurities [48]. Until now, a variety of wet methods have been developed for the synthesis of titania materials, such as: hydro(solvo)thermal method [90], microwave hydrothermal process [91], the sol-gel process [93-95], the sol-gel process coupled with hydro(solvo)thermal treatment [96], microwave assisted sol-gel process [97], ultrasonic-induced precursor hydrolysis [98], etc. The sol-gel techniques [30-32] have been widely applied because of the possibility to control the synthesis conditions in order to achieve appropriate textural properties of titania, i.e. high specific surface area and porous frameworks, which is essential for the photocatalytic efficiency.

3.1. Production of the TiO₂ powders by sol-gel method

In conventional, so-called hydrolytic sol-gel processes [99], sol and gel formation is due to the formation of Ti-O-Ti bridges through hydrolysis and polycondensation reactions of the precursors, which are usually inorganic metal salts or metal organic compounds such as metal alkoxides. Complete polymerization and loss of solvent leads to the transition from the liquid sol into a solid gel phase.

On the other hand, any reaction leading to the same bridges in good yields could afford an alternative sol-gel route [100]. Thus, in the so-called non-hydrolytic sol-gel processes, Ti-O-Ti bridges result, from the condensation between different compounds, under exclusion of water: alkoxide and halide, acetates and alkoxides, ether and halide, halide and alcohol, etc. [101]

3.1.1. Hydrolytic sol-gel method

The hydrolytic sol-gel process can be defined as the conversion of a precursor solution into an inorganic solid via inorganic polymerization reactions induced by water. In general, the precursor or starting compound is either an inorganic metal salt (chloride, nitrate, sulfate, ...) or a metal organic compound such as an alkoxide, $M(OR)_n$. Metal alkoxides are the most widely used precursors, because they react readily with water.

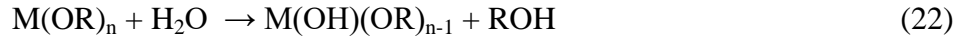
In general, the sol-gel process consists of the following steps [102]: i) Preparation of a homogeneous solution either by dissolution of metal organic precursors in an organic solvent that is miscible with water, or by dissolution of inorganic salts in water; ii) conversion of the homogeneous solution into a sol by treatment with a suitable reagent (generally water with or without any acid/base); iii) aging; iv) shaping; and v) thermal treatment/sintering.

The route that starts from inorganic salts involves the formation of condensed species by adjusting the pH, by increasing the temperature or by changing the oxidation state. Nevertheless, this method has several disadvantages. The aqueous chemistry of metal ions can be rather complicated because of the formation of a large number of oligomeric species, depending on the oxidation state, the pH or the concentration. The role of the counter anions, which are able to coordinate the metal ion giving rise to a new molecular precursor with different chemical reactivity towards hydrolysis and condensation, is difficult to predict. These ions can influence the morphology, the structure and even the chemical composition of the resulting solid phase. In addition, the removal of these anions from the final metal oxide product is often a problem. Many of these issues can be avoided by using metal alkoxides as precursors. They are often soluble in organic solvents, providing high homogeneity, and they can easily be converted to the corresponding oxide [102].

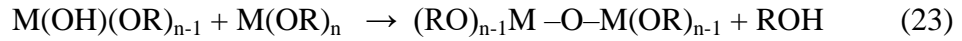
The main step in a sol-gel reaction is the formation of an inorganic polymer by hydrolysis and condensation reactions, i.e., the transformation of the molecular precursor into a highly crosslinked solid. Hydrolysis leads to a sol, a dispersion of colloidal particles in a liquid, and further condensation results in a gel, an

interconnected, rigid and porous inorganic network enclosing a continuous liquid phase. This transformation is called the sol-gel transition.

Hydrolysis of metal alkoxides in excess water leads to the formation of insoluble hydroxides or hydrated oxides. However, when restricted amounts of water are added, metal alkoxides undergo partial hydrolysis reactions, yielding soluble species that can take part in polymerization reactions [103]:



Subsequent condensation reactions involving the hydroxy metal alkoxide produces polymerizable species with M–O–M bonds and alcohol (ROH) or water as a by-product:



The chemical reactivity of metal alkoxides towards hydrolysis and condensation depends mainly on the electronegativity of the metal atom, its ability to increase the coordination number, the steric hindrance of the alkoxy group, and on the molecular structure of the metal alkoxides (monomeric or oligomeric).

The gels can be dried in two ways. Upon removal of the pore liquid under hypercritical conditions, the network does not collapse and aerogels are produced. When the gel is dried under ambient conditions, shrinkage of the pores occurs, yielding a xerogel [102].

The dry gels are typically amorphous, exhibiting a rather high specific surface area. A transition from the amorphous to the crystalline phase is typically induced by a calcination step, leading in most cases to a deterioration of the pore system and an increase of the particle size associated with a decrease of the specific surface area [104].

The major problem of sol-gel methods based on the hydrolysis and condensation of alkoxide is the control over the reaction rates. For most alkoxides of titanium, these reactions are very fast, resulting in loss of morphological and structural control over the final oxide material. One possibility to decrease and to adjust the reactivity of the alkoxides is the use of organic additives like carboxylic acids, β -diketones or functional alcohols, which act as chelating ligands and modify the reactivity of the precursors

[105]. An alternative strategy involves the slow release of water by chemical or physical processes, allowing control the local water concentration and thus the hydrolysis of the alkoxide. In spite of these efforts, the strong sensitivity of hydrolytic sol-gel processes towards any slight changes in the synthesis conditions and the simultaneous occurrence of hydrolysis and condensation reactions make it still impossible to fully control the hydrolytic sol-gel processing of metal oxides. One alternative strategy is provided by nonhydrolytic sol-gel processes, in which precursors, solvents, experimental conditions, catalysts, and reaction mechanisms are changed [101].

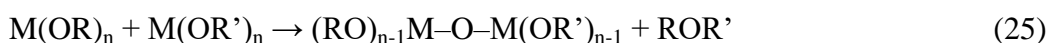
3.1.2. *Non-hydrolytic sol-gel method*

In non-hydrolytic sol-gel chemistry, the transformation of the precursor takes place in an organic solvent under exclusion of water. Discarding reactions where water is produced in situ, non-hydrolytic sol-gel methods fall into two groups, depending on whether they involve hydroxylation reactions or not. In the latter case, rigorously aprotic conditions are preserved by the use of heterofunctional condensation reactions excluding hydroxyl groups; such reactions will be referred to as aprotic condensation reactions [101].

Non-hydrolytic hydroxylation reactions include: i) thermal decomposition of metal alkoxide precursor (in the temperature range 200-300 °C), where hydroxyl groups are produced via a cyclic elimination mechanism with liberation of alkene, ii) action of certain alcohols on halides, iii) reaction of carbonyl compounds such as ketones with basic metal alkoxides, etc.

In *aprotic condensation reactions*, formation of an oxo bridge is provided by the condensation reaction between two different functional groups bonded to two metal centers by eliminating a small organic molecule. The main important reactions are [106]:

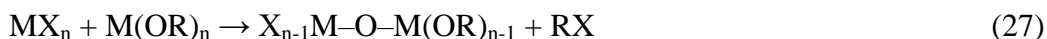
- reaction between two alkoxides, where dialkil eter is eliminate



- reaction between alkoxide and alkoxide modified by carboxylic acid, where ester is eliminate



- reaction between alkoxide and metal halide, where alkyl halide is eliminate



- reaction between metal halide and an organic ether, where alkyl halide is eliminate



The reactions of formation of the M-O-M bridges are usually quite slow at room temperature; in most cases, the oxide formation requires heating between 80 and 150 °C. The only reaction that takes place at room temperature is the redistribution of the ligands around the metal atoms. In the case of the reaction between TiCl₄ and Ti(OR)₄, which is usually applied for the titania synthesis [7,101,106,107], the substituent's around the titanium atoms redistribute at room temperature, which leads to the formation of an equilibrated mixture of TiCl_{4-x}(OR)_x species with 0 ≤ x ≤ 4. Further heating of the reaction mixture provides formation of a three-dimensional TiO₂ network (gelation) with the by-product of the reaction RCl enclosed in its pores [108], which can be removed by heating to temperatures over 500°C or by an UV-illumination treatment [109]. The temperature of the gelation has manifold influences on the structural and textural properties of the gels and titania powders obtained by gel calcination: the crystallinity level, the specific surface area and the total pore volume increase, while the average pore size decreases with increasing gelation temperature [7].

3.2. Production of mesoporous titania

Titania has been widely used as a photocatalyst for the removal of large organic molecules from water. Since the small pore size hinders the diffusion of the large molecules of the pollutant into microporous titania, the synthesis of mesoporous titania is highly desirable to achieve a good photocatalytic degradation of organic pollutants in

water. If mesoporous titania could be prepared with an anatase crystalline wall, it would be a useful material applicable as a high performance photocatalyst [34].

Lots of work has been done in the controllable synthesis of mesoporous titania with various mesostructures (lamellar, two-dimensional (2D) hexagonal, three-dimensional (3D) hexagonal and cubic), pore-wall parameters, morphology (nanotubes [110], nanoparticles (NPs) [111], nanowires [112], nanosheets [113]), as well as compositions [114].

There are mainly two pathways to synthesize ordered mesoporous titania, one is soft-templating method and the other is hard-templating nanocasting approach [114]. In addition, there are several routes to prepare disordered mesoporous TiO_2 .

The soft-templating method usually undergoes a coassembly process of the precursor and surfactant templates. Since the success in the synthesis of ordered mesoporous silica, there is a tendency to extend this methodology to transition metal oxide analogues. However, as it already stated, it is not easy to control the reactivity of transition metal oxide precursors as that of silicates, because they are highly sensitive to water or even moisture and tend to fast hydrolyze and form dense precipitates prior to assembly with the surfactant templates. So the key issue in the synthesis of mesoporous TiO_2 is to control the hydrolysis of Ti precursors for the co-assembly with the surfactants. Since it is not easy to control the hydrolysis and polymerization of Ti precursors in aqueous solution, the obtained TiO_2 materials usually do not have high mesostructural regularity over large domains.

The hard-templating approach is usually to prepare mesoporous materials in a confined space, in which the growth of the precursor is restricted to the surface, cages, channels, or substrate of a 'hard template'. The nanoparticles, colloidal crystals and mesoporous materials have been used as the hard template. If a highly ordered mesoporous material is used as the template, an ordered mesoporous replica can be obtained by a controllable nanocasting process [114].

In methods in which a surfactant was used to arrange the mesoporosity, the wall of the synthesized materials is normally amorphous. Crystallization of these materials under heat treatment or UV light irradiation could easily destroy the three-dimensional mesostructure and reduce the photocatalytic activity [91]. Also the removal of surfactant from the gel pores by extraction was hindered by metallo-surfactant interactions,

thereby seriously deteriorating the end product. To avoid the collapse of the mesostructure, several methods have been applied to prepare mesoporous titania materials without templates. The combination of sol-gel and hydro/solvothermal methods has been shown as successful in obtaining of mesoporous titania [107-109,115-117]. It is shown that that hydro/solvothermal treatment significantly affects the physical properties of porous TiO₂, particularly crystal composition, crystallinity, thermal stability, surface area, pore size distribution and photocatalytic activity.

Guo et al. [118] fabricated two types of 3D mesoporous TiO₂ microspheres using various titanium sources via a one-step solvothermal process without templates. They investigated the photodegradation of bisphenol A [2,2-bis(4-hydroxyphenyl)propane, BPA] in aqueous suspension under UV irradiation. The experimental results revealed that the photocatalytic effect of the two 3D mesoporous TiO₂ microspheres was superior to the commercial P25 TiO₂.

The Caruso group [119] studied the synthesis of crystalline, mesoporous TiO₂ beads through a facile combination of sol-gel and solvothermal processes. Dye-sensitized solar cells made from these mesoporous beads gave a total power conversion efficiency of 7.2 % under sunlight higher than that obtained using Degussa P25 films of similar thickness (5.7%).

Tanasković et al. [107] demonstrated that mesoporous titania with well-crystallized anatase phase can be synthesized by nonhydrolytic sol-gel process combined with solvothermal treatment, followed by annealing at 500 °C. They found that the increasing of gelation time doesn't increase the crystallinity of the dry gel and titania powder obtain by the annealing of the gel. The increasing temperature of the solvothermal treatment caused increase of the crystallinity level, the specific surface area and the total pore volume, while the average mesopore size decreased. The photocatalytic activity of the titania powder tested by measuring the photocatalytic degradation of the azo dye C.I. Reactive orange 16, was sufficiently high and attained the photocatalytic activity of the broadly accepted commercial powder P-25 produced by Degussa.

4. Development of visible light active photocatalysts by titania modifications

A major shortcoming of pure TiO₂ is related to its wide band gap energy of about 3 eV, meaning that only near-ultraviolet radiation can be used for its photo-activation. This limits the use of zero-cost natural sunlight since solar radiation reaching the surface of the earth contains only about 3-5% UV radiation [10,120-122]. Therefore, it is of great interest to find ways to extend the absorbance wavelength range of TiO₂ to the visible region without lowering its photocatalytic activity.

In addition, the recombination of photo-generated charge carriers is the important limitation in semiconductor photocatalysis as it reduces the overall quantum efficiency [123,43]. Smaller band gap of visible light active photocatalysts often results in rapid recombination and conversion of photonic energy into non-usable heat. As it already stated, recombination can occur either in the bulk or on the surface and is induced by defects, impurities and other crystal bulk/surface imperfections [124,125].

Therefore, the main aim of titania modifications is to shift its optical response to the visible-light region and to reduce the rate of electron-hole pair recombination to increase its photoreactivity [126]. The common techniques used for TiO₂ modifications [127-137] can be classified into two groups: surface and bulk modifications.

Surface modifications include anchoring colored inorganic semiconductors, for example CdS and CdSe [127], or organic dyes on the TiO₂ surface [128], where they act as sensitizers. However, most of these sensitizers are susceptible to photocorrosion or degradation in aqueous solutions and are not suitable for photocatalytic water treatment applications. In addition, metallic nanoparticles including Pt, Pd, Au, Ag, Ru, and Fe have been used to enhance the photocatalytic activity by suppressing the e⁻/h⁺ recombination behaviors. The photo-induced electrons migrate to the metal due to the relatively low Fermi level of metals, which make the photo-induced holes stable on the TiO₂ surfaces by increasing the lifetime of the charge carrier [138].

Bulk modifications are mainly effected by doping metals or non-metals into bulk TiO₂. The modified catalysts appear to be photo-stable in aqueous solution and can be used in photocatalytic water purification.

The doping is one of the most promising methods to extend the light-absorbing properties of TiO₂, which can also bring other advantages, such as low recombination rate of electrons and holes and high anatase crystallinity.

4.1. Mechanism of photoactivity of TiO₂ doped with metal cations

Various transition and rare earth metal dopants, including copper (Cu) [139], zinc (Zn) [140], cobalt (Co) [141], manganese (Mn), nickel (Ni), iron (Fe), chromium (Cr), vanadium (V), etc., have been analyzed to change titania bandgap and shift the photo-response into visible spectrum. Another benefit of transition metal doping species is the improved trapping of charge carriers to inhibit electron-hole recombination during illumination [44,114,142].

In transition-metal-doped titania, there are two different positions that the dopant ions can occupy in the lattice, i.e., substitutional and interstitial. If the ionic radius of the dopant is similar to that of Ti⁴⁺, the dopant will conveniently take the substitutional mode. If the dopant radius is much smaller than the Ti⁴⁺, interstitial doping is also possible. The dopant ions should be within an appropriate concentration to exclude phase separation between the dopant and the matrix.

Upon metal-ion doping, new energy states can be formed either within or beyond the band gap of TiO₂ (**Fig. 6**). Due to the formation of intra-band-gap energy levels, the light absorption edge can be red-shifted (shifted to higher wavelength) by electronic transitions from the VB to these levels and/or from these levels to the CB [143].

In the Fig. 6, the energy states formed by doping with chromium and iron are presented. The most frequently employed valence states of Cr and Fe ions are Cr³⁺ and Fe³⁺, respectively. If these cations are incorporated into the TiO₂ lattice by substituting Ti⁴⁺, the electroneutrality as a whole requires the simultaneous formation of oxygen vacancies, the amount of which should be equal to half of the incorporated cations:



where M refers to the corresponding metal (Fe or Cr), M_{Ti}^{\bullet} is dopant metal in the Ti^{4+} position, $V_o^{\bullet\bullet}$ represents the oxygen vacancy, the energy level of which lies slightly below the CB edge (Fig. 6); O_o denotes the oxygen atom at its normal lattice site.

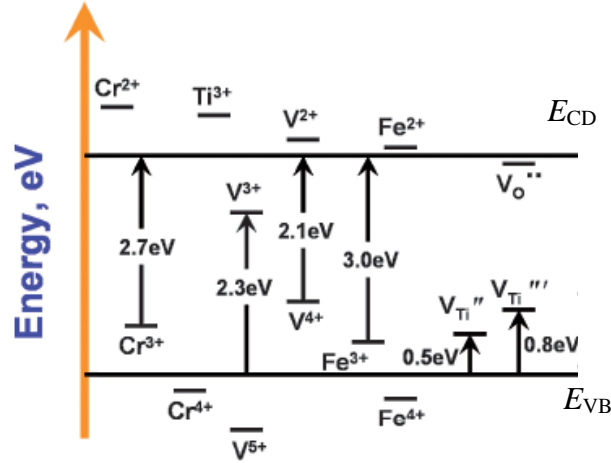


Fig. 6. Energy states in TiO_2 after being doped by Fe, Cr and V ions [143].

Similarly, for pentavalent dopants such as V^{5+} ,



where $V_{Ti}^{4\bullet}$ represents cation vacancies that are good hole acceptors (as shown in **Fig. 6**; after excitation, holes in the VB can be trapped at these sites to form V_{Ti}^{\bullet} and $V_{Ti}^{\bullet\bullet}$ states above the VB edge); M_{Ti}^{\bullet} denotes the defect sites that are good electron acceptors (upon acceptance of one or two photoelectrons, V^{4+} and V^{3+} states can be formed within the bandgap).

Although quite a large number of examples exist in the literature on materials exhibiting enhanced light absorption properties, it should be pointed out that the absorption of light is a necessary but not a sufficient condition to promote photocatalytic activity. It is important that metal-ion dopants can greatly alter the lifetime of photogenerated charge carriers and thus photocatalytic activities. At appropriate concentrations, the dopants can selectively trap one charge carrier and allow another one to reach the particle surface to be able to take part in the desired redox reactions. On the other hand, dopant ions can also act as recombination centers for the

photoelectrons and holes and thus decrease the photocatalytic performance. The frequently reported decrease in photoactivity of metal-ion-doped TiO₂ with increasing dopant concentration above a certain doping level is a good illustration of this phenomenon [143].

Many examples seemingly suggest that a direct relationship exists between the charge carrier lifetime and the photoactivity of metal-ion-doped photocatalysts. The longer the lifetime, the higher the photoactivity. However, such a statement should not be generalized because the relationship between the charge carrier lifetime and the photoactivity is not straightforward and unambiguous. For examples, photogenerated holes could be trapped either deeply or shallowly. Those deeply trapped holes that were rather long-lived exhibited almost no activity. On the other hand, shallowly trapped holes had strong activity. Moreover, there are also other effects caused by metal-ion doping on the photoactivity of catalysts, such as changes in the surface hydrophilicity, changes in the adsorption ability towards reactant molecules, changes in the thickness of the space charge region near the surface, etc. Sometimes, these factors may exhibit opposite effects when present simultaneously [143].

4.2. Mechanism of photoactivity of TiO₂ doped with nonmetal species

Compared with metal dopants, nonmetal dopants, such as carbon [15,144], sulfur [13], phosphorous [145] and nitrogen [11,12,146,147], may be more appropriate for the extension of the light absorbance of TiO₂ into the visible region because their impurity states are near the valence band edge, but they do not act as charge carriers, and their role as recombination centers might be minimized. Among all nonmetal-doped TiO₂ materials, N- and S-doped TiO₂ nanomaterials have been found to exhibit superior photocatalytic activity under visible light irradiation.

Generally, mechanisms of non-metal doped TiO₂ photocatalysis include (**Fig. 7**): narrowing band gap ($h\nu_1$: pure TiO₂; $h\nu_2$: non-metal doped TiO₂); facilitating electron transfer from the bulk of the TiO₂ structure to the surface region (reaction sites); and enhancing adsorption of contaminants (RH) [147].

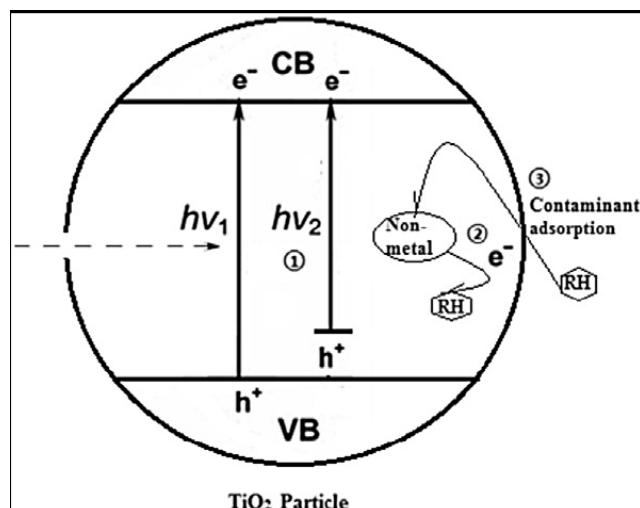


Fig. 7. Mechanisms of non-metal doped TiO₂ photocatalysis [147].

A high level of doping does not necessarily correspond to a high photocatalytic performance [148,149]. The dopant element, in fact, usually leads to active species for photocatalysis under visible light but, at the same time, it can form species having a detrimental effect on the material photoactivity [150].

4.2.1 Nitrogen doped TiO₂ (N-TiO₂)

Among anionic dopants, nitrogen is one of the most effective elements to promote visible light photoactivity. Due to atomic size comparable to oxygen, low ionization energy and high stability, nitrogen can be easily introduced in the TiO₂ structure.

Sato et.al [151] investigated the first non-metal doped TiO₂ in 1986 where they obtained N-TiO₂ powders from a commercial titanium hydroxide by calcination. The powders showed higher photocatalytic activity for oxidation of carbon monoxide and ethane than standard TiO₂ in the visible region. However, at that time, this result did not attract attention. Later on, Asahi et al. [152] reported the band-gap narrowing of titanium dioxide by nitrogen doping where they prepared TiO_{2-x}N_x films by sputtering the TiO₂ target in a N₂(40%)/Ar gas mixture and by treating anatase powder in the NH₃(67%)/Ar atmosphere at 600°C for 3 h. Since then, doping of titania by nitrogen has been intensively investigated.

The efficiency of N-TiO₂ under visible light depends on many factors: the synthesis procedure (sol-gel, ion implantation, magnetron sputtering, oxidation of titanium nitride, etc), dopant position and concentration [153], the crystal phase of the TiO₂ [154], the interaction between the N centers and oxygen vacancies [155], the intensity of light irradiance [27], the type of pollutants, etc. [23].

Recently, significant efforts are being devoted to investigating the structural, electronic and optical properties of N-doped TiO₂, understanding the underlying mechanisms and improving the photocatalytic and self-cleaning efficiency under visible and solar light [156,157].

4.2.1.1. *Electronic structure of nitrogen-doped TiO₂*

There are different opinions regarding the origin of visible-light absorption for nitrogen-doped TiO₂:

- a) *Band gap narrowing*: Asahi et al. [152] proposed that the narrowed band gap of TiO₂ contributes to the visible light absorption of nitrogen-doped TiO₂ by mixing O 2p states with the N 2p states (**Fig. 8A**) that cause elevating the valence band edge.
- b) *Impurity energy level*: Irie et al. [158] stated that TiO₂ oxygen sites substituted by nitrogen atom form isolated impurity energy levels above the valence band. Irradiation with UV light excites electrons in both the VB and the impurity energy levels, but illumination with visible light only excites electrons in the impurity energy level (**Fig. 8B**).
- c) *Oxygen vacancies*: Ihara et al. [159] suggests that the visible-light absorption of nitrogen-doped TiO₂ originates from the localized states of the oxygen deficiencies caused by nitrogen doping, observed at ~ 0.8 eV below the bottom of the conduction band [128], rather than from the nitrogen dopant itself (**Fig. 8C**).

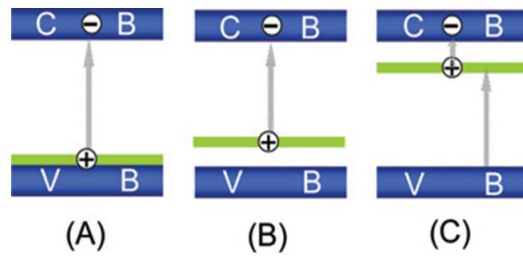


Fig. 8. The possible origin of visible light absorption in doped TiO₂ by non-metal doping [160].

4.2.1.2. Incorporation of nitrogen in TiO₂ matrix

Nitrogen can be incorporated into the crystal lattice either substitutionally or interstitially (**Fig. 9**).

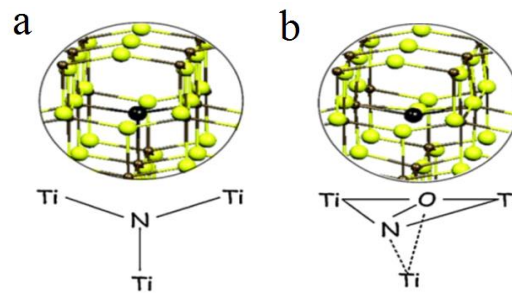
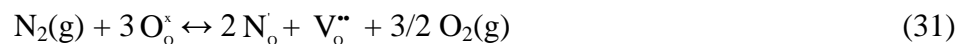


Fig. 9. Substitutional (a) and interstitial (b) incorporation of nitrogen in TiO₂ lattice [161]

In substitutional doping, nitrogen atom is bound to three Ti atoms and replaces lattice oxygen, where every two nitrogen sites create one oxygen vacancy in the lattice due to charge balancing. In the case of nitrogen gas as a source of nitrogen, reaction of vacancy creation can be written as:



Therefore, nitrogen incorporation promotes oxygen loss. The state of substitutional nitrogen appearing slightly above the valence band edge (0.14 eV) as shown in **Fig. 10** [17,162].

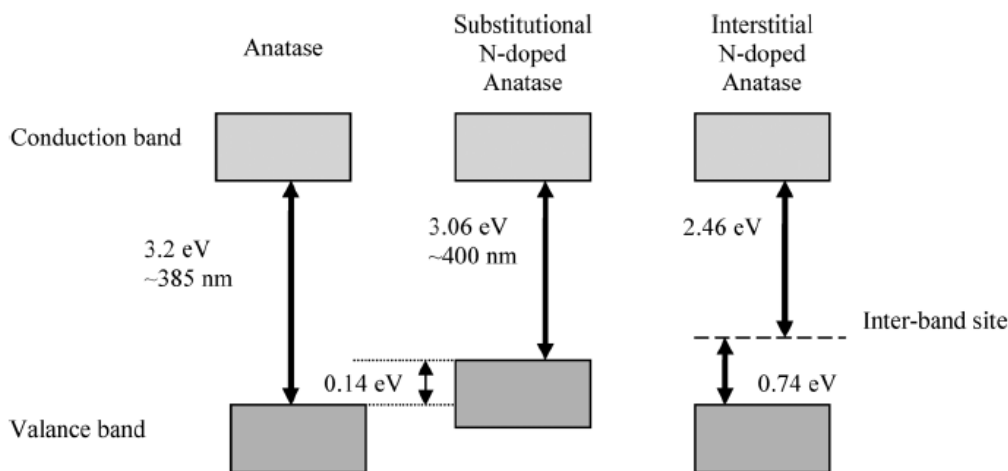
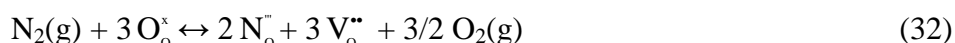


Fig. 10. Electronic band structure for: a) pure anatase, b) substitutional N-doped anatase, and c) interstitial N-doped anatase TiO₂ [163].

In interstitial doping (**Fig. 9b**), nitrogen binds to the oxygen forming N—O type bond surrounded by three atoms of Ti, where the NO bond generates localized states with π character. The two bonding states are deep in energy and lie below the top of O 2p band, while the two antibonding states lie above the O 2p band (0.74 eV), shown in **Fig. 10** as inter-band site. Some authors describe the interstitial nitrogen as Ti—O—N or Ti—N—O, but without defining a geometric arrangement of atoms [164].

The interstitial doping also creates oxygen vacancies, but the concentration is three times higher than in substitutional doping:



The binding energy ranges from 396 to 398 eV for substitutional nitrogen, and 400 to 406 eV for interstitial nitrogen [164,165].

The location of nitrogen doping in TiO₂ is critical to its behavior as a photocatalyst, but there is controversy regarding which position is most beneficial.

The state of N in titania depends upon the way it is introduced through several preparation methods/techniques. On the other hand, many reports have shown that a combination of both substitution and interstitial doping generally occurs during nitrogen doping of the TiO₂ lattices [166].

4.2.1.3. *Synthesis of nitrogen-doped TiO₂*

N-doped TiO₂ materials have been prepared by various methods, either physical (ion implantation [167,128], magnetron sputtering [168], chemical vapor deposition [169], annealing under N₂ or NH₃ flow at high temperatures (>550 °C) [170,171]) or chemical (solvothermal treatment [172], sol-gel synthesis [173], chemical treatment of TiO₂ [127], oxidation of titanium nitride). The most common methods for preparing N-TiO₂ powders are: the hydrolysis of organic and inorganic titanium compounds with ammonia water (sol-gel methods) followed by heating the resultant precipitates or their mixtures with urea [174,175], the nitridation of TiO₂ colloidal nanoparticles with alkylammonium salts at room temperature [23], the mechanochemical reaction of titania with hexamethylenetetramine or urea [24], the spray pyrolysis from a mixed aqueous solution containing TiCl₄ and nitrogen precursor [25], and the heat treatment of a TiO₂ precursor in an ammonia atmosphere [8,26,27,176].

The most versatile technique for the synthesis of N-TiO₂ powders is the sol-gel method, which requires relatively simple equipment and permits good control of the material's nanostructure, morphology and porosity. The incorporation of nitrogen in the TiO₂ matrix could be achieved by two ways:

- Adding of the dopant in the sol during the gelation stage [128].
- Synthesis of TiO₂ first, then nitrogen doping by using various nitrogen containing compounds (e.g. urea, thiourea, ethylamine and NH₃ or gaseous nitrogen at high temperatures [177-179]).

An often-used heat treatment of TiO₂ under NH₃ atmosphere as a nitrogen source has various advantages, such as no residual organic material and improvement of specific surface area [180].

Fang et al. [176] prepared N-doped TiO₂ photocatalysts by annealing two different precursors, P25 and a TiO₂ xerogel powder under NH₃/Ar flow at 500, 550, and 600 °C. The xerogel powder prepared by peptizing Ti(OH)₄ with HNO₃ was composed of nanoparticles and had large specific surface area. During the annealing process, the xerogel powder underwent increase in crystallinity, grain growth and phase transformation, whereas P25 did not show obvious changes. The N-doped TiO₂ photocatalysts obtained from the xerogel powder possessed higher concentrations of the

substitutional nitrogen and exhibited more obvious visible-light activities for photodegrading methylene blue than P25. The sample prepared at 500 °C achieved the best performances.

Mozia et al. [181] prepared N-doped TiO₂ photocatalysts by heating amorphous TiO₂ in gaseous NH₃ atmosphere at 200-100 °C. The photocatalytic activity of the investigated catalysts was determined on a basis of a decomposition rate of nonionic surfactant. N-doping narrowed the band-gap of TiO₂ in case of catalysts prepared at temperatures 800–1000 °C For catalysts prepared at temperatures 400–1000 °C an additional absorption edge in the vis-range occurred. The most photoactive catalysts were those obtained by calcination at 300, 500 and 600 °C.

Kang et al. [182] prepared N-TiO₂ by the grinding of TiO₂ in gaseous NH₃ at room temperature, followed by heating at low temperature as 200 °C for 60 min. The doping behaviors could be regulated by adjusting NH₃ amount and grinding periods and the rotational speed of planetary ball mill as well. NH₃ atmosphere helped to improve surface area due to the delay of aggregation, and post-heating treatment enhanced photocatalytic activity through improving of surface area by removal of surface impurities such as NH₃ and NH₄⁺ related compositions.

Balcerski et al. [183] prepared N-TiO₂ by high temperature ammonia treatment of anatase TiO₂. The TiO₂ powders were first treated between 500 and 600 °C under NH₃/Ar (80:20) gas flow at 1 atm for 3 h and then treated under air for 1 h. The N-doped TiO₂ powders were found to be active for the degradation of formic acid under visible light. However, the catalytic efficiency of the N-doped TiO₂ under UV light alone is less than that of the pure TiO₂ starting material. An optimal synthesis temperature of 550 °C can be seen as a balance point between catalyst crystallinity and the presence of defect sites that can absorb visible-light photons.

Chen et al. [26] synthesized N-doped and oxygen-deficient TiO₂ photocatalysts by heating commercial TiO₂ in NH₃ atmosphere, followed by a postcalcination process. The photocatalytic efficiency of the samples was analyzed by the degradation of gas-phase benzene under visible light irradiation. The NH₃ heat treatment of TiO₂ resulted in not only nitrogen doping but also creation of oxygen vacancies with optical absorption in visible-light region. The postcalcination is found to be positive by dramatically removing surface amino species, decreasing surface Ti³⁺ defects,

facilitating the generation of $O_2^{\bullet-}$ radicals, improving the separation of photogenerated carriers on the NH_3 treated catalyst and exhibiting a high visible-light activity toward benzene degradation. The photocatalytic conversion rate of benzene over the postannealed catalyst was much higher than that on the NH_3 -treated TiO_2 before postcalcination. The visible-light photoactive centers of doped TiO_2 were identified to be substitutional N species and oxygen vacancies.

4.2.1.4. *Synthesis and photoactivity of substitutional and interstitial N-doped TiO_2*

Preparation methods and conditions largely affect the position of N in the TiO_2 matrix [161]. In excess of oxygen and nitrogen, interstitial nitrogen doping is definitely preferred. However, under highly reducing conditions, as it is after annealing at high temperature, substitutional nitrogen species in parallel with oxygen vacancies could be favored.

Peng et al. [184] compared the photocatalytic properties of substitutional nitrogen doped TiO_2 prepared by physical method (calcination in ammonia) and interstitial nitrogen-doped TiO_2 , prepared by chemical method (microwave synthesis). Both substitutional and interstitial N can enhance the photoactivity of TiO_2 in visible light. Moreover, the visible light activity of interstitial N-doped TiO_2 is higher than that of substitutional N-doped TiO_2 .

Nitrogen-doped anatase titania nanobelts [185] are prepared via hydrothermal processing and subsequent heat treatment in NH_3 . Both the nitrogen content and the oxygen vacancy concentration increase with increasing the NH_3 treatment temperature. Nitrogen atoms were induced on the interstitial site at a low N doping level. It was shown that at 1.53 at % level, the interstitial sites became saturated and extra N atoms were located on the substitutional sites in the anatase lattice. The visible light responsive photoactivity of the N-doped titania originated from the excited electrons from the N 2p states on the edge of the valence band maximum (VBM) and the local N 2p levels above the VBM. The 3d states of Ti^{3+} below the conduction band, which were associated with oxygen vacancies, acted as the electron-hole recombination centers, leading to the reduction of photocatalytic activity.

Kalantari et al. [186] synthesized N-TiO₂ photocatalyst via a direct impregnation reaction using urea as nitrogen source, which was assisted by ultrasonic irradiation from TiO₂-P25 precursor. Nitrogen was effectively incorporated into the TiO₂ lattice as both substitutional and interstitial forms. N doping caused narrowing the band gap of the TiO₂ and a red shift in the absorption edge was observed toward visible light by formation of a new energy level in the TiO₂ band gap. The N-TiO₂ photocatalyst exhibited efficient photocatalytic activity for dibenzothiophene oxidation under the visible light irradiation compared with the TiO₂-P25. N doping resulted in a decrease in the crystallite size and an increase in the specific surface area of TiO₂.

Zeng et al. [17] prepared both substitutional and interstitial nitrogen doped TiO₂ by a simple annealing method, assisted by adjusting gas composition to control the positions of nitrogen dopants in TiO₂ lattice. The presence of oxygen in the atmosphere really affects the location of nitrogen dopant in the lattice. In this case, the nitrogen dopants favor to occupy the interstitial sites in the lattice. In pure NH₃, substitutional N-TiO₂ was formed.

The authors proposed, according to results and previous investigations, that the visible light response in the case of substitutional N-doped TiO₂, arise from occupied N 2p localized states which is located slightly above the valence band edge. In the case of interstitial N-doped TiO₂, the visible light response arise from occupied π^* character N-O localized states located slightly above the valence band edge. Both substitutional and interstitial N doped TiO₂ could respond to visible light, since the band gap of TiO₂ become narrow after annealing in NH₃ or NH₃/air mixture. Nonetheless, strong light harvesting does not mean excellent photocatalytic property. Many factors including phase structure, specific surface area, recombination rate of electron-hole pairs and crystalline size et al. can affect the photocatalytic performance. In the experiment, substitutional N-TiO₂ possessed higher photocatalytic activity than the interstitial N-TiO₂. The difference in photocatalytic activity is attributed to the different location of nitrogen in the lattice of TiO₂ and the proportion of surface hydroxyl group for the samples. For pure TiO₂, gaseous benzene cannot be decomposed under visible light illumination since the width of bandgap has not changed (**Fig. 11B**). However, both doped samples can respond to visible light since the band structure have been narrowed by nitrogen doping (**Fig. 11 A and C**). In **Fig. 11A**, the oxygen vacancy energy level

lies below the bottom of the conduction band and the N 2p state mixes with valence band for N-TiO₂, whereas, the isolated N_i-energy level is formed in interstitial N-TiO₂. The recombination of electron-hole pairs occurs in isolated Ni-energy level. In addition, the surface hydroxyl group plays an important role in improving photocatalytic activity. The proportion of surface hydroxyl group in substitutional N-TiO₂ was higher than that in interstitial N-TiO₂. Therefore, the substitutional N-TiO₂ possessed better photocatalytic property than interstitial N-TiO₂.

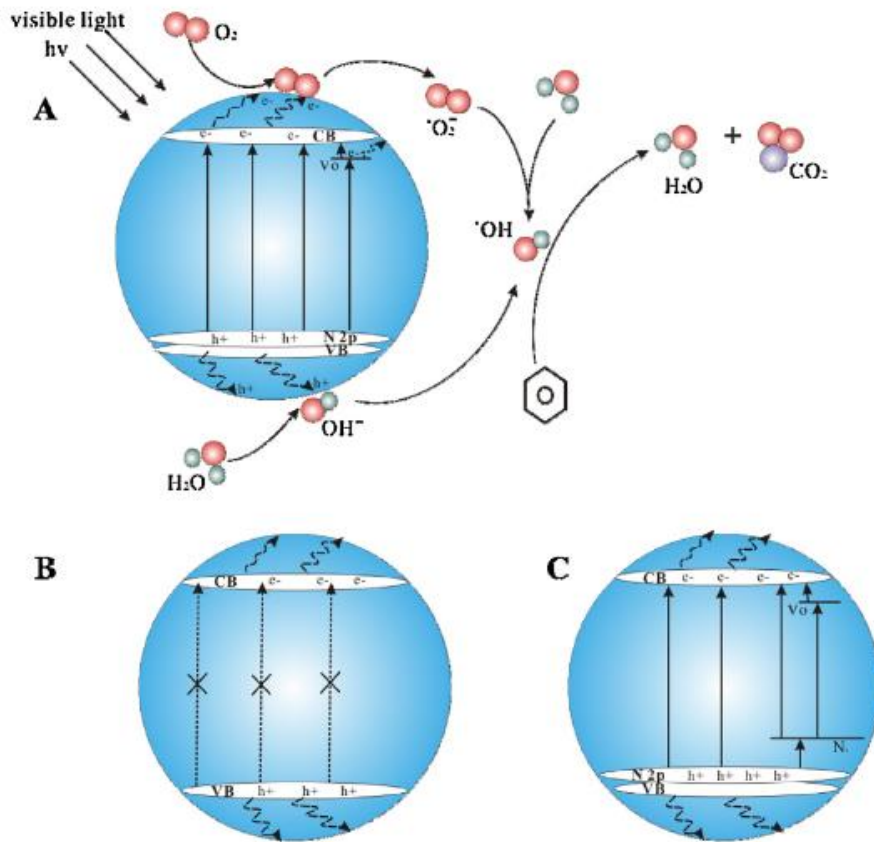


Fig. 11. Electronic band schematics of photocatalytic degradation of benzene for substitutional N-TiO₂ (A), pure TiO₂ (B) and interstitial N-TiO₂ [17].

4.2.2. Sulfur doped TiO₂ (S-TiO₂)

Sulphur doping into TiO₂ crystal structure has been widely studied as it produced alike band gap narrowing as observed in case of other non-metals doping.

4.2.2.1. *Chemical nature and structural location of sulphur in TiO₂*

The origin of the visible-light responsive S-doped TiO₂ still remains unclear because of several issues. The most important one concerns the chemical nature and the structural location (substitutional, interstitial, etc.) of the S-doping species responsible for the enhanced photoactivity. Some authors suggested that the observed red-shift of the optical absorption edge in S-doped TiO₂ is due to a band gap narrowing induced by a rigid shift of the valence band resulting from a mixing between S 3p and O 2p orbitals [18,187]. On the other hand, some authors have attributed the observed visible-light sensitization of S doped TiO₂ to an excitation from localized impurity states in the band gap to the conduction band [188,189-191]

Sulfur was detected as hexavalent (SVI⁺), tetravalent (SIV⁺), or sulfide (S²⁻), depending on the preparation condition and the sulfur precursor [192,193,18]. In cationic S-doped TiO₂, sulfur is incorporated as a SIV⁺/SVI⁺ cation, substituting Ti⁴⁺ to form Ti-O-S bonds [194]. The unit cell parameters decrease because of smaller ionic radius of SIV⁺/SVI⁺ compared to that of Ti⁴⁺. In anionic S-doped TiO₂, sulfur incorporated as S²⁻ anion, substituting the lattice oxygen to form O-Ti-S bonds [18,19]. Unit cell parameters increases due to larger ionic radius of S²⁻ compared to that of O²⁻. [195,196]. The binding energy is around 169.2 eV for SVI⁺ and around 163.6 eV for the S²⁻ species.

Successful insertion of anionic sulfur into the TiO₂ lattice is far more difficult to achieve than nitrogen, due to its larger ionic radius. The insertion of cationic sulfur (SVI⁺/SIV⁺) is chemically favorable over the anionic form (S²⁻) [43], because of smaller ionic radius of SIV⁺/SVI⁺ compared to that of Ti⁴⁺ [197]. It has also been proved that cationic S-doping of TiO₂ is much more stable than anionic doping and its exothermicity is significantly higher than for anionic doping. Consequently, the cationic doping appears as the most probable state, while anionic doping is metastable [190]. Irrespective of sulphur oxidation state, the photocatalytic activity was found to be enhanced.

4.2.2.2. *Synthesis and photoactivity of S-doped TiO₂*

S-doped titania powders have been synthesized by different methods, using different sources of sulfur.

In 2002, Umebayashi et al. [187] successfully synthesized S-doped TiO₂ by oxidation annealing of TiS₂ [10,17]. According to their report, the S atoms replaced O atoms and the S-doped TiO₂ showed optical absorption red-shift. The authors stated that the mixing of the S3p states with the valence band contributed to the band gap narrowing.

Later researches have shown parallel findings when taking TiS₂ or CS₂ as sulfur sources [21]. According to them, most of the sulfur in TiS₂ or CS₂ was oxidized and the residual sulfur would naturally remain as S²⁻ that favors the replacement of oxygen atoms in the O–Ti–O framework [144,13].

Sulfur-doped anatase TiO₂ nanoparticles with sulfur atoms occupying oxygen sites were also realized by low-temperature (120 °C) hydrothermal oxidation of titanium disulfide (TiS₂) with deionized water as the solvent [161]. The authors stated that S doping can effectively narrow the bandgap of TiO₂ because S 3p level is higher than O 2p orbital. The large surface area caused by this doping method induces higher photocatalytic activity in the visible regime compared with S-TiO₂ oxidized at high temperature.

On the contrary, Ohno and other groups [13] found that sulfur atoms were incorporated as cations and replaced Ti ions when taking thiourea or sulfate as sulfur sources in the S-doped TiO₂ nanopowders. They confirmed that the substitution of Ti⁴⁺ by S⁶⁺ was chemically more favorable than replacing O²⁻ with S²⁻, due to the different ionic radius among them.

Periyat et al. [198] successfully developed cationic S-doped TiO₂ through modification of titanium isopropoxide with sulphuric acid. Sulfur doping in high-temperature stabilized anatase titania was easily achieved by the decomposition of TiOSO₄ formed by the initial reaction between titanium isopropoxide and sulfuric acid. Sulfur-modified samples showed extended anatase phase stability up to 900 °C and increased visible light photocatalytic activity.

Cationic S–TiO₂ was also prepared by the reaction of titanium butoxide and thiourea in methanol [199]. It was showed, similar as in research of Periyat et al. [198], that anatase structure was stabilized up to 700 °C, as sulphate groups (from decomposition of thiourea) anchored on TiO₂ delayed the anatase to rutile transformation. In addition, the increase of the calcination temperature led to a decrease of the sulphur content. It caused a formal blue shift of the edge of corresponding diffuse reflectance spectra from visible to UV range.

Ma et al. [13] synthesized, by using electrospinning method, both cationic and anionic S-doped TiO₂ nanofibers, employing thiourea and CS₂ as the sulfur sources. In cationic S-doped sample synthesized by using thiourea, the crystalline reduced in size via Ti⁴⁺ substitution by S⁶⁺, because its smaller ionic radius compared to that of Ti⁴⁺. Similarly, the crystalline sizes increased when O²⁻ was substituted by S²⁻ in anionic S-doped sample synthesized by using CS₂. Both types of S-doped TiO₂ nanofibers showed significant photodegradation and mineralization of organic compounds. Results showed that photoinduced holes (h⁺) and chemisorbed hydroxyls (OH_{ads}⁻) on catalyst surface played a vital role in the photocatalysis obtained with thiourea, but photoinduced holes (h⁺) and electrons (e⁻) had the nearly equal importance in the case of samples synthesized with CS₂.

Abu Bakar et al. [191] prepared also both cationic and anionic S-doped TiO₂ via template free and low-temperature oxidant peroxide method (OPM) assisted hydrothermal treatments. As a sulphur source, thiourea was used for cation doping, while CS₂ was used for anionic doping, similar as in other researches. Similar as in the research of Ma et al. [13], the authors found that S⁶⁺ substituted for Ti⁴⁺ in cationic S-doped sample reduced the crystalline size due to a smaller ionic radius of S⁶⁺ as compared to Ti⁴⁺, whereas S²⁻ substitution for O²⁻ increased the crystalline sizes in anionic S-doped TiO₂ samples. The anionic S-doped TiO₂ photocatalysts showed higher photocatalytic activity due to reduced crystallite size and scavengers test revealed that holes and electrons played the nearly equal role for its higher photocatalytic activity. Whereas, in the case of cationic S-doped TiO₂ photocatalysts the creation of new impurity levels could be mainly responsible for enhanced higher photocatalytic efficiency due to oxidation of surface chemisorbed hydroxyl ions by photoinduced holes. Therefore, it was revealed that doping levels and degree of surface chemisorbed

hydroxylation are largely accountable for the enhanced photocatalytic activity of S-doped TiO₂ photocatalysts.

4.2.3. *Non-metal co-doping*

Although the monodoped nonmetal or metal atoms can obviously enhance photocatalytic performance, they always act as the recombination centers because of the partially occupied impurity bands. It has been recognized theoretically that codoping using two or more foreign atoms can passivate the impurity bands and decrease the formation of recombination centers by increasing the solubility limit of dopants [200].

Co-doped systems involve combinations of cations and anions [201] or two anions together within the oxide lattice that may modify conductivity and optical properties of titania or introduce new electronic states that may lie closely to conduction or valence band of titania. TiO₂ with an appropriate combination of nonmetals doping would result in more visible light sensitive photocatalysts for a desired application, because of the synergistic effect tuning the electronic structure [202,203].

The modified N-doped TiO₂ usually showed favorable effects for improving the photocatalytic activity in the range of visible light compared to N-doped TiO₂.

The (N,S)-co-doping TiO₂ can play a vital role in significantly improving photocatalytic activity because of the strong synergistic interaction between S and N, in which the surface separation of photoexcited electron-hole pairs is promoted. Consequently, the VB of TiO₂ shifts to a positive direction, which leads to higher oxidative ability and degradation ability towards pollutant under visible light irradiation [200]. Etacheri et al. further proved that the formation of isolated S 3p, N 2p, and π^* N-O states between the VB and CB was responsible for the visible light absorption (**Fig.12**) [204]. As it already stated, the energy states created by substitutional nitrogen (N 2p) is positioned 0.14 eV above the valence band, whereas interstitial nitrogen (π^* N-O) states lie higher in the gap at 0.73 eV. It is also reported that cationic S-doping creates an additional S 3p level positioned 0.38 eV above the valence band of TiO₂ (**Fig. 12**).

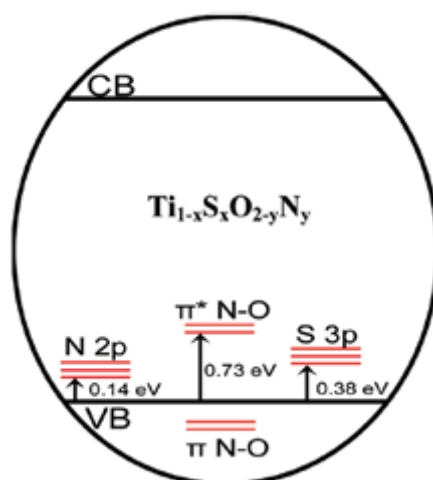


Fig. 12. Electronic structure of $\text{Ti}_{1-x}\text{S}_x\text{O}_{2-y}\text{N}_y$ [204].

N,S-co-doped TiO_2 materials have been usually prepared by addition of urea, thiourea or other N,S containing substances to the initial solutions containing titanium precursor [18,205], or by treatment of crystallized TiO_2 with such modifiers [206,207].

Naik et al. [208] synthesized sulfur and nitrogen incorporated mesoporous TiO_2 (SNT) nanocomposites by a template-free homogeneous coprecipitation of $\text{TiOSO}_4 \cdot x\text{H}_2\text{SO}_4 \cdot x\text{H}_2\text{O}$, thiourea, ethanol, and water. The photocatalytic activities of the catalysts were evaluated for the degradation of methyl orange and phenol under direct solar light. SNT shows about a 2-fold higher photocatalytic activity than singly N-doped or S-doped mesoporous TiO_2 and 3-fold higher than Degussa P25. The authors concluded that high visible-light-driven photocatalytic activity is mainly due to the narrowing of the band gap. High surface area, small crystallite size, wormhole mesoporosity with a narrow pore size distribution, and large pore volume are also the determining factors for the enhanced photocatalytic activity. Besides all of the above facts, the electronic environment of the SNT nanocomposites having N-Ti-O and O-Ti-NO environments is mainly responsible for visible light absorption. The presence of Ti^{3+} states produced through substitutional N-doping has also a leading role for high photocatalytic activity. Sulfate species anchored on TiO_2 as a cocatalyst contribute to an enhancement of surface acidity, separation and transfer of charge carriers, increase in surface area, inhibition of phase transformation, and hence contribute to an overall increase in the photocatalytic activity.

Yau et al. [209] prepared mesoporous N,S-co-doped TiO₂ by a solvothermal method starting from tetrabutyl orthotitanate and thiourea as the sources of the nitrogen and sulfur doping. The results confirm that N and S have been incorporated into the lattice of anatase TiO₂, N replacing O site and S replacing Ti site in anatase lattice, which brings an obvious red-shift of the absorption edge into visible-light region. Moreover, the codoped products exhibit high photocatalytic activity under the visible-light irradiation.

Zhang et al. [210] prepared the N,S-co-doped TiO₂ nanowires by a hydrothermal route, using titanium sulfate as a precursor and isopropanol as a protective capping agent. Photocatalytic activity evaluation demonstrated that the N,S-codoped TiO₂ NWs calcined at 600 °C exhibited the best photocatalytic performance for the degradation of atrazine under visible light irradiation and had a good ability of recyclable and cycling use. This benefit comes from the synergistic effect of N and S on narrowing the band gap and separating electron-hole pairs of photocatalysts, and prohibition of the anatase-to-rutile transformation temperature at 600 °C.

Behpour et al. [211] prepared homogeneous and transparent N,S-co-doped TiO₂ nanocrystalline thin films by sol-gel dip coating method using thiourea as a source of sulfur and nitrogen. The surface structure of the films was modified by addition of different concentrations of polyethylene glycol (PEG) into the TiO₂. The results showed only the anatase TiO₂ was formed in both film and powder and N,S-codoping led to lower crystallite size, red-shift absorption and high photocatalytic activity under irradiation of both visible and sun light.

Ju et al. [212] prepared successfully N,S-co-doped TiO₂ photocatalysts at a nanometer scale by hydrothermal process, and photocatalytic activity of the obtained powders for degradation of methyl orange under sunshine irradiation was studied. Experimental results indicate that the nitrogen was incorporated into the lattice of TiO₂ substitutionally or interstitially, while sulphur existed as S^{VI+}. The incorporation was responsible for narrowing the band gap of TiO₂ and shifting its optical response from ultraviolet to the visible-light region.

Yu et al. [213] prepared highly photoactive nanocrystalline mesoporous N,S-co-doped TiO₂ powders by hydrolysis of Ti(SO₄)₂ in a NH₃·H₂O solution at room temperature. The photocatalytic activity was evaluated for the photocatalytic oxidation

of acetone and formaldehyde under UV light and daylight irradiation in air, respectively. The results showed that the as-prepared TiO₂ powders exhibited a stronger absorption in the UV–vis light region and a red shift in the band gap transition due to N,S-co-doping. Sulphur was incorporated anion and cation, while nitrogen was interstitially incorporated. The photocatalytic activities of the as-prepared N,S-co-doped TiO₂ powders calcined at a temperatures 400–700 °C were higher than that of commercial Degussa P25. The high activities of the N,S-co-doped TiO₂ can be attributed to the results of the synergetic effects of strong absorption in the UV–vis light region, red shift in adsorption edge, good crystallization, large surface area and two phase structures of undoped TiO₂ and N,S-co-doped TiO₂.

N,S-co-doped titania powders were also prepared by thermal treatment of TiO₂ with N,S-containing substances, thiourea and ammonium thiocyanate and the properties of the obtained powders were compared with the N-doped TiO₂, synthesized by using urea. The N and S were introduced preserving the crystalline structure, morphology and specific surface area of the initial TiO₂. The level of N,S-co-doping varied depending on the modifier. In all samples, N was found interstitially incorporated in the TiO₂ lattice. S was recorded in ionic states S^{VI+} and S^{IV+}. All modified powders exhibited enhanced visible light absorption and narrower energy band gap in comparison to the initial titania. The photocatalytic activity in NO_x oxidation under UV light decreased after doping, while the activity under visible light did not increase for all modified samples. This outcome was related to the high level of N and S doping and intense e⁻-h⁺ recombination on dopants sites. The activity of the photocatalysts in NO_x oxidation processes was also connected to the type of non-metal dopant in the lattice of TiO₂. The beneficial effect of N-doping was ascribed to the preferential formation of •OH species on N-doped surface, whereas the detrimental effect of N,S-co-doping was credited to the suppressed •OH production on S-doped surface.

EXPERIMENTAL PART

5. Experimental procedure

5.1. Materials and reagents

The following reactants of p.a. grade were used for the titania synthesis:

- Titanium(IV) chloride (TiCl_4) produced by Sigma-Aldrich
- Titanium(IV) isopropoxide ($\text{Ti}(\text{OiPr})_4$) produced by Sigma-Aldrich
- Dimethyl sulfoxide (DMSO) produced by Sigma-Aldrich
- Carbon tetrachloride (CCl_4) produced by Acros Organic
- Chloroform (CHCl_3) produced by Merck and
- Cyclohexane (C_6H_{12}) produced by Merck

The azo dye C.I. Reactive Orange 16 (RO16) was used in the photocatalytic experiments, as a model for dissolved organic substances. It was obtained from CHT/Bezema (commercial name Bezaktiv Orange V-3R) and used without any purification. The structure of the dye is shown in **Fig. 13**, and the general characteristics are presented in **Table 2**.

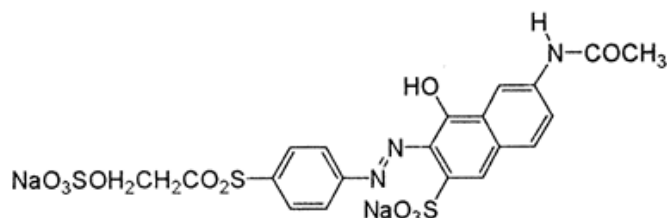


Fig. 13. The structure of dye C.I. Reactive Orange 16

Table 2. The general characteristics of dye C.I. Reactive Orange 16 (λ_{max} - the wavelength of the most intense UV/Vis absorption, M_w – molecular weight)

Chemical formula	IUPAC name	λ_{max} (nm)	M ($\text{g}\cdot\text{mol}^{-1}$)	Appearance
$\text{C}_{20}\text{H}_{17}\text{N}_3\text{Na}_2\text{O}_{11}\text{S}_3$	disodium (3Z)-6-acetamido-4-oxo-3-[[4(2-sulfonatoxyethylsulfonyl)phenyl]hydrazinylidene]naphthalene-2 sulfonate	494	617.5	Red powder

Three types of water were used in the photocatalytic experiments:

- deionized water (DIW), produced by Milipore Waters Milli Q purification unit, resistance 18 M Ω cm
- natural seawater (SW), obtained off the coast of Greece and passed through 2 μ m filter, and
- artificial seawater (ASW)

The concentration of major cations and anions in natural seawater was determined on a Metrohm ion chromatography instrument, 861 Advanced Compact IC MSM II and the results are presented in **Table 3**. The instrument specifications are: conductivity detector with chemical suppression; controlled flow ranging from 0.2 to 2.5 cm³·min⁻¹; maximum pressure of 35 MPa. The columns specifications are: Metrosep A Supp 5-150 (for anion analysis), anion eluent - 3.2 mmol Na₂CO₃/1.0 mmol NaHCO₃; Metrosep C2-150 (for cation analysis), cation eluent - 4 mmol taric acid/0.75 mmol dipicolinic acid; suppressor solution - 50 mmol H₂SO₄. Prior to the analysis, all samples were filtered through 0.45 μ m filters and degassed in the S100 ELMASONIC ultrasonic bath. The standard solutions were prepared from deionized water and the standard ion solutions.

Table 3. Ionic composition of NSW

Ion	Concentration (mmol·dm ⁻³)
Cl ⁻	564.1
Na ⁺	488.9
K ⁺	8.74
Mg ²⁺	45.22
Ca ²⁺	8.56
SO ₄ ²⁻	27.91

The quantities of salts for ASW preparation were calculated according to the composition of NSW given in **Table 3**. The prepared ASW had the following composition: 488.9 mmol·dm⁻³ NaCl, 8.74 mmol·dm⁻³ KCl, 25.91 mmol·dm⁻³ MgCl₂·6H₂O, 19.36 mmol·dm⁻³ MgSO₄·7H₂O and 8.56 mmol·dm⁻³ CaSO₄.

5.2. Synthesis of undoped TiO₂ powders

Undoped TiO₂ powders were prepared by the non-hydrolytic sol–gel method coupled with solvothermal treatment, starting from TiCl₄ and Ti(OⁱPr)₄, by using different solvents: CCl₄, CHCl₃ or C₆H₁₂. The reactants were mixed in the molar ratio 1:1:1 (10 cm³ Ti(OC₃H₇)₄, 3.7 cm³ TiCl₄ and 3.3 cm³ solvent) in a glove box under a protective atmosphere of nitrogen. The initial experimental stage comprised the mixing of Ti(OiPr)₄ and solvent, followed by adding of TiCl₄, drop by drop. The obtained mixture was subsequently heated in an autoclave, in the presence of excess solvent (45 cm³), at 160 °C for 3 h in order to form a gel. The so-synthesized gels were dried at 100 °C under a nitrogen flow and the dry gels were denoted as G160(CCl₄), G160(CHCl₃) or G160(C₆H₁₂), according to the temperature of gelation and the solvent used in the synthesis. All gels were dark-brown.

The dry gels were annealed in air atmosphere, at different temperatures ($T = 350, 400$ or 500 °C) for 3 h to obtain undoped titania powders (P160/T(CCl₄), P160/T(CHCl₃) or P160/T(C₆H₁₂)). The denotation of the powders includes letter P (powder), temperature of gelation (160 °C), temperature of annealing (350, 400 or 500 °C) and solvent used in the synthesis (CCl₄, CHCl₃ or C₆H₁₂). All the obtained powders presented a typical bright white color.

5.3. Synthesis of doped TiO₂ powders

5.3.1. Doping by sulfur

Sulfur-doped TiO₂ was synthesized by the same procedure as undoped ones (section 5.2), only the solvent was DMSO, used as a source of sulfur, and the gelation temperature was 200 °C (gel G200(DMSO)) [214]. As in the case of undoped titania, the dry gel was annealed in air at 500 °C for 3 h, and the obtained white powder was denoted as P200DS (P – powder, 200 – temperature of gelation, DS – doped by S).

5.3.2 Doping by nitrogen

5.3.2.1. Annealing in ammonia flow

For nitrogen doping, gels G160(C₆H₁₂) and G200(DMSO) were annealed in ammonia flow, in a tube furnace [214]. Initially, the air in the furnace was pumped out by flow of nitrogen for 60 min and then ammonia flowing was stabilized at a rate of 200 cm³·min⁻¹. Afterwards, the furnace was heated from room temperature to 500 °C and annealing at this temperature lasted 3 h, followed by natural cooling to room temperature under the NH₃ gas. Both obtained powders were black.

The same procedure of annealing was applied for the undoped powder P160/500(C₆H₁₂), and dark yellow powder was obtained [214].

5.3.2.2. Post-annealing in air

The black powder obtained by G160(C₆H₁₂) annealing in ammonia flow was post-annealed in a static air atmosphere, at different temperatures ($T = 350, 400$ or 450 °C), during 30 or 60 min. The obtained powders were denoted as P160DN/T(30 or 60 min).

The powders obtained by G200DMSO and P160/500(C₆H₁₂) annealing in ammonia flow were further annealed in a static air atmosphere at 400 °C for 30 min and denoted as P200DNS (doping by N and S) and P160PDN (powder doped by N), respectively.

5.3.2.3. Annealing in ammonia flow followed by annealing in air flow

To avoid the two-step process of annealing and post-annealing in two furnaces, the gel G160(C₆H₁₂) was annealed and post-annealed in a tube furnace. First, annealing was performed in ammonia flow at 500 °C for 3 h, and then the temperature was lowered to 400 °C, where the ammonia flowing was stopped and the stream of air was turned on at the same flow rate as ammonia. In the air stream, annealing was performed

for 30 or 60 min. The obtained TiO₂ powders were denoted as P160DN^{*}(30min) and P160DN^{*}(60min), respectively.

5.3.2.4. *Annealing in a mixture of air and ammonia*

The gel G160(C₆H₁₂) was annealed in a tube furnace, in a mixture of air and ammonia, at ratio 1:3, 1:5 or 1:15. The obtained black powders were further annealed at 400 °C for 30 min in a static air atmosphere and denoted as P160DNR₁, P160DNR₂ and P160DNR₃, respectively.

5.4. Characterization methods

5.4.1. X-ray diffraction (XRD) analysis

The phase composition of the samples was determined by a BRUKER D8 ADVANCE, with a Vario 1 focusing primary monochromator (CuK α 1 radiation, λ = 1.54059 Å). The average crystallite size was determined by using the Scherrer's equation:

$$D = \frac{K\lambda}{\beta \cos\theta} \quad (33)$$

where:

λ is wavelength of X-ray radiation,

β is the width of the X-ray diffraction line at its half maximum,

K is the Scherrer constant and

θ is the angle of diffraction

5.4.2. Nitrogen adsorption-desorption isotherms

The specific surface area, pore volume and pore size distribution of the samples were determined according to nitrogen adsorption–desorption isotherms obtained at ~

196 °C by using a Micrometrics ASAP2020. Before the measurements, the samples were degassed at 150 °C for 10 h under the reduced pressure (< 1 Torr). The specific surface area was calculated according to (BET) method (S_{BET}) from the linear part of the nitrogen adsorption isotherm.

Calculation of the specific surface area is based on the direct application of the Brunauer, Emmett, Teller (BET) equation:

$$\frac{p}{V(p_0 - p)} = \frac{1}{V_m c} + \frac{(c-1)}{V_m c} \frac{p}{p_0} \quad (34)$$

where:

- p is the partial pressure of the adsorbate (Pa)
- p_0 is saturation vapor pressure of the adsorbate (Pa)
- V is volume of gas adsorbed at standard temperature and pressure (273.15 K and atmospheric pressure)
- V_m is volume of gas adsorbed at standard temperature and pressure to produce an apparent monolayer on the sample surface
- c is a constant equal to the quotient of the molar enthalpy of the adsorbate and the universal gas constant multiplied with T at which adsorption takes place

The dependence of $1/V[(p_0/p)-1]$ of p/p_0 is usually linear in the range $0.05 \leq p/p_0 \leq 0.35$. The value of the slope and the intercept of the line are used to calculate V_m and the c constant. The specific surface area, S_{BET} , of the powder is calculated from the equation:

$$S_{\text{BET}} = \frac{V_m \cdot N \cdot A}{M} \quad (35)$$

where:

N is Avogadro's number, $6.02 \cdot 10^{23}$ (mol⁻¹)

M is the molar mass of nitrogen (g·mol⁻¹)

A is a cross section of nitrogen molecule ($16.2 \cdot 10^{-20}$ m²).

The total pore volume (V_t) was given at $p/p_0 = 0.998$. The volume of the mesopores (V_{meso}) and the pore size distribution were determined according to the Barrett, Joyner and Halenda (BJH) method from the desorption isotherm.

5.4.3. *Field emission scanning electron microscopy (FESEM)*

The morphology of the powders was characterized by a Tescan MIRA3 FESEM, with the electron energies of 20 kV in a high vacuum. The samples were coated with thin layer of Au/Pd using a standard sputtering technique.

5.4.4. *Transmission electron microscopy (TEM) and high-resolution transmission electron microscopy (HR-TEM)*

The TEM and HR-TEM micrographs were obtained using a Jeol JEM-2010 operating at 200 kV. The samples were prepared by dispersing the material in ethanol. A drop of the dispersion was placed on a carbon coated copper grid and they were let to dry under ambient condition. The Digital Micrograph 3.7.1 software was used for the micrographs analysis.

5.4.5. *X-ray photoelectron spectroscopy (XPS)*

The XPS analyses were carried out on the PHI-TFAXPS spectrometer produced by Physical Electronics Inc. The samples in the form of powders were pressed onto an adhesive carbon tape. The sample surfaces were excited by X-ray radiation from monochromatic Al source at the photon energy of 1486.6 eV. During data processing the spectra were aligned by setting the C 1s speak at 284.6 eV, characteristic for C–C/C–H bonds. The high-energy resolution spectra were acquired with energy analyzer operating at the resolution of about 0.6 eV and the pass energy of 29 eV. The accuracy of binding energies was about 70.3 eV. The quantification of the surface composition was performed from XPS peak intensities taking into account the relative sensitivity factors provided by instrument manufacturer. The XPS spectra were fitted using the Gaussian-Lorentzian functions.

5.4.6. Fourier transform infrared (FTIR) spectroscopy

The FTIR analysis was performed on a MB BOMAN HARTMANN 100 instrument in the wave number range from 4000 to 400 cm^{-1} . The samples were prepared by the KBr disc method, at the sample: KBr ratio of 1:100.

5.4.7. UV–Vis diffused reflectance spectra

The UV–Vis diffuse reflectance spectra were recorded on a Shimadzu 2600UV–Vis spectrometer with an integrating sphere attached and using BaSO_4 as a reference. The spectra were recorded in the wavelength range 300–600 nm. The diffuse reflectance measurements were converted into the equivalent absorption coefficient by applying the transformation based on the Kubelka–Munk function (Eq. (36)):

$$F(R_\infty) = \frac{(1 - R_\infty)^2}{2R_\infty} \quad (36)$$

where $R_\infty = R/R_{\text{ref}}$ is the reflectance of the sample.

The band gap energy was determined using the Tauc plot of the transformed Kubelka-Munk function of $[F(R_\infty)h\nu]^{1/2}$ (for the indirect energy transition) versus the photon energy $h\nu$, by extrapolation of the linear part of the curve to the $F(R_\infty)=0$ [215,216].

5.5. Photocatalytic activity determination under UV and visible light

A batch –type quartz reactor (cylindrical shape, inner diameter 4 cm, volume 50 cm^3) was used for the catalytic runs. The setup was in a closed housing to prevent the external light effect. The reactor had a water-cooling jacket, and the illumination was provided by a Philips HPR 125 W lamp (having the strongest emission wavelength of 364 nm). The lamp was placed 10 cm from the surface of the reaction mixture. For the

visible light, an appropriate filter (GG400 Farbglas SCHOTT), which cuts off the wavelength below 400 nm, was placed on top of the reactor at about 20 cm above the liquid level. The catalyst's suspended form was sustained by using a magnetic stirrer (500 rpm) (Fig. 14).

The photocatalytic efficiency of the titania powders was investigated in the process of degradation of dye C.I. Reactive Orange 16 (RO 16), at the dye concentration of $50 \text{ mg}\cdot\text{dm}^{-3}$ for experiments with UV light and $20 \text{ mg}\cdot\text{dm}^{-3}$ for experiments with visible light. The concentration of TiO_2 powder was $1 \text{ g}\cdot\text{dm}^{-3}$. In all the experiments, 25 cm^3 of the dye solution and 25 mg of the titania powder were placed in the reactor, mixed ultrasonically for 10 min, followed by magnetic stirring for 30 min in dark, to attain the adsorption/desorption equilibrium. The concentrations of dye in the starting solutions and the concentrations of the dye remaining in the solutions after stirring in dark and after 15, 30, 45, 60, 75 and 90 min of irradiation were determined by UV–Vis spectroscopy (Shimadzu UV-160A 145 instrument). The solutions for UV–Vis spectroscopy analysis were prepared by passing the solution through a syringe filter (pore size of 0.22 μm) in order to remove the particles of the photocatalyst.

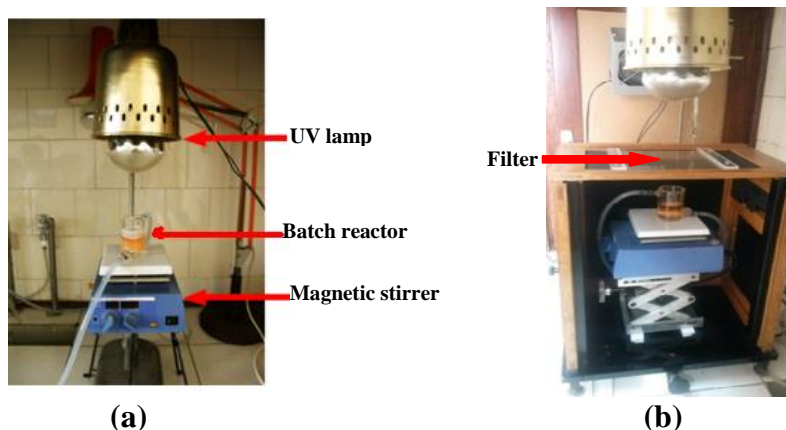


Fig. 14. Experimental set-up used for the photodegradation of RO16 under: (a) UV light, (b) visible light.

The photocatalytic experiments were performed:

- at initial dye concentrations 20, 40, 60, 80 and $100 \text{ mg}\cdot\text{dm}^{-3}$, in deionized (DIW), natural (NSW) and artificial (ASW) sea water; in order to compare the efficiency under UV light of titania P160/500, previously synthesized by non-hydrolytic sol-gel process with CCl_4 as a solvent [7], with the efficiency

of commercial powder P25 at initial dye concentration $50 \text{ mg}\cdot\text{dm}^{-3}$ in order to compare the efficiency of titania powders synthesized by using different solvents and annealed at different temperatures, under UV light

- at initial dye concentration $20 \text{ mg}\cdot\text{dm}^{-3}$ in order to compare the efficiency of doped titania powders under visible light.

6. Results and discussion

6.1. Comparison of photocatalytic efficiency of powder P160/500 synthesized by nonhydrolytic sol-gel method and commercial P25

In this dissertation, non-hydrolytic sol-gel method coupled with the solvothermal process [7] was applied to synthesized doped TiO₂ powders, since the previous investigations proved that this method produces mesoporous, nanocrystalline pure TiO₂ powders of narrow particle and pore size distribution, with the activity under UV light comparable to the activity of commercial powder Degusa P25. In order to confirm high photocatalytic efficiency of such synthesized powder P160/500 [7] at different conditions, the photocatalytic experiments with P160/500 and P25 were performed at different concentrations of dye RO16 in three types of water, DIW, NSW and ASW.

Photocatalytic activity is usually investigated in deionized water, but the photocatalyst efficiency could greatly depend on the environmental factors, in other words, some components found in the processed water may affect the photocatalyst efficiency [217-219]. Saline waters were chosen for testing of P160/500 and P25 photocatalytic activity due to its high content of ions and some other compounds, i.e. organic matter, which can influence the activity of photocatalysts.

Specific surface area of P-25 is 45.7 m²·g⁻¹, the pore volume is 0.177 cm³·g⁻¹, the average pore size is 7.57 nm, the crystalline size is 29.5 nm and it consists of 72.7 % anatase and 27.3 % rutile [220], while the point of zero charge, pH_{PZC}, is 6.4 [221]. Powder P160/500 consists of pure anatase and its specific surface area is 52.8 m²·g⁻¹, the average pore size is 11.1 nm, the pore volume is 0.209 cm³·g⁻¹ and the crystalline size is 26.4 nm [7]. The point of zero charge [222] of P160/500 is 6.5. Scanning electron micrographs (SEM) of the titania powders are presented in **Fig. 15**.

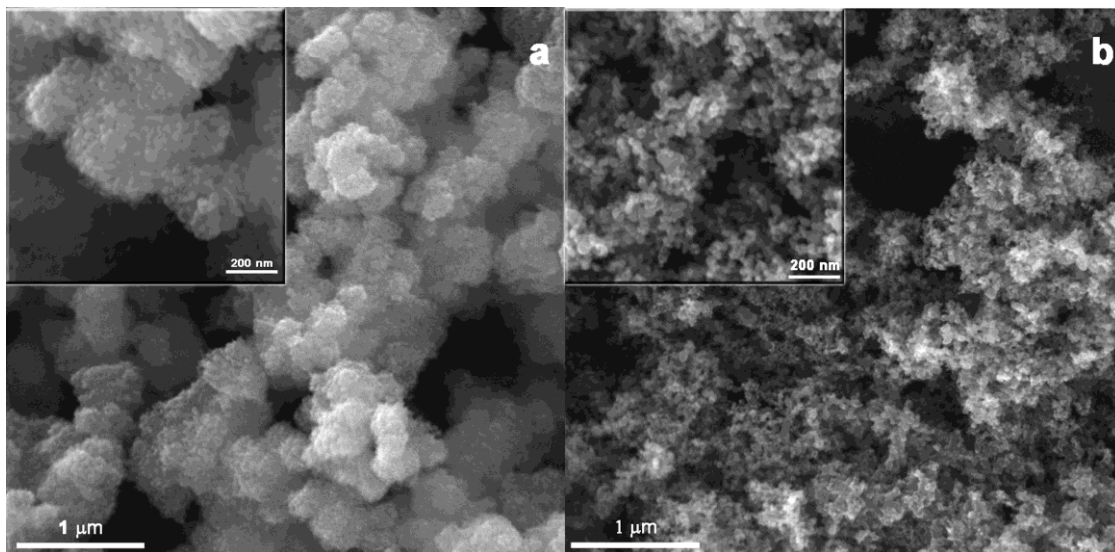


Fig. 15. Scanning electron micrographs (SEM) of: a) P160/500 and b) P25.

6.1.1. *The comparison of the photocatalysts efficiency in different types of water*

The results of photodegradation of dye in DIW, NSW and ASW by P25 and P160/500 are presented as a dependence of normalized concentration, $C/C_0 = C/C_{\text{dark}}$, vs. time illumination t , where C_{dark} is the concentration of RO16 after 30 min stirring in dark and C is the concentration of RO16 after illumination time t (**Figs. 16** and **17**). The dependences of $-\ln(C/C_{\text{dark}})$ vs. t for data in **Figs. 16** and **17** are linear (insets of **Figs. 16** and **17**), as confirmed by the value of correlation coefficient R^2 almost equal to 1 (**Tables 4-6**). The derived k_{app} values (Eq. 17) corresponding to their respective initial dye concentration, C_0 , is also presented in **Tables 4-6**.

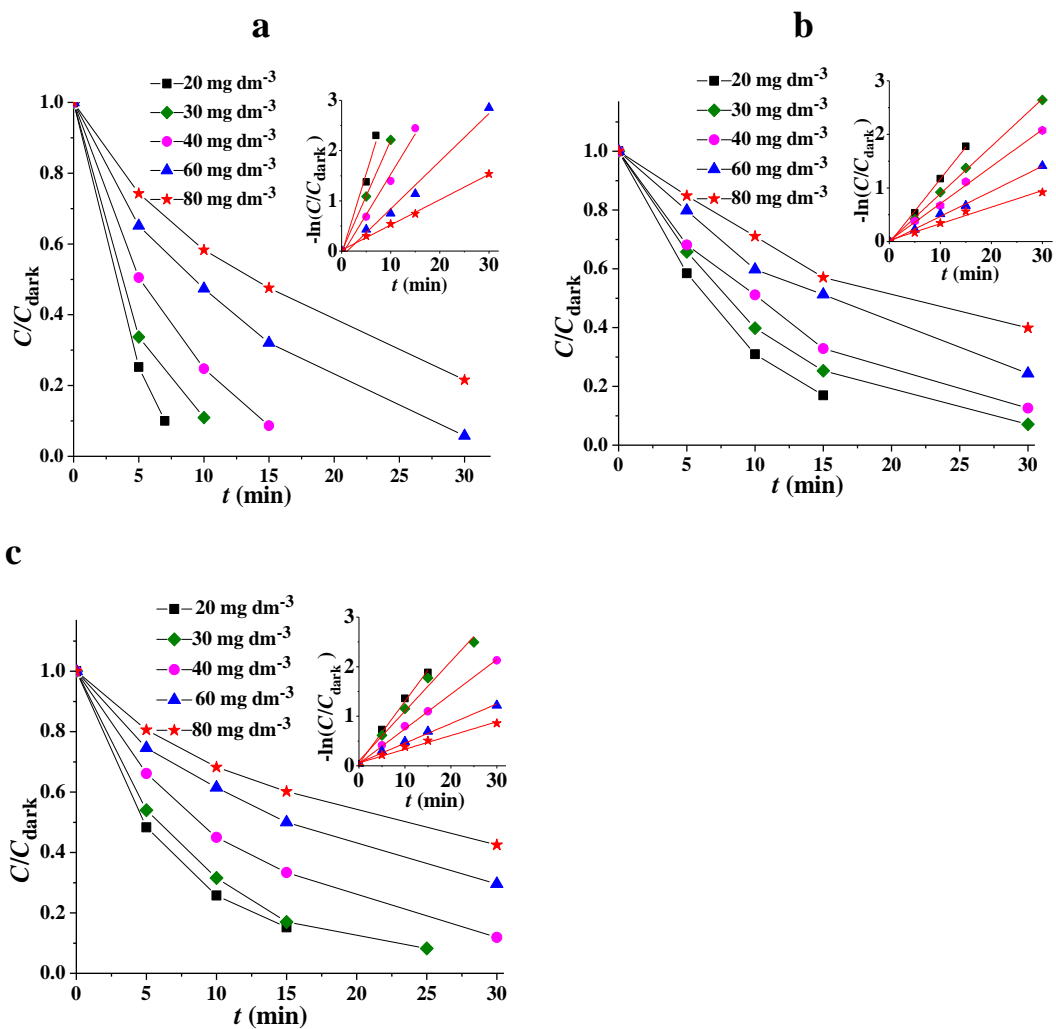


Fig. 16. Photocatalytic degradation of dye RO16 by P25 powder in: a) DIW, b) NSW and c) ASW (UV irradiation at room temperature; P25 concentration was 1 g·dm⁻³). The corresponding linear plots of the photocatalytic decolorization kinetics are given in the insets.

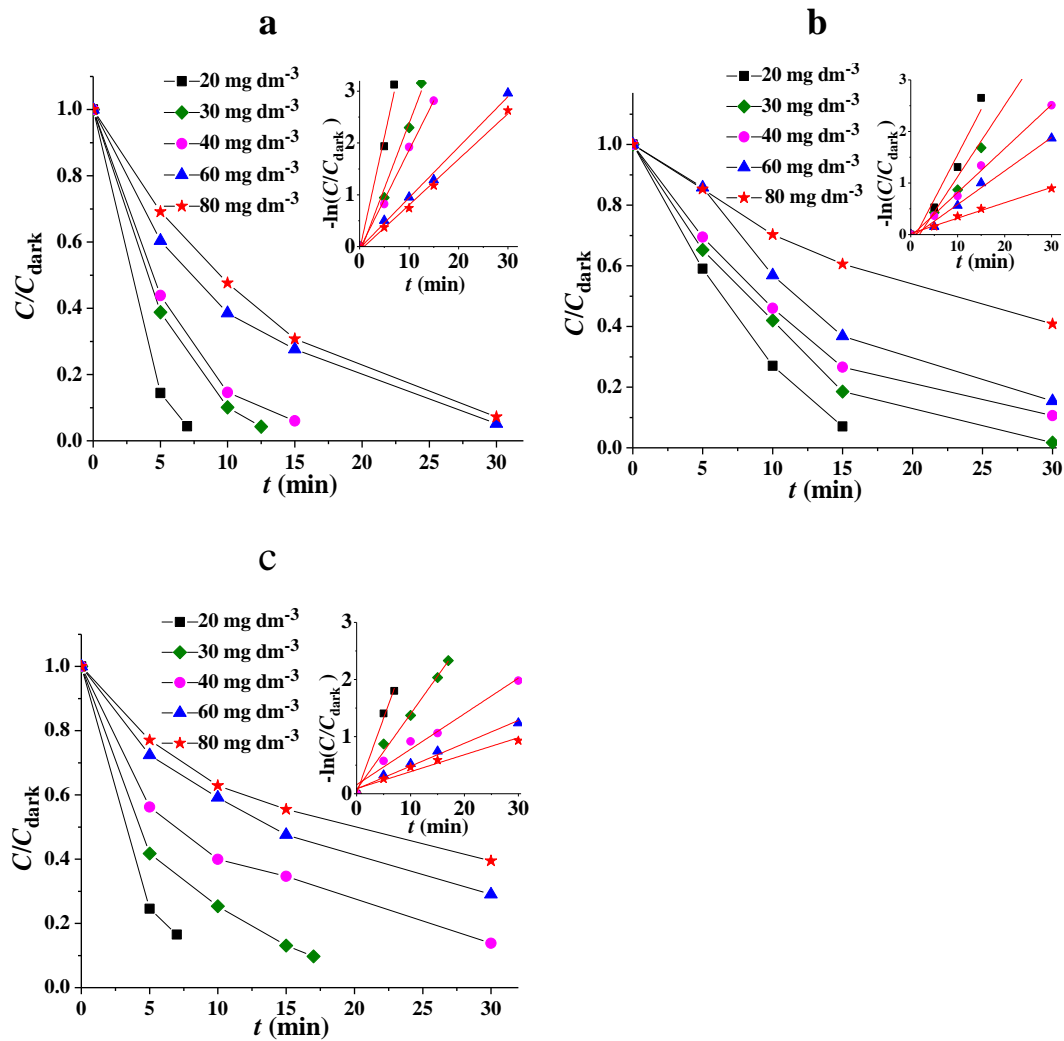


Fig. 17. Photocatalytic degradation of dye RO16 by P160/500 powder in: a) DIW, b) NSW and c) ASW (UV irradiation at room temperature; P160 concentration was $1 \text{ g} \cdot \text{dm}^{-3}$). The corresponding linear plots of the photocatalytic decolorization kinetics are given in the insets.

Table 4. The k_{app} values of photodegradation of RO16 by P25 and P160/500 in DIW depending on the initial dye concentration (UV irradiation at room temperature; TiO_2 concentration was $1\text{ g}\cdot\text{dm}^{-3}$)

Type of titania	P25		P160	
C_0 ($\text{mg}\cdot\text{dm}^{-3}$)	k_{app} (min^{-1})	R^2	k_{app} (min^{-1})	R^2
20	0.3109	0.9902	0.4267	0.9934
30	0.2207	0.9999	0.2389	0.9917
40	0.1545	0.9936	0.1874	0.9983
60	0.0898	0.9887	0.0962	0.9966
80	0.0512	0.9988	0.0846	0.9959

Table 5. The k_{app} values of photodegradation of RO16 by P25 and P160/500 in NSW depending on the initial dye concentration (UV irradiation at room temperature; TiO_2 concentration was $1\text{ g}\cdot\text{dm}^{-3}$)

Type of titania	P25		P160	
C_0 ($\text{mg}\cdot\text{dm}^{-3}$)	k_{app} (min^{-1})	R^2	k_{app} (min^{-1})	R^2
20	0.1173	0.9902	0.1590	0.9671
30	0.0890	0.9995	0.1260	0.9810
40	0.0700	0.9926	0.0827	0.9974
60	0.0470	0.9887	0.0620	0.9915
80	0.0322	0.9988	0.0310	0.9955

Table 6. The k_{app} values of photodegradation of RO16 by P25 and P160/500 in ASW depending on the initial dye concentration (UV irradiation at room temperature; TiO_2 concentration was $1 \text{ g}\cdot\text{dm}^{-3}$)

Type of titania	P25		P160	
C_0 ($\text{mg}\cdot\text{dm}^{-3}$)	k_{app} (min^{-1})	R^2	k_{app} (min^{-1})	R^2
20	0.1299	0.9969	0.2651	0.9973
30	0.1062	0.9917	0.1380	0.9964
40	0.0723	0.9980	0.0699	0.9774
60	0.0426	0.9908	0.0441	0.9841
80	0.0306	0.9831	0.0341	0.9683

From the results presented in **Figs. 16** and **17**, it can be seen that the efficiency of photocatalytic degradation of RO16 by both P25 and P160/500 in DIW, NSW and ASW decreases as the initial concentration increases, which is in good agreement with decreasing trend of k_{app} values, shown in **Tables 4-6**. This can be explained in terms of the saturation of limited number of accessible active sites on photocatalytic surface. When dye concentration is increased, the amount of dye adsorbed on the catalyst surface also increased, resulting in a reduction of light intensity reaching the photocatalyst [223], since the absorption of RO16 [224] well matches the absorption of titania [220] in the UV part of spectrum. The absorption edge of titania powders is 387 nm [220], while the RO16 has three absorption bands in the UV region, centered at 388 nm, 302 nm and 254 nm [224].

Both photocatalysts showed the highest photocatalytic activity in DIW, where the dye concentration decreased more rapidly with time than in NSW and ASW, as seen in **Figs. 16** and **17**. Consequently, k_{app} values are much higher for the dye photodegradation in DIW than in SW and ASW. The observed decrease of dye photodegradation efficiency in salt waters is explained by fouling effects of inorganic ions on titania photoactivity. Several mechanisms for fouling effects of inorganic ions on titania photoactivity have been proposed [218]. These include UV screening, competitive adsorption to surface active sites, competition for photons, surface

deposition of precipitates and elemental metals, radical and hole scavenging and direct reaction with the photocatalyst.

Furthermore, according to k_{app} values for photodegradation in saline waters, it can be seen that the photocatalytic efficiency is higher in ASW at lower concentrations (20 and 30 mg·dm⁻³), while at higher concentrations the efficiency is slightly higher in NSW, for both photocatalysts. It could be assumed that the better efficiency in ASW than in NSW is because NSW contains, besides major cations and anions (**Table 3**), some other ions (carbonate and bicarbonate) and organic substances. It was reported that carbonate and bicarbonate ions act as electron scavengers and thus they are expected to be responsible for lowering the degradation rate [225]. However, when the photocatalysis takes place in air atmosphere, oxygen is more powerful scavenger of electrons formed in TiO₂ after illumination than carbonate and bicarbonate ions. In addition, the reaction rate constants of hydroxyl radicals with carbonate and bicarbonate ions are much smaller than the values given for the other ions [226]. Therefore, it is likely that organic substances present in NSW influence the activity of titania powders by adsorption and blocking active sites onto their surface. The differences in photocatalytic activity in ASW and NSW may be also the result of different pH values of the suspensions during the reaction. The pH values of the suspensions in NSW were higher than pH_{PZC} of the titania, while in the case of suspension in ASW, the pH values were approximately equal to the titania pH_{PZC}. Accordingly, adsorption of the dye anions should be less favorable at negatively charged titania surface in NSW than in ASW. These results show that, besides major ions, organic compounds naturally present in seawater have a large influence on photocatalytic activity of titania powders. Consequently, the artificial seawater that contains major seawater ions cannot be used as a model for prediction of photocatalysts activity in natural seawaters.

By comparing the photocatalysts P25 and P160/500, it can be observed that P160/500 had slightly better photocatalytic efficiency than P25 in all three types of water. The values of k_{app} in all three types of water for P160/500 are higher than for P25 (with experimental uncertainty for higher concentration of dye). It is well known that the efficiency of semiconductors is influenced by many factors, such as crystalline structure, particle size, specific surface area, adsorption capacity, and prevention of electron–hole pair recombination reactions. In comparison with P25, powder P160/500

has slightly higher specific surface area, higher pore volume and larger pores, which contributes to its better photocatalytic efficiency with respect to P25. On the other hand, P25 crystallites are slightly larger than of P160/500 and P25 contains 72.7 % anatase and 27.3 % of rutile, while P160/500 contains pure anatase. These features contribute to better photoactivity of P25. It was shown [227] that, in comparison to pure anatase, mixed-phase titania catalysts show greater photoeffectiveness in UV region due to the stabilization of charge separation by electron transfer from rutile to anatase, which slows recombination. Despite the fact that P160/500 contains pure anatase, its photocatalytic efficiency is slightly higher comparing to P25, probably due to higher specific surface area and larger pores. For the same quantity of adsorbed dye, surface coverage will be higher in the case of TiO_2 with lower specific surface area, which causes higher reduction of light intensity reaching the photocatalyst and consequently lower photocatalytic activity. In addition, different types of aggregation of the primary particles of P160/500 and P25 (**Fig. 15**) caused different pore volumes and pore sizes of the powders. Pore size is very important parameter for photocatalysis, because large dye molecules cannot enter small pores and, in that way, surface of such pores is inaccessible for the reaction.

6.1.2. The influence of initial dye concentration on the initial photodegradation rate

The effect of initial dye concentration, after 30 minutes in dark, C_{dark} , on its initial photodegradation rate r_0 with P25 and P160/500 in DIW, NSW and ASW is demonstrated in **Fig. 18**. Values of r_0 (in $\text{mg}\cdot\text{dm}^{-3}\cdot\text{min}^{-1}$) were obtained according to the results presented in **Figs. 16** and **17**, as the dye concentration decay at 5 minutes of photoreaction. It can be observed from **Fig. 18** that the initial degradation rate increased with increasing the initial dye concentration and then remained almost constant. According to the L-H model [228,229] (Eq. 16, $r = r_0$ and $C = C_{\text{dark}}$), such dependence of r_0 on C_{dark} indicates that the oxidation rate is first-order at lower concentrations and becomes zero-order at higher concentrations, where the reaction rate becomes independent of the dye concentration (meaning a saturation-type Langmuir kinetics). Such Langmuir-type relationship between the initial degradation rate and concentration indicates that adsorption plays a role in the photocatalytic reaction.

From **Fig. 18** it is obvious that the highest values of initial reaction rate for both photocatalysts were observed for the DIW, than for the ASW, and the lowest for NSW, as it was found for the efficiency of the photocatalysts according to the overall reaction rate for the different dye concentrations.

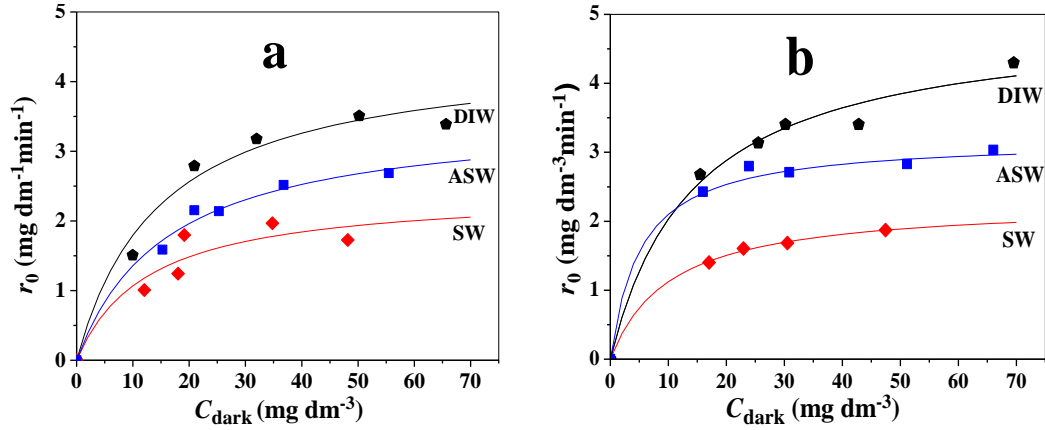


Fig. 18. Effect of initial RO16 dye concentration on its initial photodegradation rate with: a) P25 and b) P160/500 in DIW, NSW and ASW (UV irradiation at room temperature; RO16 concentration was in the range of 20 - 80 mg·dm⁻³; TiO₂ concentration was 1 g·dm⁻³).

The experimental data presented in Fig. 18 were fitted to the hyperbolic function, expressed by equation (37) [230]:

$$Y = \frac{abx}{1 + bx} \quad (37)$$

in which $Y = r_0$, $x = C_{\text{dark}}$, $b = K$ and $a = k$.

The parameters K and k were estimated by an optimization procedure using MATLAB and presented in **Table 7**.

Table 7. The parameters k and K obtained by fitting the experimental data of the photocatalytic dye degradation by P25 and P160/500 in DIW, SW and ASW (UV irradiation at room temperature; RO16 concentration was in the range of 20 - 80 $\text{mg}\cdot\text{dm}^{-3}$; TiO_2 concentration was $1 \text{ g}\cdot\text{dm}^{-3}$)

Type of titania	P25			P160		
Type of water	K ($\text{mg}\cdot\text{dm}^{-3}\cdot\text{min}^{-1}$)	K ($\text{dm}\cdot\text{mg}^{-1}$)	mes *	K ($\text{mg}\cdot\text{dm}^{-3}\cdot\text{min}^{-1}$)	K ($\text{dm}\cdot\text{mg}^{-1}$)	mes *
DIW	4.4364	0.0669	0.0487	4.9546	0.0695	0.0362
ASW	3.5383	0.0622	0.0119	3.1995	0.1964	0.0035
SW	2.4275	0.0786	0.0631	2.2746	0.0975	0.0005

* (mes) mean standard error

The results given in **Table 7** show that the values of the photodegradation rate constant k for both types of photocatalysts is higher in DIW than in saline waters, which indicates that inorganic ions have inhibiting effect on the photoactivity of both titania powders. In addition, the values of photodegradation rate constant for both photocatalysts are lower in natural seawater than in artificial seawater. The value of k for the photocatalytic decolorization in DIW by using P160 is slightly higher than with P25, probably because of higher surface area and larger pores. But the values of k for P160/500 in ASW and NSW are lower than for P25 in these waters, indicating that influence of inorganic ions is slightly more pronounced for P160/500 than for P25.

Presented results showed that the photocatalytic efficiency of powder P160/500 in deionized and saline waters under UV irradiation is comparable and even slightly higher than the efficiency of standard TiO_2 powder Degusa P25. Higher specific surface area, higher pore volume and larger pores of P160/500 with respect to P25 contributed to its better photocatalytic efficiency.

6.2. Characterization and photocatalytic activity of undoped TiO₂ synthesized by using different solvents

Considering very good photocatalytic efficiency of titania powder P160/500 under UV light, non-hydrolytic method coupled with solvothermal treatment was chosen as a method for the synthesis of doped titania powders. In trying to avoid previously used carbon tetrachloride regarded as highly toxic, the synthesis was performed also by using chloroform and cyclohexane, aprotic solvents of similar boiling points as CCl₄. The gels synthesized with CCl₄, CHCl₃ or C₆H₁₂ were annealed at 350, 400 or 500 °C in order to investigate the influence of both the temperature of gel annealing and the type of solvent used in the synthesis on the properties and photocatalytic activity of the titania powders.

6.2.1. X-ray diffraction analysis

The XRD patterns of all prepared undoped TiO₂ powders are shown in **Figs. 19-21**. All diffraction peaks can be assigned to the tetragonal anatase phase (JCPDS file no.01-078-2486(C)). As it was shown previously, the annealing temperatures were low to provide anatase → rutile transformation [7].

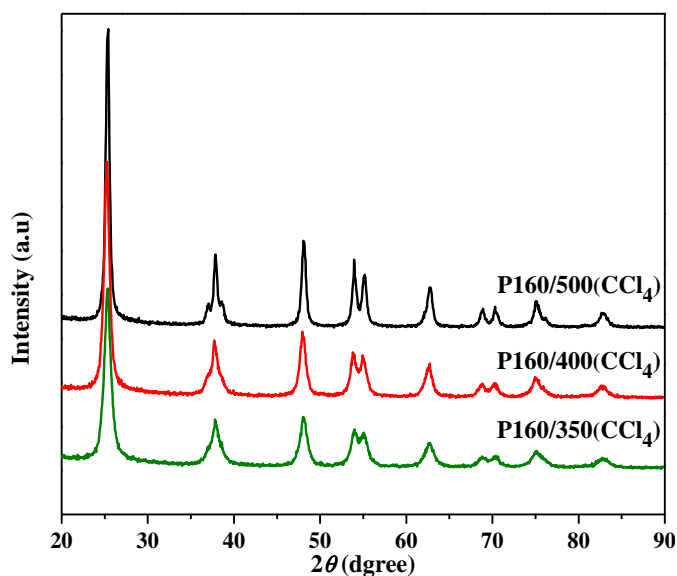


Fig. 19. XRD patterns of TiO₂ powders synthesized using CCl₄, annealed at different temperatures.

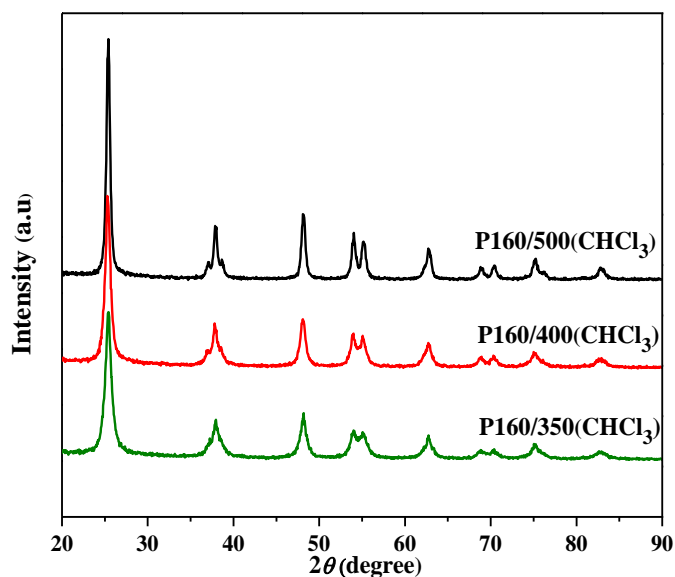


Fig. 20. XRD patterns of TiO₂ powders synthesized using CHCl₃, annealed at different temperatures.

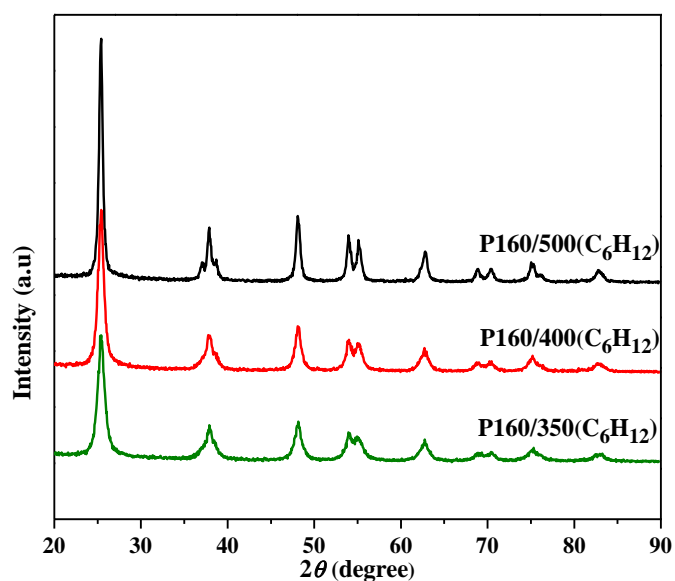


Fig. 21. XRD patterns of TiO₂ powders synthesized using C₆H₁₂, annealed at different temperatures.

Upon annealing at temperatures from 350 to 500 °C, a progressive enhancement of the crystallization degree of the anatase phase is identified, as reflected from a continuous sharpening and intensification of the diffraction peaks (**Fig. 19-21**). The influence of annealing temperature on the crystallization degree can be better seen from

the dependence of the crystallite size, calculated by using the Sherrer's equation (Eq. (33)), on the annealing temperature (**Table 8**). Obviously, the size of crystals increased almost linearly with the temperature of annealing.

The crystal sizes of the samples obtained with different solvents at the same annealing temperature were very similar, although the ones obtained with CHCl_3 were slightly larger than of samples obtained with CCl_4 and C_6H_{12} (**Table 8**). It was shown previously [7] that the conditions of solvothermal treatment, e.g. temperature and duration of treatment, influence the size of crystals of both the gel and the powder obtained by the gel annealing. Having in mind that the boiling point of CHCl_3 (61.2 °C) is lower than of C_6H_{12} (80.7 °C) and CCl_4 (76.8 °C), it can be concluded that higher pressure was achieved in the autoclave during solvothermal synthesis when CHCl_3 was used and the larger crystals were formed. Anyway, by using aprotic solvents of similar boiling points, titania powders of similar crystallite sizes were obtained.

Table 8. Crystallites sizes of TiO_2 powders

TiO_2 sample	Crystallite size (nm)
P160/350(CCl_4)	7.1
P160/400(CCl_4)	9.3
P160/500(CCl_4)	14.2
P160/350(CHCl_3)	7.7
P160/400(CHCl_3)	9.4
P160/500(CHCl_3)	14.6
P160/350(C_6H_{12})	7.0
P160/400(C_6H_{12})	8.6
P160/500(C_6H_{12})	14.1

6.2.2. Textural parameters

The textural parameters of the synthesized titania powders were determined via nitrogen adsorption/desorption isotherms presented in **Fig. 22a-24a**. The pore size distributions of the powders are presented in **Fig. 22b-24b** and the values of textural

parameters, the specific surface area (S_{BET}), total pore volume (V_t), the volume of mesopores (V_{meso}) and the mean diameter of mesopores (D_{mean}), are given in **Tables 9-11**.

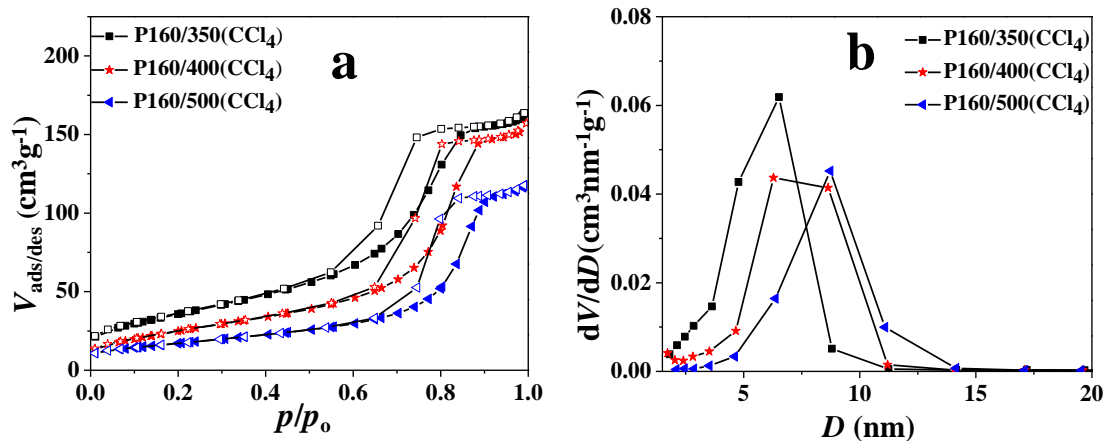


Fig. 22. a) N_2 adsorption-desorption isotherms, b) pore size distribution of TiO_2 powders synthesized using CCl_4 .

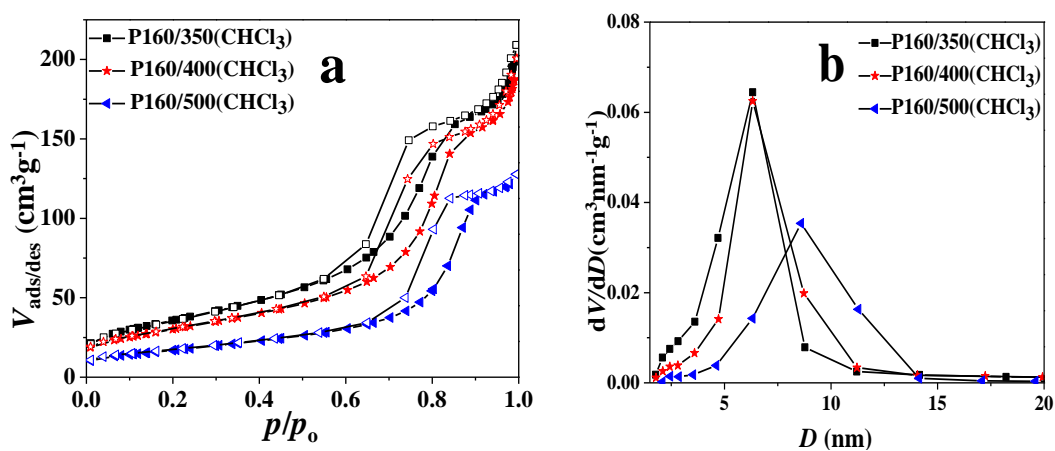


Fig. 23. a) N_2 adsorption-desorption isotherms, b) pore size distribution of TiO_2 powders synthesized using CHCl_3

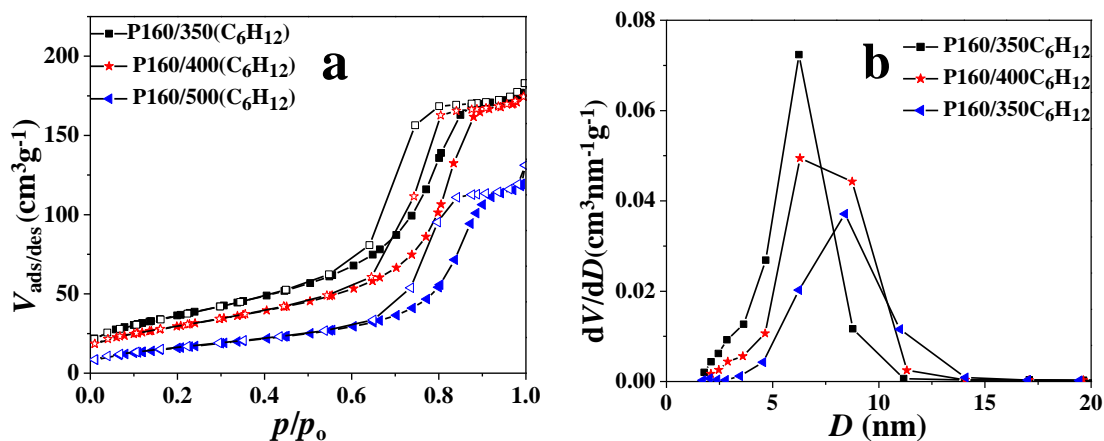


Fig. 24. a) N₂ adsorption-desorption isotherms, b) pore size distribution of TiO₂ powders synthesized using C₆H₁₂.

Adsorption-desorption isotherms for all powders belong to type IV isotherms according to the IUPAC classification that are characteristic of mesoporous material. The plots of the pore size distribution show also that all powders have obvious mesoporous structure, with pore sizes mainly in the range 3-12 nm.

Table 9. Textural characteristics TiO₂ powders synthesized using CCl₄

TiO ₂	P160/350(CCl ₄)	P160/400(CCl ₄)	P160/500(CCl ₄)
S_{BET} (m ² ·g ⁻¹)	130.9	94.5	61.9
V_t (cm ³ ·g ⁻¹)	0.249	0.236	0.178
V_{meso} (cm ³ ·g ⁻¹)	0.251	0.236	0.179
D_{mean} (nm)	5.6	6.9	8.3

Table 10. Textural characteristics TiO₂ powders synthesized using CHCl₃

TiO ₂	P160/350(CHCl ₃)	P160/400(CHCl ₃)	P160/500(CHCl ₃)
S_{BET} (m ² ·g ⁻¹)	129.6	109.8	62.0
V_t (cm ³ ·g ⁻¹)	0.311	0.294	0.190
V_{meso} (cm ³ ·g ⁻¹)	0.312	0.296	0.191
D_{mean} (nm)	6.8	7.7	8.6

Table 11. Textural characteristics TiO₂ powders synthesized using C₆H₁₂

TiO ₂ sample	P160/350(C ₆ H ₁₂)	P160/400(C ₆ H ₁₂)	P160/500(C ₆ H ₁₂)
S_{BET} (m ² ·g ⁻¹)	131.9	106.9	60.3
V_{t} (cm ³ ·g ⁻¹)	0.275	0.266	0.185
V_{meso} (cm ³ ·g ⁻¹)	0.276	0.267	0.185
D_{mean} (nm)	5.9	7.0	8.2

It is seen that the S_{BET} of the samples (**Tables 9-11**) decreases continuously with increasing annealing temperature. The variation of the sample pore volume with the annealing temperature followed the same trend of the surface area. In addition, with the annealing temperature increasing, the pore size distribution of samples exhibited a systematic shift toward larger mesopores, which can be associated with the collapse of the initial porous structure and growth of crystallites (**Table 8**). Sizes of pores and crystallites indicate that the pores were formed mainly between crystallites: the larger the crystallites, larger the pores.

The comparison of the textural properties of the samples obtained by annealing at the same temperature indicate the small influence of solvent type, although values of D_{mean} , V_{meso} and V_{t} are slightly higher for samples obtained by using CHCl₃ than for samples obtained by using CCl₄ and C₆H₁₂. Obviously, because of slightly larger crystallites of the CHCl₃-samples (**Table 8**), slightly larger pores were formed. In addition to boiling point, it is possible that differences in dipole moment have an influence on the powders properties, having in mind that CCl₄ and C₆H₁₂ are non-polar (dipole moment is 0), while CHCl₃ is polar (dipole moment is ~1). Generally, different aprotic solvents of similar boiling points will produce powders of similar crystallite sizes and textural properties.

6.2.3. SEM analysis

The SEM micrographs of the powders obtained by the gels annealing at 500 °C are shown in **Fig. 25**.

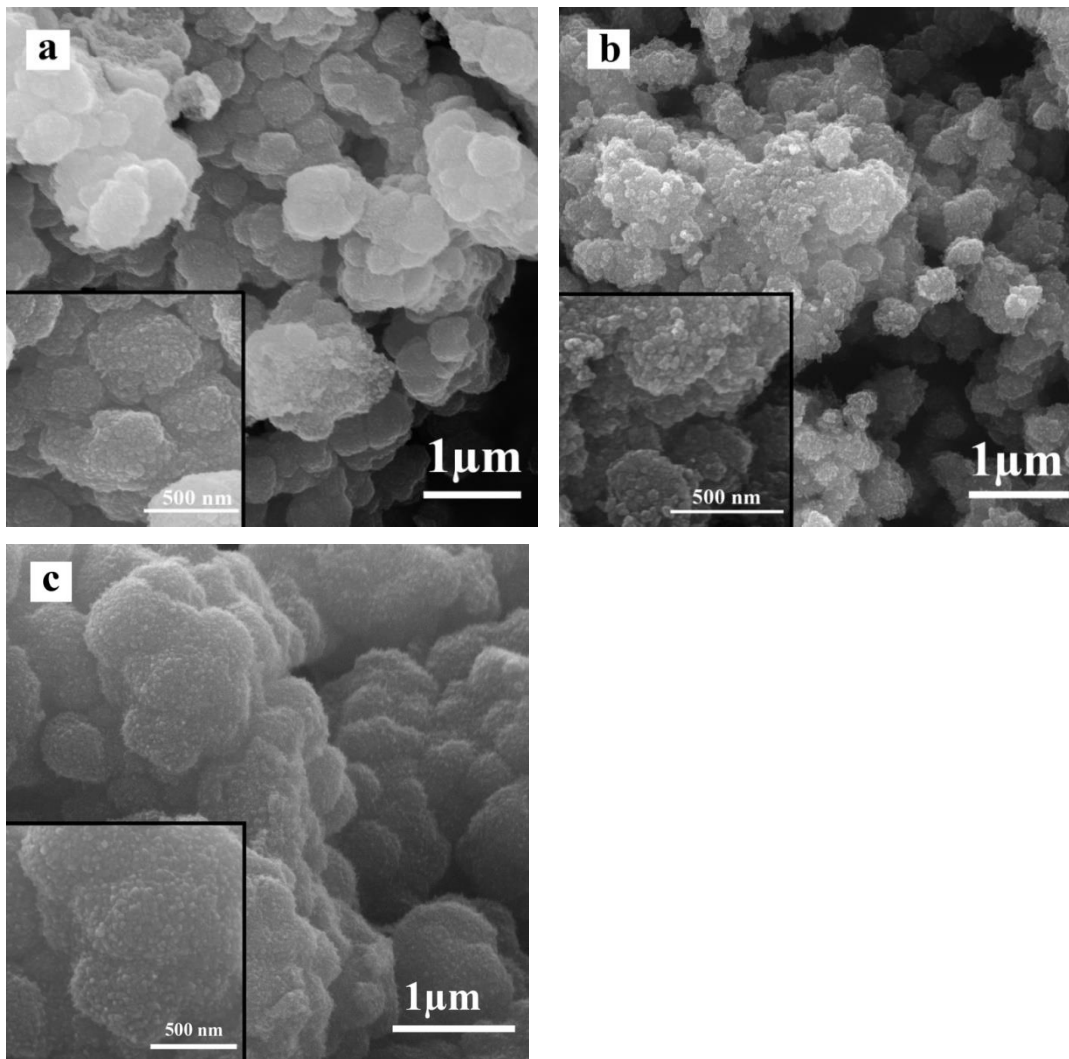


Fig. 25. SEM micrographs of TiO_2 powders: (a) P160/500(CCl_4), (b) P160/500(CHCl_3), (c) P160/500(C_6H_{12})

SEM analysis showed similar morphology of the powders: spherical particles, sizes of about 30 - 50 nm (inset in **Fig. 25**), are aggregated to form approximately spherical particles, which further aggregate and form larger irregular particles. Obviously, the type of solvent did not have significant influence on the morphology of the powders.

6.3. Photocatalytic activity under UV light

The photocatalytic activity of the powders synthesized by using CCl_4 , CHCl_3 and C_6H_{12} was tested by measuring the degradation of dye C.I. Reactive Orange 16 (RO16) under UV light irradiation. The results are presented in **Fig. 26** as a dependence of relative concentration, C/C_0 , on time, where C_0 is the starting concentration of RO16 and C is the RO16 concentration after 30 minutes stirring in dark or after time t of irradiation. The negative time (-30 min) is the time where the reactor was not irradiated and just adsorption of the dye took place. Preliminary experiments (not presented) showed that 30 min was enough time to attain adsorption/desorption equilibrium. In addition, results are presented in **Fig. 27** as the dependence of dye concentration relative to concentration after 30 min in dark (C_{dark}), where the corresponding linear plots of the kinetics of photocatalytic dye degradation are given in the insets. The derived k_{app} (Eq. (17)) values are presented in **Table 11**.

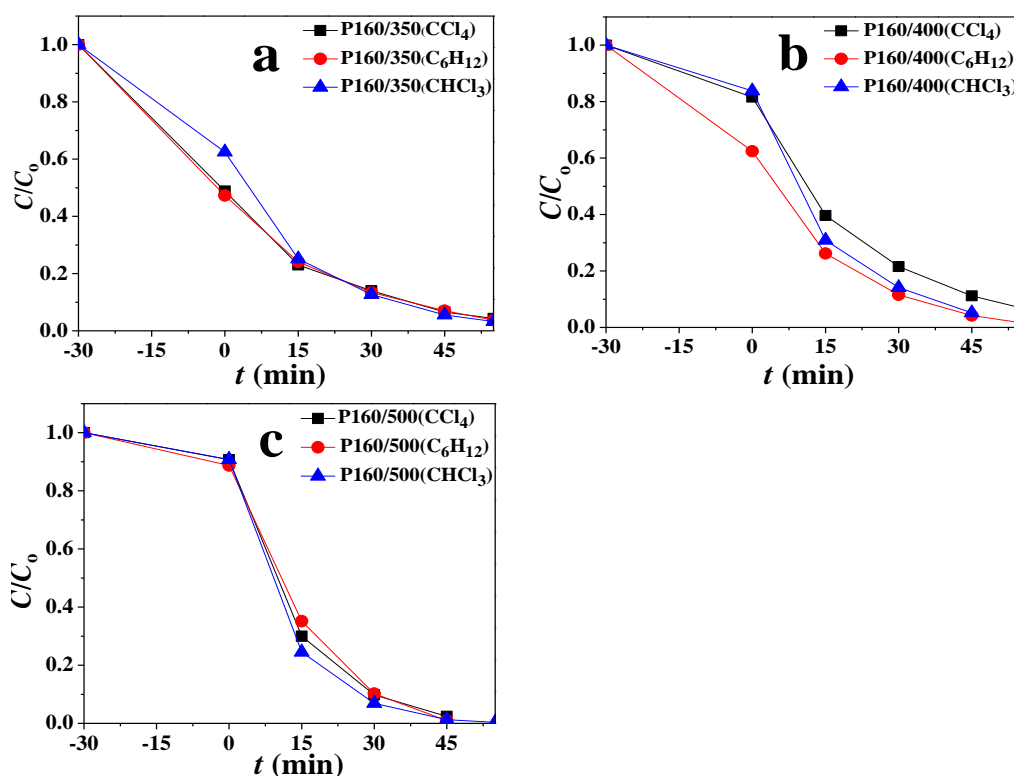


Fig. 26. Adsorption and photocatalytic degradation of RO16 dye under UV light irradiation in the presence of the powders synthesized by using CCl_4 , CHCl_3 and C_6H_{12} annealed at: a) 350 °C, b) 400 °C and c) 500 °C.

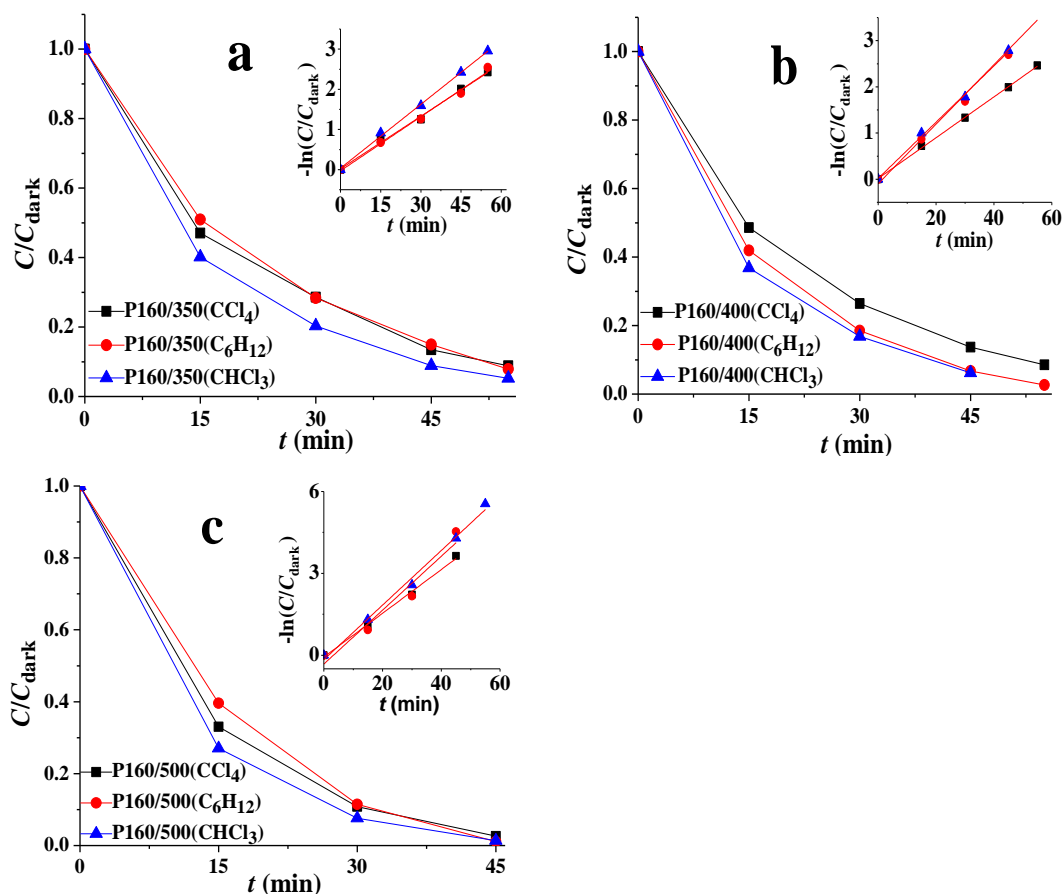


Fig. 27. Photocatalytic degradation of RO16 dye under UV light in the presence of the powders synthesized by using CCl_4 , CHCl_3 and C_6H_{12} annealed at: a) 350 °C, b) 400 °C and c) 500 °C.

Table 12. The k_{app} values of photocatalytic degradation of RO16 dye under UV light irradiation by the powders synthesized by using CCl_4 , CHCl_3 and C_6H_{12} annealed at: a) 350 °C, b) 400 °C and c) 500 °C.

TiO ₂ sample	k_{app} (min ⁻¹)	R ²
P160/350(CCl_4)	0.0436	0.9953
P160/350(CHCl_3)	0.0530	0.9979
P160/350(C_6H_{12})	0.0449	0.9919
P160/400(CCl_4)	0.0442	0.9991
P160/400(CHCl_3)	0.0609	0.9966
P160/400(C_6H_{12})	0.0645	0.9879
P160/500(CCl_4)	0.0802	0.9943
P160/500(CHCl_3)	0.1001	0.9905
P160/500(C_6H_{12})	0.0988	0.9285

The results (**Fig. 26**) showed that powders obtained by gels annealing at 350 °C had higher adsorption capacity for the dye (C/C_0 for P160/350 powders was about 0.5-0.6) than powders obtained at higher annealing temperatures (C/C_0 for P160/500 powders was about 0.9). On the other hand, powders P160/500 had the highest photocatalytic activity (**Fig. 27**). Obviously, high specific surface area of P160/350 powders (**Tables 9-11**) provided high adsorption capacity, but small crystallites caused lower photocatalytic efficiency of these powders in comparison to P160/500 powders with larger crystallites. It is known that the performance of a TiO₂ photocatalyst is influenced by many factors, such as crystalline structure, degree of crystallinity, particle size, specific surface area, adsorption capacity, and prevention of electron-hole pair recombination reactions. In addition, the carbonaceous residues of the catalyst also play an important role in the photocatalytic performance of TiO₂-based materials [231]. Generally, thermal treatment at elevated temperatures is beneficial for the photocatalytic efficiency because of a progressive elimination of the surface organic residue along with a further crystallization of the anatase phase. Smaller anatase crystals provided higher specific surface area, but also caused higher content of surface defect, where electron-hole pair recombination reactions take place, causing lower photocatalytic efficiency.

The powders obtained by using different solvents and annealed at the same temperature had approximately the same adsorption capacities and photocatalytic activities owing to similar structural and textural properties. It can be seen that powders obtained by using CHCl₃ had slightly better photocatalytic activities, probably due to larger crystals of the powders (**Table 8**).

Considering the highest photocatalytic efficiency of the powders obtained by gels annealing at 500 °C and similar textural, structural and photocatalytic properties under UV light of the powders obtained by using different solvents, powder P160/500(C₆H₁₂) was chosen for further investigations due to the lowest toxicity of C₆H₁₂.

6.4. Optimization of conditions of nitrogen-doping

An often-used method for nitrogen doping is annealing of TiO₂ in NH₃ atmosphere. Recently, it has been reported that a post-annealing in air can improve the visible-light activity of NH₃-treated TiO₂ in the photocatalytic degradation of organic compounds [162,163]. The effect of post-annealing is found to be positive by dramatically removing surface amino species, decreasing surface Ti³⁺ defects, facilitating the generation of O₂^{•-} radicals, improving the separation of photogenerated carriers on the NH₃-treated catalyst. In addition, O₂[•] radicals participate in the reaction of the dye degradation.

The conditions of post-annealing in air were optimized by varying temperature and duration of the treatment, as well as the type of air atmosphere (static or dynamic) in order to achieve the best photocatalytic efficiency under visible light. The efficiency of the post-annealing treatments was tested also by DRS analysis of the treated powders. In addition, annealing in a mixture of NH₃ and air was applied trying to avoid two-step process, i.e. annealing in ammonia followed by post-annealing in air.

6.4.1. Post-annealing in static air atmosphere

6.4.1.1. Visible-light activity of N-TiO₂ powders obtained at different post-annealing conditions

Fig. 28 shows the results of photocatalytic degradation of dye under visible light in the presence of undoped powder P160/500(C₆H₁₂) and N-TiO₂ powders obtained at different post-annealing conditions in static air atmosphere, as well as the powder without post-annealing treatment.

Obviously, the undoped powder P160/500(C₆H₁₂) was completely inactive in the dye degradation process under visible light. The powder obtained by gel annealing in NH₃ atmosphere, but without post-annealing (sample P160DN-NoPA), had high adsorption capacity, but very low photocatalytic activity, because almost the same dependence on time was observed in dark (sample P160DN-NoPA_{dark}), which

indicated that the decreasing of dye concentration was the results of prolonged adsorption, not of photocatalysis.

The photocatalytic efficiency of N-doped powders was higher when post-annealing was performed at 400 °C than at 450 °C (**Fig. 28**), probably because the removal of nitrogen from the TiO₂ structure was more intensive at higher temperatures. The efficiencies of the powders obtained by post-annealing at 350 °C and 400 °C were similar, which indicate that these temperatures were high enough to remove surface amino species, but no nitrogen from the TiO₂ structure. According to the results, 400 °C and 30 min were chosen as the optimal conditions for post-annealing in static conditions.

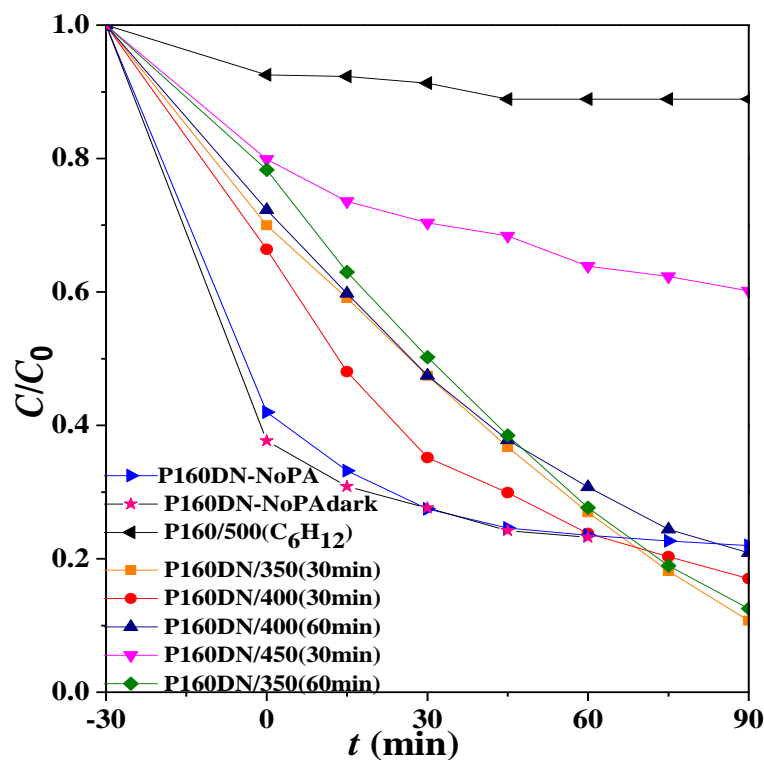


Fig. 28. Photocatalytic efficiency of undoped powder P160/500(C₆H₁₂), N-TiO₂ powders obtained at different post-annealing conditions and powder obtained without post-annealing (P160DN-NoPA); sample P160DN-NoPAdark is sample P160DN-NoPA without light (in dark)

6.4.1.2. DRS analysis of the N-TiO₂ powders obtained at different post-annealing conditions

The band gap energies (E_g) of the samples were determined from the diffuse-reflectance spectra (**Fig. 29a**) by plotting $[F(R_\infty)h\nu]^{1/2}$ against the photon energy, $h\nu$ (Tauc plot), as shown in **Fig. 29b**.

The results showed that doping with nitrogen lead to the band gap energy decreasing in comparison to undoped TiO₂ and that the E_g value depends on the post-annealing conditions. Obviously, post-annealing at 350 and 400 °C provided lower band-gap energies than the treatment at 450 °C, while the lowest E_g was achieved by post-annealing at 400 °C for 30 min. The results are in accordance with the photocatalytic efficiency determination, because the powder with the lowest band gap (P160DN/400(30min)) (**Fig.29b**) had the best efficiency in the process of photocatalytic degradation of dye (**Fig.28**). Therefore, the optimal conditions for post-annealing in static air atmosphere are temperature 400 °C and duration 30 minutes.

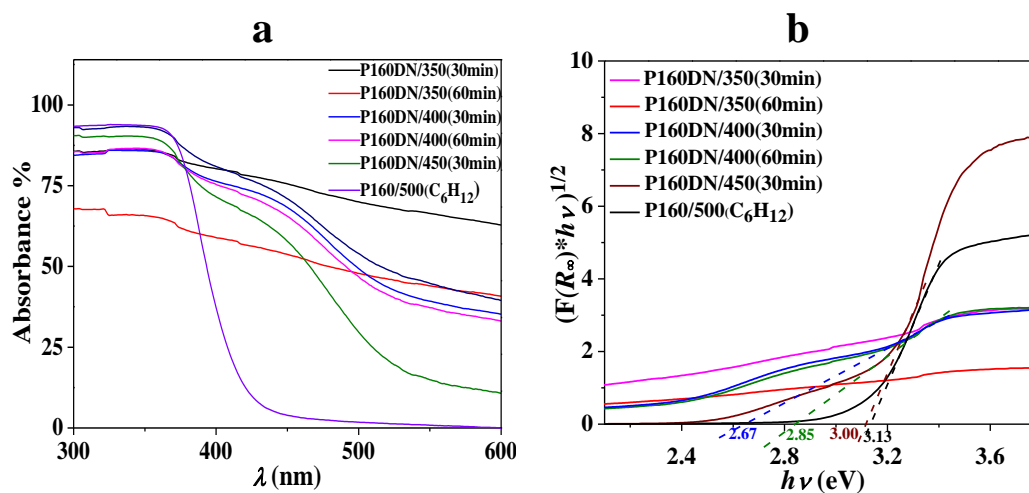


Fig. 29. Plot of UV–Vis diffuse reflectance spectra (a) and Tauc plots (b) for the N-TiO₂ powders obtained at different post-annealing conditions in static air atmosphere.

6.4.1.3. Morphology of the N-TiO₂ powders obtained at different post-annealing conditions

SEM micrographs of powders obtained by annealing in ammonia and post-annealed for 30 min at 350, 400 and 450 °C, as well as of powder obtained without post-

annealing, are shown in **Fig. 30**. All the powders have similar morphology as the powder P160/500(C_6H_{12}) (**Fig. 25c**), obtained by the annealing in air at 500 °C. Obviously, type of annealing atmosphere (air or ammonia) and post-annealing conditions do not have distinct influence on the powders morphology.

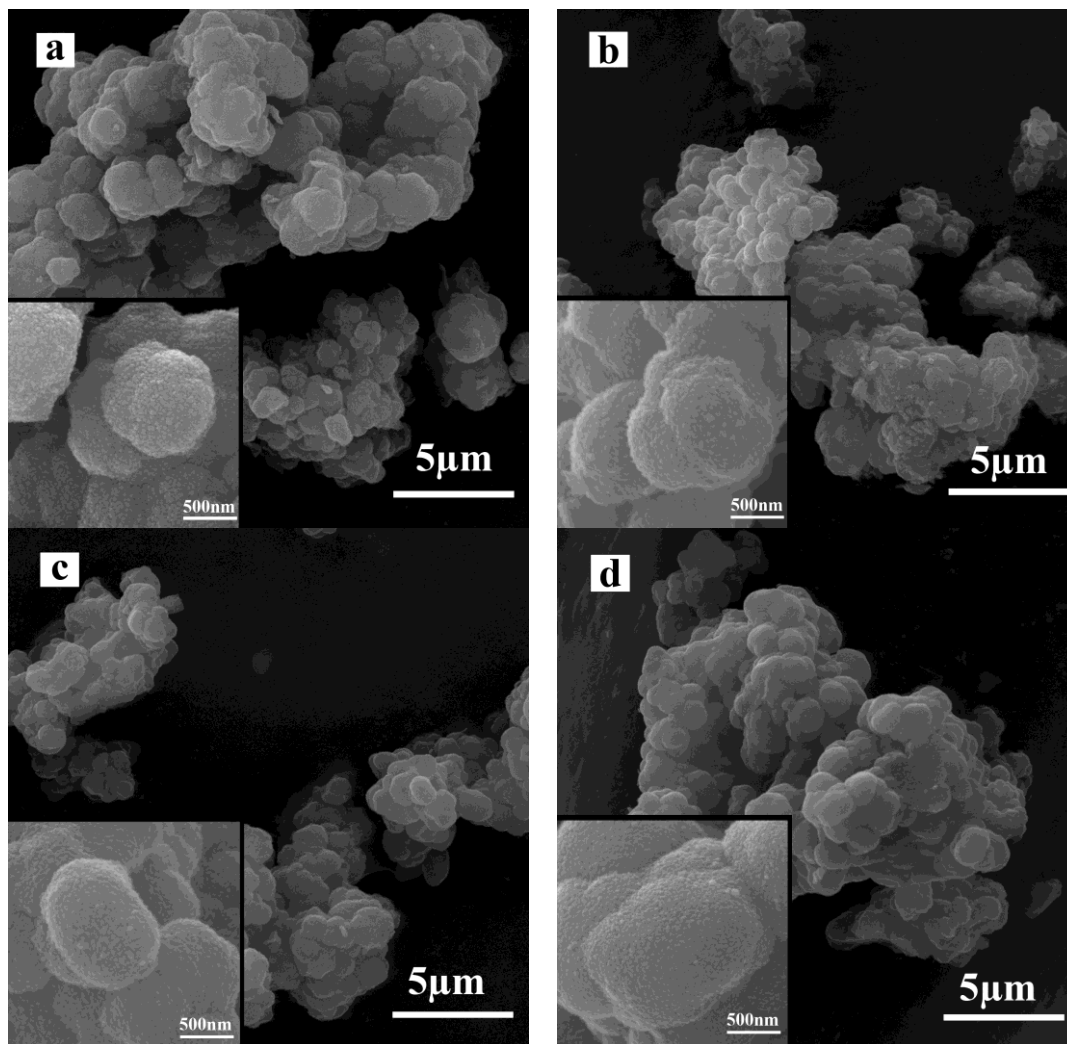


Fig. 30. SEM micrographs of the powders: a) obtained by G160(C_6H_{12}) calcination in ammonia at 500 °C for 3 h, without post-annealing b) P160DN/350(30min), c) P160DN/400(30min) and d) P160DN/450(30min)

6.4.2. Visible-light activity of N-TiO₂ powders obtained by post-annealing in dynamic air atmosphere

In **Fig. 31**, photocatalytic efficiency of the powders obtained at the optimal post-annealing temperature in static air atmosphere is compared with the efficiency of the powders obtained by post-annealing in air flow at the same temperature, but without cooling to room temperature after annealing in ammonia. Both the adsorption and photocatalytic degradation of dye were higher in the case of powder obtained by post-annealing in static air atmosphere. It can be assumed that air flow immediately after ammonia flowing caused lower specific surface area and intensive removal of nitrogen from the titania structure, which caused lower photocatalytic efficiency.

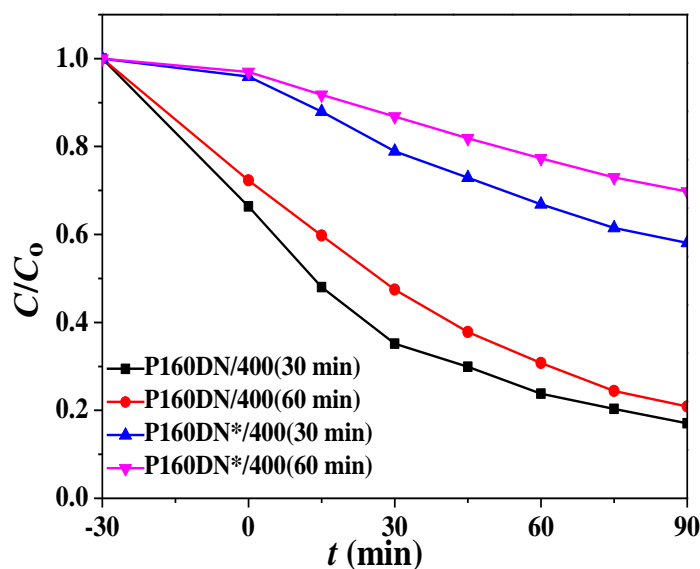


Fig. 31. The efficiency of N-TiO₂ powders obtained by post-annealing at 400 °C in static and dynamic air atmosphere.

6.4.3. Visible-light activity of N-TiO₂ powders annealed in air/NH₃ mixture followed by post-annealing in static air atmosphere

Gel annealing in a mixture of air and NH₃, at different ratios, was performed in order to achieve doping by nitrogen and the removal of ammonia species, at the same

time. However, so obtained powders were inactive under visible light, the same as the powder obtained by annealing in pure ammonia without post-annealing. Consequently, the powders obtained by annealing in air/NH₃ mixtures were also post-annealed in static air atmosphere at optimal conditions (400 °C and 30 min) and the activity of these powders are presented in **Fig. 32**, together with the activity of the powder P160DN/400(30min).

Samples obtained by annealing in air/NH₃ mixtures with the ratio 1:3 and 1:5 (P160DNR₁ and P160DNR₂, respectively) had very low visible-light activity, regardless of the post-annealing. Obviously, very low quantity of nitrogen was incorporated in the titania structure during annealing due to the presence of air in the mixture. Activity of the sample P160DNR₃ was much higher owing to much lower content of air in the mixture (ratio air/NH₃ = 1:15), but still lower than of sample P160DN/400(30min), which was obtained by gel annealing in pure ammonia.

The presented results showed that the best N-doping and visible-light activity was achieved by gel annealing in pure ammonia flow and post-annealing, after cooling to the room temperature, at 400 °C for 30 min in static air atmosphere.

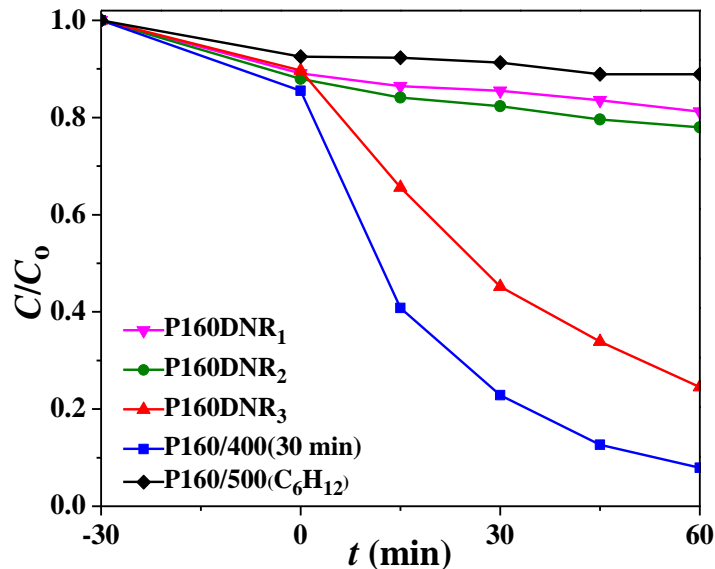


Fig. 32. The visible-light activity of N-TiO₂ powders obtained by annealing in air/NH₃ mixtures at 500 °C for 3 h and post-annealed at 400 °C and 30 min

6.5. Characterization of doped TiO₂

Doped titania powders were synthesized by annealing of:

- gel G200(DMSO) in air at 500 °C for 3h to obtain S-doped (P200DS) titania powder,
- gels G160(C₆H₁₂) and G200(DMSO) in ammonia flow at 500 °C for 3h, followed by post-annealing at 400 °C for 30 min in air to obtain N-doped (P160DN) and N,S-co-doped (P200DNS) titania powders, respectively,
- powder P160/500(C₆H₁₂) in ammonia flow at 500 °C for 3h, followed by post-annealing at 400 °C for 30 min in air to obtain powder N-doped (P160PDN) titania.

The experimental conditions for the preparation of doped titania powders are systematized in **Table 13**, together with the undoped powder P160/500(C₆H₁₂), which is labeled as P160 in the following text. The characteristics of the doped titania powders will be given in comparison to the properties of undoped powder P160.

Table 13. The experimental conditions for the TiO₂ samples preparation

TiO ₂ samples	P160	P160DN	P160PDN	P200DS	P200DNS
Solvent	C ₆ H ₁₂	C ₆ H ₁₂	C ₆ H ₁₂	DMSO	DMSO
Gelation temperature (°C)	160	160	160	200	200
Annealing at 500°C for 3 h in:	Air	NH ₃ flow	Air then NH ₃ flow	Air	NH ₃ flow
Post annealing in air at 400°C for 30 min:	No	Yes	Yes	No	Yes
Powder's color	White	Yellowish	Light yellowish	White	Beige

6.5.1. X-Ray diffraction analysis

The XRD patterns of the synthesized TiO₂ powders are shown in **Fig. 33**. All diffraction peaks can be assigned to the tetragonal anatase phase (JCPDS file no.01-078-2486 (C)).

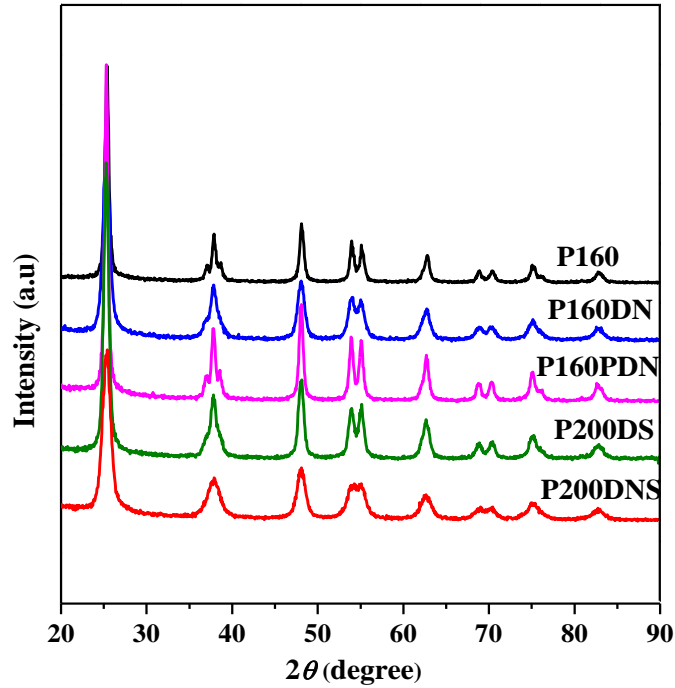


Fig. 33. XRD patterns of the TiO₂ powders.

The average crystallite sizes of the samples, calculated using the Scherer equation (Eq. 33), according to the broadening of (101) peak at $2\theta = 25.3^\circ$, are given in **Table 14**.

Table 14. Crystallite sizes of TiO₂ powders

TiO ₂ sample	Crystallite size (nm)
P160	14.1
P160DN	8.2
P200DS	10.5
P200DNS	5.1
P160PDN	15.3

The crystallite size of the samples obtained by annealing of gels G160(C₆H₁₂) and G200(DMSO) decreases in the following order: P160>P200DS>P160DN>P200DNS. Obviously, the samples obtained by the gels annealing in air (P160 and P200DS) have larger crystallites than the samples obtained by the gels annealing in ammonia (P160DN and P200DNS), which indicates a faster growth of crystallites in the presence of oxygen during the annealing. Additionally, the presence of sulfur in both cases (annealing in air and ammonia) causes the decrease of the crystallite size: the sample P200DS has lower size crystallites than the sample P160 and also the sample P200DNS lower than the sample P160DN. It can be supposed that the presence of doping agents inhibits the crystallite growth during the gels annealing [27,185,210,233], similarly as additives and impurities suppress grain growth during sintering. The crystallite size of the sample P160PDN, obtained starting from the powder P160/500(C₆H₁₂), i.e. P160, is slightly higher than of the parent sample, owing to the further growth of crystallite during P160 annealing in ammonia and post-annealing in air.

6.5.2. Textural parameters

The textural parameters of the synthesized titania powders were investigated via nitrogen adsorption/desorption isotherms shown in **Fig. 34a**. The pore size distributions of the powders are presented in **Fig.34b** and the values of textural parameters of the powders are given in **Table 15**.

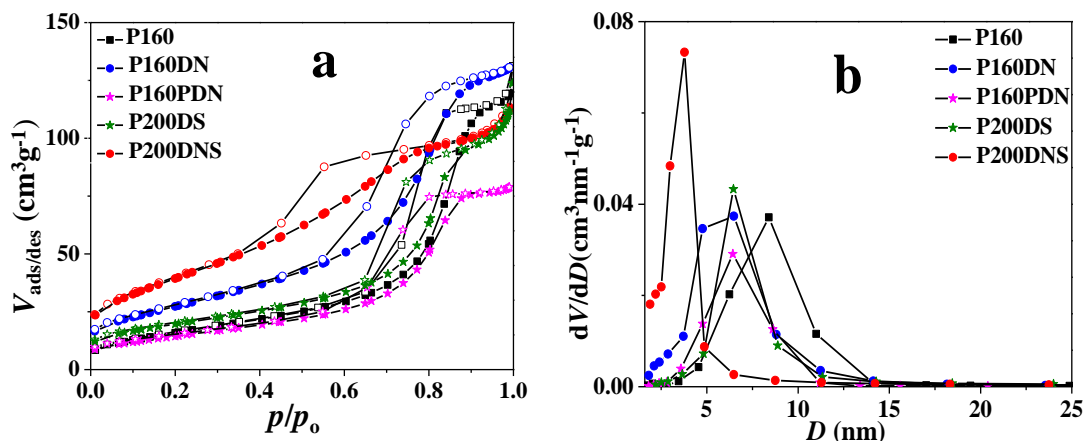


Fig. 34. a) N₂ adsorption-desorption isotherms, b) pore size distribution of TiO₂ powders.

Table 15. Textural properties of TiO₂ powders

TiO ₂ sample	P160	P160DN	P160PDN	P200DS	P200DNS
S_{BET} (m ² ·g ⁻¹)	60.3	100.1	53.2	69.7	144.8
V_{total} (cm ³ ·g ⁻¹)	0.185	0.200	0.120	0.174	0.169
V_{meso} (cm ³ ·g ⁻¹)	0.185	0.201	0.121	0.175	0.167
D_{mean} (nm)	8.2	5.9	6.4	7.7	3.9

All the isotherms exhibited the type IV behavior with H₂ hysteresis loop, indicating the presence of mesopores in the samples [234,235]. The comparison of the total pore volume, V_{total} , and the volume of mesopores, V_{meso} (**Table 15**) clearly shows that only the mesopores are present in the samples. Taking into account the crystallite and the pore sizes (**Tables 14 and 15**), it can be stated that the mesopores were formed among the crystallites. The approximately equal values of D_{max} and the mean diameter of the mesopores, D_{mean} (**Table 15**), indicate a narrow mesopore size distribution, which is also evident from the **Fig. 34b**.

The specific surface area, S_{BET} , of the samples is in agreement with the crystallite size: the samples with larger crystals have lower S_{BET} . The crystallite size decreased in the following order: P160PDN > P160 > P200DS > P160DN > P200DNS and S_{BET} increased in the same order. The samples obtained by gel calcinations in ammonia, P160DN and P200DNS, have the highest S_{BET} .

6.5.3. SEM analysis

The SEM images of the doped titania are presented in **Figs. 35** and **36**. The morphology of samples P160, P160DN and P160PDN are similar as of undoped powder P160 (P160/500(C₆H₁₂)) (**Figs. 25** and **35**) a cauliflower-like aggregates are formed from the relatively spherical particles of different sizes, which are composed of smaller spherical particles, whose sizes are ~ 50 nm (inset in **Figs. 25** and **35**). Regardless the similar morphology, the samples differ in the specific surface area, as it was shown, owing to different crystallite sizes (**Table 14** and **15**).

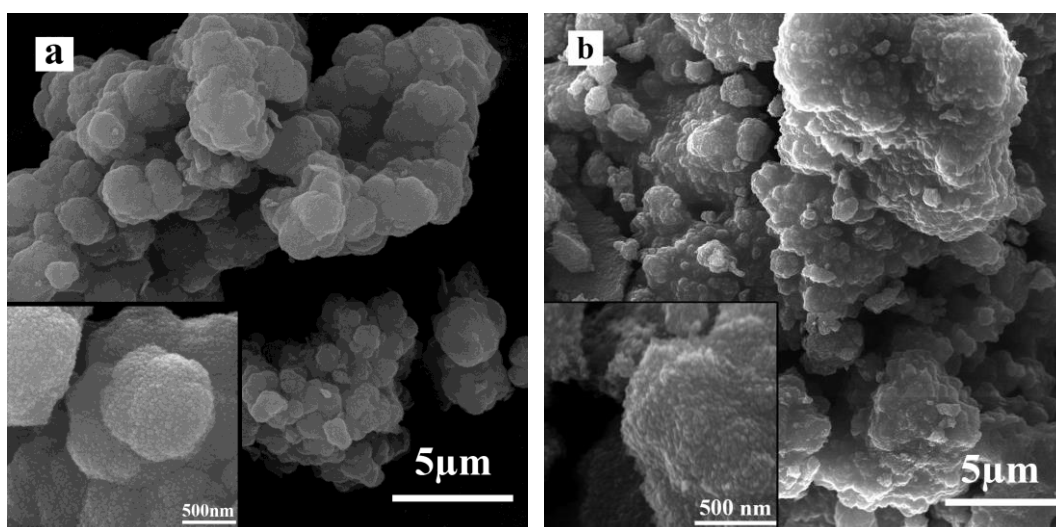


Fig. 35. SEM images of the samples: a) P160DN and b) P160PDN.

The morphology of the samples P200DS and P200DNS (**Fig. 36**) are similar, but different from the morphology of the samples P160, P160DN and P160PDN: the particles are smaller and less aggregated. Obviously, higher temperature of gelation in the case of synthesis with DMSO caused a formation of smaller, less aggregated particles [7]. Similarly as in the case of P160, P160DN and P160PDN, the samples P200DS and P200DNS have similar morphology, however the specific surface area of the sample P200DNS is higher than of the sample P200DS due to smaller crystallites (**Table 14** and **15**).

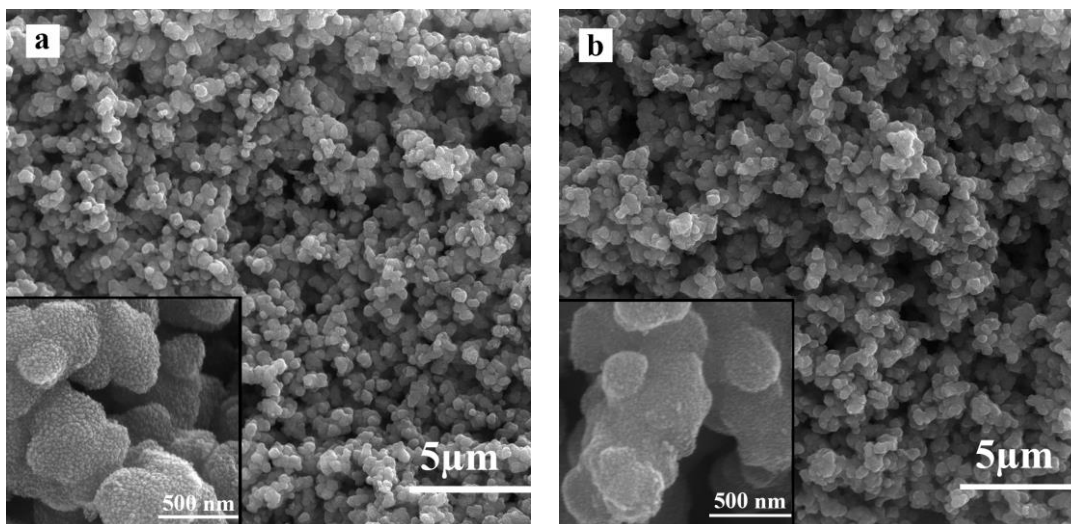


Fig. 36. SEM images of the samples: a) P200DS and b) P200DNS

6.5.4. TEM analysis

Figs. 37 a-d show the representative TEM images of the samples P160, P160DN, P160PDN and P200DNS. In all cases, the interconnection of the small primary particles, i.e. crystallites, results in the aggregates with significant framework of void space. This is consistent with the textural mesoporosity observed in N_2 adsorption isotherms. The HRTEM images (**Figs.37 e-h**) showed the interplanar spacing of about 0.35 nm (measured on the particles marked by arrow), corresponding to the (101) plane of anatase TiO_2 , which is in agreement with the results obtained from XRD. The average size of anatase crystallites, determined by a manual measurement of the size of about twenty crystallites per sample, decreases in the following order: P160PDN (11.0 nm) > P160 (8.3 nm) > P160DN (6.9 nm) > P200DNS (4.8 nm). The order is the same as obtained by XRD analysis, but the values obtained by TEM are smaller than obtained by XRD (**Table 14**). Since TEM images directly visualize irregularities such as variations of the crystallite shape or the presence of some considerably larger or smaller crystallites, generally TEM characterization provides better estimation of the crystallite size than calculation by the Scherrer formula.

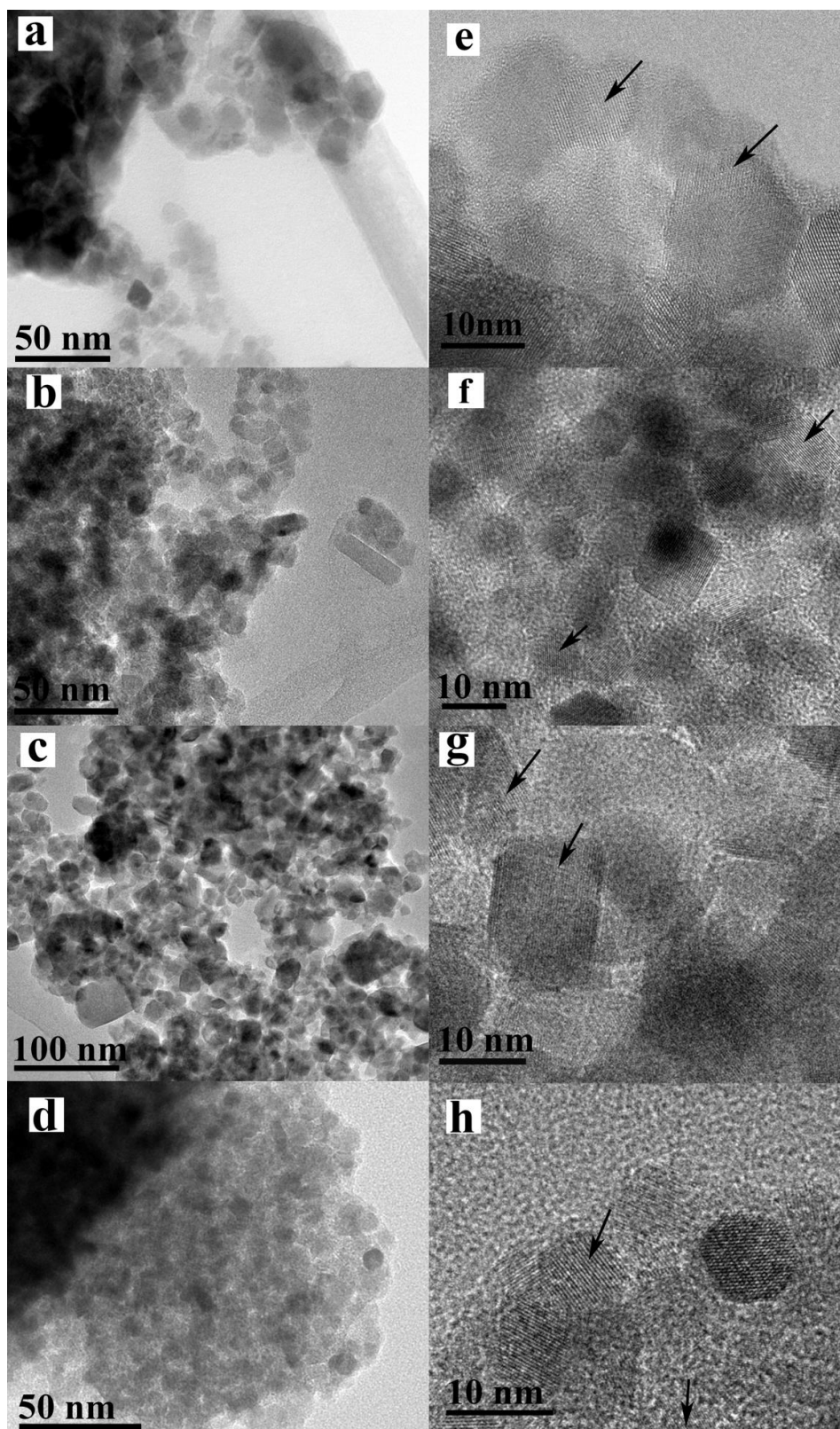


Fig. 37. TEM and HRTEM images of samples: P160 (a, e), P160DN (b, f), P160PDN (c, g) and P200DNS (d, h).

6.5.5. XPS analysis

The surface chemical composition and the chemical states of the titania samples were analyzed by means of XPS. As an example, XPS full survey spectra of the sample P200DNS is presented in **Fig. 38**. Besides Ti and O, C is present in all the samples, as a result of surface contamination and the use of organic precursors during the synthesis. The quantity of carbon in all samples was about 25 at.%.

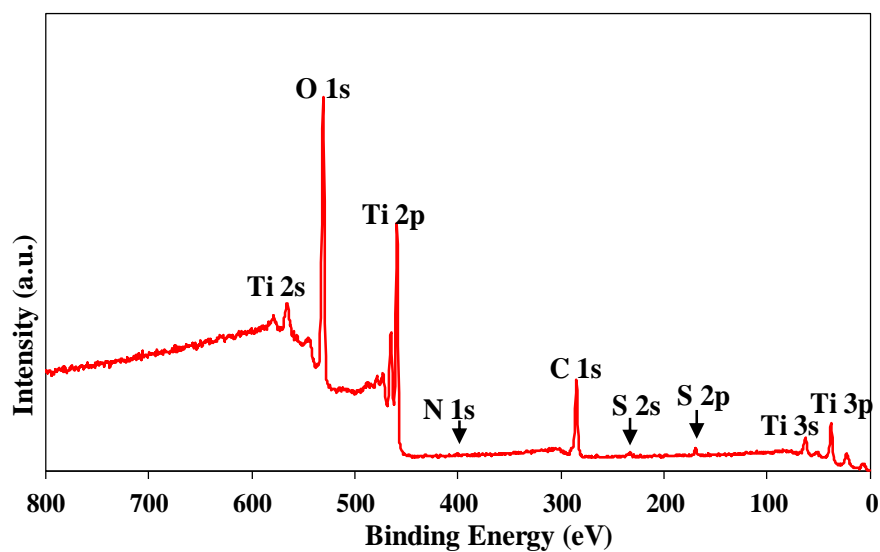


Fig. 38. XPS survey spectra from the sample P200DNS.

The high-resolution XPS spectra confirmed the presence of sulfur in the samples P200DS and P200DNS (**Fig. 39a**) and nitrogen in the samples P160DN and P200DNS (**Fig. 39b**).

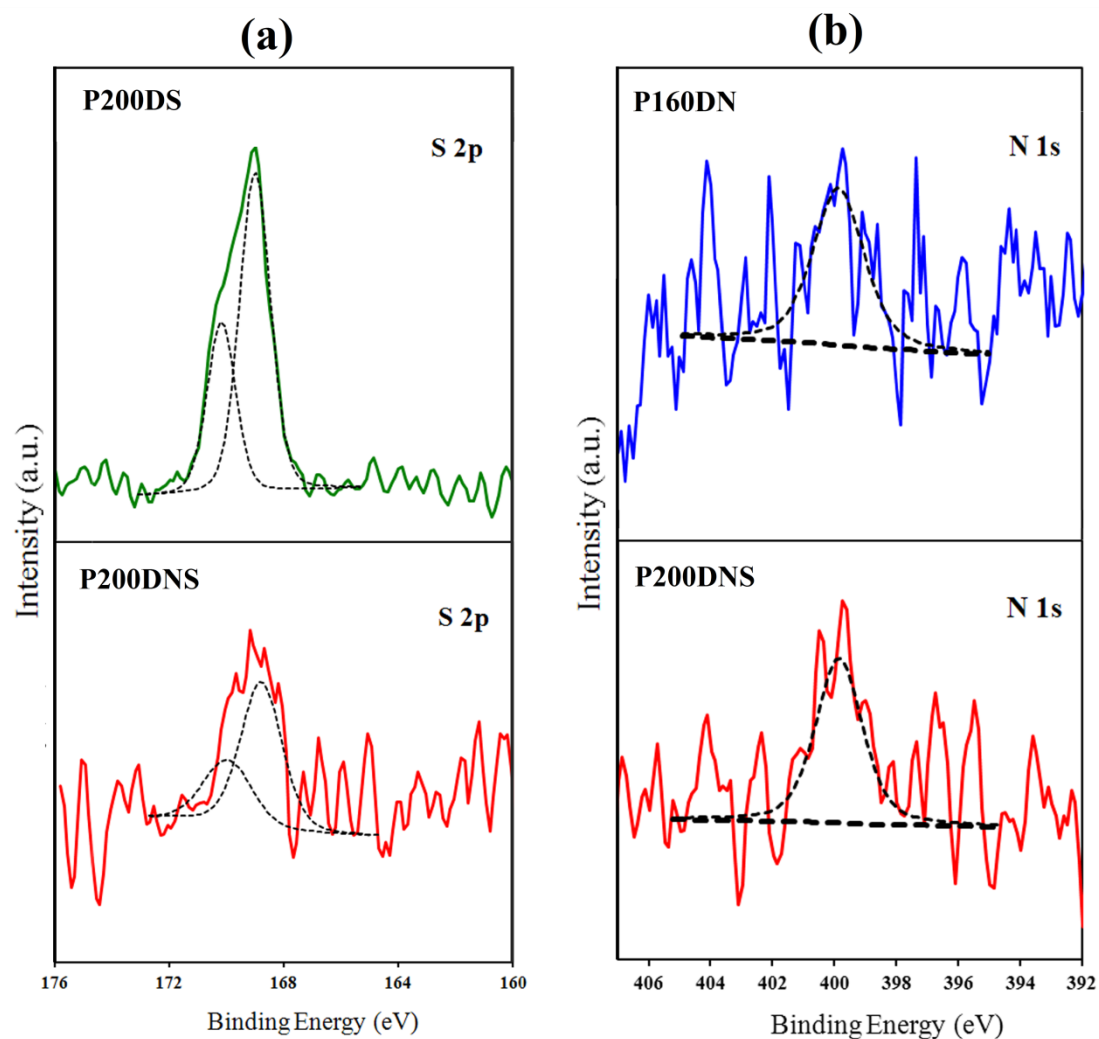


Fig. 39. XPS spectra of: a) S 2p from P200DS and P200DNS, b) N 1s from P160DN and P200DNS, where the curve fittings are shown as dashed lines.

The S 2p XPS spectra (**Fig. 39a**) are composed of doublet $2p_{3/2}$ and $2p_{1/2}$, separated by 1.18 eV [47]. The binding energy of the maximum of S $2p_{3/2}$ is at ~ 169.6 eV, which is related to both S(IV+) and S(VI+) oxidation state [20,23,236]. From this, it was concluded that sulphur from DMSO was incorporated in TiO_2 lattice, during the synthesis, as a cation in IV+ and/or VI+ valences, substituting Ti^{4+} [237]. There was no peak present at ~ 163 eV, related to S(2-) oxidation state, suggesting that the anion-type incorporation of S atoms by replacement of O atoms was not involved [238,239]. The content of sulfur in P200DS was ~ 2.0 at.%, which is significantly higher than in the sample P200DNS (~ 0.5 at.%). Both samples were obtained by annealing of gel G200(DMSO), but in different atmosphere. It can be assumed that the annealing in air

caused the oxidation of sulfur from the gel to higher oxidation states, S(IV+) and S(VI+), while this oxidation is suppressed when the annealing was performed in ammonia. Therefore, the substitution of Ti^{4+} by S(IV+) and S(VI+) is favourable in air atmosphere and the content of sulphur in the sample P200DS was higher than in the P200DNS.

The N 1s XPS spectra from the samples P160DN and P200DNS, obtained by gels annealing in ammonia, are shown in **Fig. 39b**. The signal of nitrogen was not visible in the spectrum of sample P160PDN, obtained by annealing titania powder in ammonia. That means that the nitrogen incorporation in titania was more efficient by the gel annealing than by the powder annealing in NH_3 . The maximums of N 1s spectra of the samples P160DN and P200DNS are located at ~ 400 eV, which indicates the interstitial integration of N^{3-} ion into TiO_2 lattice, being a usual type of nitrogen incorporation in TiO_2 lattice by annealing in ammonia [27,240]. The atomic content of nitrogen in P200DNS (~ 0.5 at.%) is slightly higher than in P160DN (~ 0.3 at.%).

The XPS Ti 2p spectra from all the samples are shown in **Fig. 40**. The Ti $2p_{3/2}$ and Ti $2p_{1/2}$ peaks for undoped TiO_2 (P160) are located at 458.5 and 464.2eV, respectively, which are the characteristic positions for pure TiO_2 [27,241]. It can be seen that doping by sulfur causes the peaks shifting to higher binding energies (samples P200DS and P200DNS), while the positions of the peaks for N-doped samples (P160DN and P160PDN) are the same as for P160. Moreover, the peak shifting to higher binding energies is more pronounced for the sample with higher quantity of sulfur (P200DS).

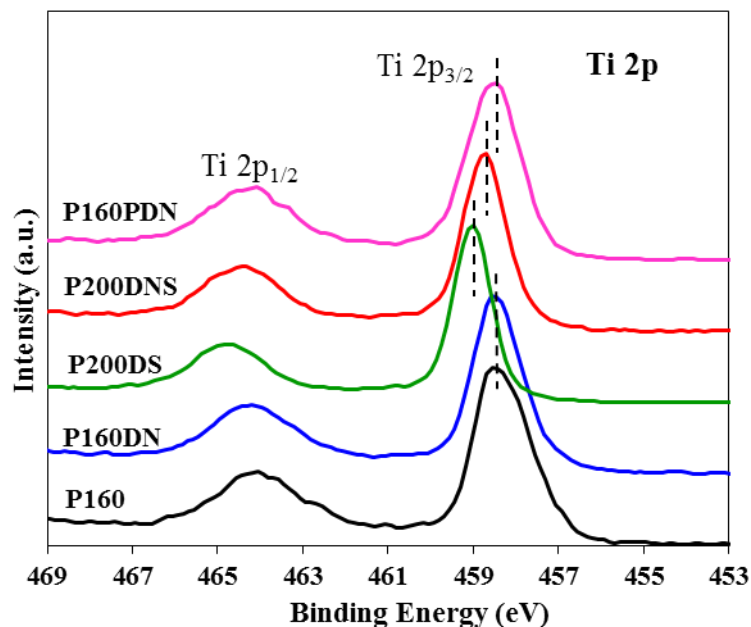


Fig. 40. XPS spectra of Ti 2p from all the TiO₂ powders.

It is known [194,242] that shifting of Ti 2p_{3/2} peak to lower binding energy is a result of the increase in electron density around the titanium cation and it can be related to the lowering of valence state level of Ti⁴⁺ to Ti³⁺ due to the formation of oxygen vacancies. In the oxygen atmosphere, reduction of Ti⁴⁺ to Ti³⁺ is suppressed, but it is stimulated in ammonia atmosphere [243]. In our experiments, the post-annealing in air was applied after annealing in ammonia, that caused a decrease of concentration of Ti³⁺ and oxygen vacancies formed during the annealing in ammonia. That is the reason why the Ti 2p_{3/2} peak is at the same position for the samples P160, P160DN and P160PDN: the concentration of Ti³⁺ in these samples is low and approximately the same.

On the other hand, higher Ti 2p_{3/2} binding energies for S-doped samples in comparison to P160 can be explained by the decrease in the electron density around the titanium cation due to the substitution of Ti⁴⁺ by S(IV+) and/or S(VI+) [194,242]. Both substitutions can cause decreasing of electron density around the titania cation: i) substitution by S(VI+) because of higher valence state of S(VI+) in comparison to Ti(IV+) and ii) substitution by S(IV+) because of higher electronegativity of sulfur (2.5) in comparison to titanium (1.5). Therefore, increasing of Ti 2p_{3/2} binding energies for S-doped samples in comparison to undoped TiO₂ clearly indicates the substitution of Ti⁴⁺ by sulfur, but it can not be said with certainty if S(IV+) or S(VI+) or both are present.

6.5.6. FTIR analysis

The FTIR spectra of all the samples are displayed in **Fig. 41**. The broad peak in the range 3000 - 3600 cm^{-1} and peak at 1627 cm^{-1} are present in all the spectra, corresponding to the stretching and bending vibration of O-H bonds, respectively, from either water molecules or surface hydroxyl groups [185,244,245]. The strong band in the range of 900-400 cm^{-1} encompasses several bands for Ti-O and Ti-O-Ti bonds in the TiO_2 lattice: stretching vibration of Ti-O bonds at higher wave numbers and stretching vibrations of Ti-O-Ti bonds at lower wave numbers [246,247]. In addition, small peaks at 2960, 2925, 2858, 1726, 1380 and 1275 cm^{-1} are observable in all the samples. The peaks at 2960, 2925 and 2858 cm^{-1} can be assigned to the C-H stretching vibration and the peak at 1380 cm^{-1} to the C-H bending vibration [20,244,248-250] of the residual organic species from the alkoxide precursor and the solvent. The peaks at 1726 and 1275 cm^{-1} may be attributed to the vibration of C=O and/or C-O groups, originated from organic species produced by oxidation of organic precursors during annealing [248].

The spectra of the samples doped with nitrogen are practically the same as the spectrum of sample P160. Only a very weak signal at 1090 cm^{-1} [12,251,252], which can be assign to nitrogen atoms embedded interstitially in TiO_2 , i.e. to N-O bonds, is visible in spectra of the samples P160DN and P160DNS. The presence of sulfur in the samples P200DS and P200DNS is proved by the band at 1048 cm^{-1} , which corresponds to the Ti-O-S bond, formed by Ti^{4+} substitution with S(IV+) or S(VI+) [26,236,253]. The band at 1117 cm^{-1} is also possible to attribute to sulfur-oxygen bonds, but this band is present in the spectra of all the samples. According to the literature [235], this band can originate from Ti-O-C bond, as a result of the presence of some organic impurities in all the samples.

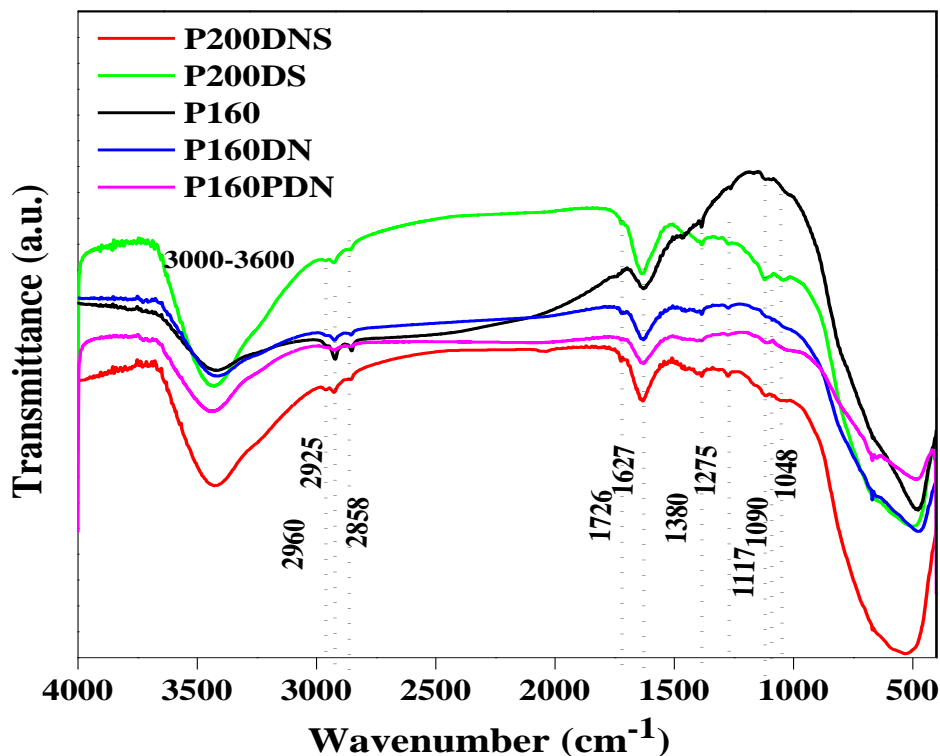


Fig. 41. FTIR spectra of the TiO₂ powders.

6.5.7. DRS analysis

The band gap energies (E_g) of the samples were determined from the diffuse-reflectance spectra (**Fig. 42a**) by plotting $[F(R_\infty)hv]^{1/2}$ against the photon energy, $h\nu$ (Tauc plot), as shown in **Fig. 42b**. The band gap energy of the sample P160 is 3.13 eV. The reason for the band gap narrowing in respect to pure anatase (3.20 eV) can be the presence of carbon [17,68,69], that is confirmed by FTIR spectroscopy. The band gap energy of S-doped sample (P200DS) is just slightly lower than of P160, despite the relatively high content of sulfur in the sample, as shown by XPS (~ 2.0 at. %). As already mentioned, the substitution of lattice titanium by sulfur can narrow the band-gap by the increases of the valence band width or by the formation of the localized midgap states above the valence-band edge [187,195,254]. Generally, the formation of midgap above the valence band causes larger band gap narrowing than the increasing of the valence band width [255]. As commented by Serpone [156], it is hard to believe that a low level of doping (<2 at. %) can rigidly shift up the valence band. Therefore, it can be supposed that S-doping in our case caused small band gap narrowing due to small

increase of the valence band width. [255] On the other hand, it is also possible that sulfur was dominantly concentrated at the surface, but not in the lattice of TiO_2 , which can explain the small band gap narrowing of the sample P200DS [254].

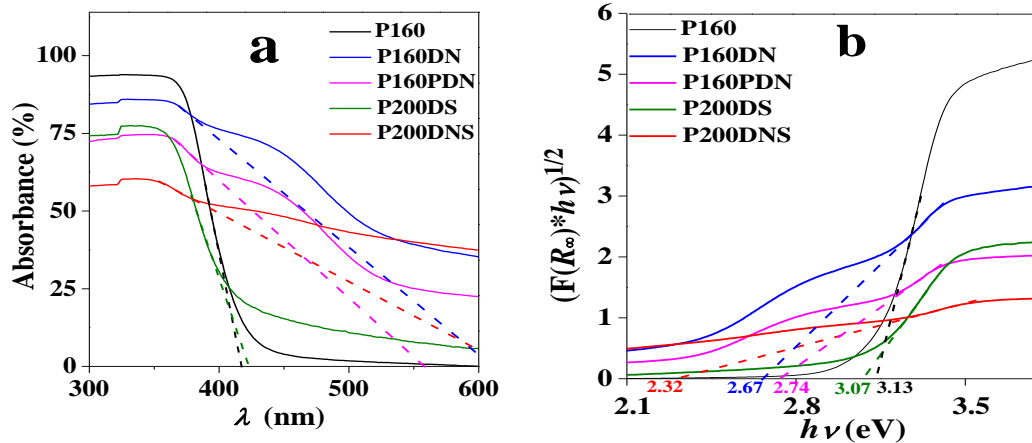


Fig. 42. Plot of UV–Vis diffuse reflectance spectra (a) and Tauc plots (b) for the TiO_2 powders.

The absorption of N-doped samples (P160DN, P160PDN and P200DNS) extends well into the visible light region and displays two thresholds. The threshold at lower λ values relates to the band gap, while the other at higher λ values might arise from surface states or impurity energy bands. According to Lindgren et al. [70], the second threshold absorption is not from a band-to-band transition, but due to excitation of electrons from local states in the band-gap to unoccupied states. The values of the first threshold, related to the band gap, for N-doped samples are significantly shifted to higher λ values: 559.70 nm (P160PDN) < 609.09 nm (P160DN) < 625.15 nm (P160DNS). The values of the energy band gap of N-doped samples decreased in the following order: 2.74 eV (P160PDN) > 2.67 eV (P160DN) > 2.32 eV (P160DNS) (**Fig. 42**). It is obvious that the annealing in ammonia of both titania gel and powder (samples P160DN and P160PDN, respectively) caused a significant narrowing of the band gap, but the narrowing is larger for the sample P160DN, as a result of higher nitrogen content in P160DN than in P160PDN, according to the XPS analysis. The XPS analysis did not show the presence of N in the sample P160PDN, but the narrowing of the band gap indicates the presence of nitrogen in P160PDN, whose content is obviously lower than detection limit of XPS analysis. The significant narrowing of the band gap caused

by a small content of nitrogen is a confirmation of the midgap formation [155,156,255], which is consistent with the XPS revealing that nitrogen is interstitially incorporated in the TiO₂ lattice.

The highest band gap narrowing was achieved by titania co-doping by N and S (sample P200DNS). Despite the fact that S-doping caused very small band gap narrowing (sample P200DS), co-doping with nitrogen significantly reduced the band gap (2.32 eV in comparison to 2.67 eV for sample P160DN), that causes the reduction of the energy required for photoactivation. Indeed, lower E_g of the sample P200DNS in comparison to P160DN can be a result of higher content of nitrogen, as determined by XPS. However, it should be emphasized that the presence of sulfur, i.e. Ti⁴⁺ substitution by S(VI+), promotes interstitial incorporation of nitrogen in TiO₂ lattice due to compensation of charge imbalance and causes higher nitrogen content and band gap narrowing.

6.6. Photocatalytic activity under visible light

The photocatalytic activity of the powders was examined under irradiation with > 400 nm light (simulated visible light) in the process of RO16 dye degradation. The results are presented in **Fig. 43**, as a dependence of the relative dye concentration, C/C_0 , on time. The negative time (- 30 min) indicates the time where the adsorption of dye took place, while the reactor was not irradiated. The investigation of dye adsorption on time, under identical conditions as during photocatalytic degradation, but without light irradiation (the results are not presented) has shown that 30 min is enough time to reach the adsorption/desorption equilibrium for all investigated titania powders.

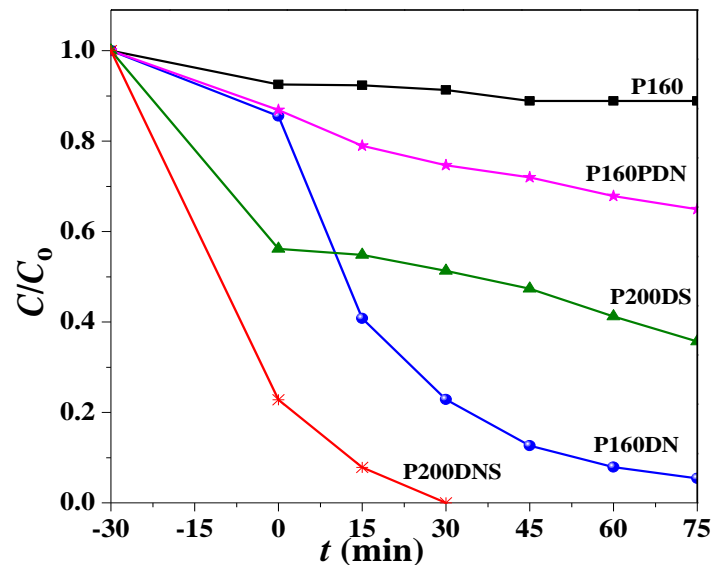


Fig. 43. Photocatalytic degradation of dye C.I. Reactive Orange 16 in the presence of TiO₂ powders.

As it already shown (**Fig. 28**), the undoped powder P160 was almost inactive in the dye degradation process under visible light (**Fig.40**), as well as powders obtained by gels G160(C₆H₁₂) and G200((CH₃)₂SO) annealing in ammonia without post-annealing in air (**Fig. 28**).

The doped samples exhibited different both photocatalytic activity under visible light and adsorption capacity for dye (**Fig.43**). The P200DNS had the highest adsorption capacity, which was expected, having in mind the highest specific surface area of this sample. However, despite the lower specific surface area, the sample P200DS had higher adsorption capacity than the sample P160DN. It can be explained by higher accessibility of the P200DS surface for the adsorption owing to smaller particles in comparison to the sample P160DN. Generally, the samples obtained by gelation at 160 °C had lower adsorption capacity than the samples obtained by gelation at 200 °C. The dye adsorption onto titania is important for its photocatalytic degradation, but the high adsorption capacity of the photocatalyst is not a prerequisite for a good photocatalytic activity, especially under visible light. For example, the adsorption capacity of the P200DS sample was much higher than of P160PND, but the photocatalytic activities were similar. On the other hand, the adsorption capacities of the samples P160DN and P160PDN were similar, but the photocatalytic efficiency of the P160DN sample was much higher than of P160PDN. It can be supposed that higher activity of P160DN

under visible light in comparison to P160PDN is a result of higher content of nitrogen, as confirmed by XPS analysis.

Besides crystalline structure, which is the same for all the samples, the crystallinity, photoabsorption, recombination rate of electron-hole pairs and the dopants concentration are the factors that influence the activity under visible light [251,256]. Photoabsorption is the most important factor, but strong light harvesting does not mean excellent photocatalytic property. Generally, high visible light absorption is a result of doping, but if the concentration is too high, the dopants can act as recombination centers and then negatively affect the photocatalytic activity of doped TiO₂ [251,256]

The best results of the dye degradation under visible light irradiation were achieved by using the sample P200DNS, due to both high adsorption capacity and photocatalytic activity. Owing to high adsorption capacity, high quantity of dye was adsorbed on the sample surface, and by favor of high photocatalytic efficiency of the sample, these molecules were oxidized fast, leaving the free space for the adsorption of new dye molecules from the solution. High photocatalytic efficiency is a result of titania doping with optimal concentration of N and S, providing in that way high visible light absorption and prevention of electron-hole recombination.

7. Conclusions

In this dissertation, undoped and N,S-doped titania powders were synthesized by non-hydrolytic sol–gel route, starting from titanium(IV) chloride and titanium(IV) isopropoxide dissolved in different solvents. Efficiency of thus synthesized undoped powder was investigated in different types of water in comparison to the efficiency of commercial photocatalyst P25, under UV light. In addition, undoped powders were synthesized by using different solvents and by annealing at different temperatures in order to achieve the best performances of the photocatalyst and to avoid usage of toxic solvent during synthesis. Solvent dimethyl sulfoxide (DMSO) was used in synthesis for sulphur doping, while annealing of gel or powder in ammonia at 500 °C for 3 h was applied for nitrogen doping. The post-annealing in air after annealing in ammonia was optimized to attain the best visible-light activity.

According to the results of the characterization of the titania powders and the photocatalytic degradation of dye C.I. Reactive Orange 16, the following conclusions were made:

- The efficiency of undoped titania, synthesized by using carbon-tetrachloride as a solvent, in deionized and saline waters under UV irradiation was slightly better than the efficiency of a standard TiO₂ powder Degusa P25; the efficiency of both photocatalysts in natural and artificial seawater was significantly lower than in deionized water.
- The dependence of the initial degradation rate on the initial dye concentration followed the Langmuir–Hinshelwood model; the photodegradation rate constant had similar values for the photocatalysts in all types of water due to similar properties of the photocatalysts.
- The textural properties, crystallite sizes, morphology and photocatalytic efficiency of undoped powders obtained by using different types of aprotic solvents of similar boiling points (carbon tetrachloride, chloroform, or cyclohexane), were approximately the same.
- Significant S-doping was achieved by using DMSO as a solvent, where S(IV+) and/or S(VI+) substituted Ti⁴⁺; surprisingly, this substitution caused a very small

band-gap narrowing and just slightly better visible-light activity in comparison to the undoped titania.

- Doping with nitrogen provided a much better photocatalytic activity than the S-doping, where annealing of the gel in ammonia flow was much more efficient way for nitrogen incorporation in TiO₂ structure than the annealing of crystalline titania powder.
- The XPS analysis revealed that nitrogen was incorporated interstitially in the titania structure as N³⁻ anion.
- Post-annealing in air of the samples obtained by annealing in ammonia or ammonia/air mixture was necessary in order to achieve a good visible-light activity; 400 °C and 30 min were determined as the optimal conditions for post-annealing in static air atmosphere.
- The highest photocatalytic activity under visible light was achieved with N,S-co-doped titania, as a result of high specific surface area, appropriate mesoporosity and efficient N,S-co-doping.

In summary, non-hydrolytic sol–gel method coupled with solvothermal treatment and annealing in air or ammonia was proved to be a convenient and powerful way for the synthesis of N,S-doped and co-doped visible-light active mesoporous, nanocrystalline anatase TiO₂ photocatalysts.

8. References

- [1] M. Pera-Titus, V. Garcia-Molina, M.A. Banos, J. Gimenez, S. Esplugas, Degradation of chlorophenols by means of advanced oxidation processes: a general review, *Appl. Catal. B* 47 (2004) 219–256.
- [2] F. Wang, D.W. Smith, M.G. El-Din, Application of advanced oxidation methods for landfill leachate treatment – A review, *J. Environ. Eng. Sci.* 2 (2003) 413–427.
- [3] J.M. Britto, M.D. Rangel, Advanced oxidation process of phenolic compounds in industrial waste water, *Quim. Nova* 31 (2008) 114–122.
- [4] S. Esplugas, D.M. Bila, L.G.T. Krause, M. Dezotti, Ozonation and advanced oxidation technologies to remove endocrine disrupting chemicals (EDCs) and pharmaceuticals and personal care products (PPCPs) in water effluents, *J. Hazard. Mater.* 149 (2007) 631–642.
- [5] A.L. Linsebigler, G. Lu, J.T. Yates, Photocatalysis on TiO₂ surfaces: principles, mechanisms, and selected results, *Chem. Rev.* 95 (1995) 735–758.
- [6] K. Xu, Y. Guo, Q. Sun, S. Dong, Z. Li, A new method for preparing TiO₂ catalyst honeycombs without sintering, *Res. Chem. Intermediate* 39 (2013) 1417–1428.
- [7] R. Petrović, N. Tanasković, V. Djokić, Ž. Radovanović, I. Janković-Častvan, I. Stamenković, Dj. Janačković, Influence of the gelation and calcination temperatures on physical parameters and photocatalytic activity of mesoporous titania powders synthesized by the nonhydrolytic sol–gel process, *Powder Technol.* 219 (2012) 239–243.
- [8] J.E. Mathis, J.J. Lieffers, C. Mitra, F.A. Reboredo, Z. Bi, C.A. Bridges, M.K. Kidder, M.P. Paranthaman, Increased photocatalytic activity of TiO₂ mesoporous micro spheres from codoping with transition metals and nitrogen, *Ceram. Int.* 42 (2016) 3556–3562.
- [9] T.H. Sia, S. Dai, B. Jin, M. Biggs, M.N. Chong, Hybridising nitrogen doped titania with kaolinite: a feasible catalyst for a semi-continuous photo-degradation reactor system, *Chem. Eng. J.* 279 (2015) 939–947.

- [10] D. Ljubas, Solar photocatalysis-a possible step in drinking water treatment, *Energy* 30 (2005) 1699–1710.
- [11] O. Sacco, V. Vaiano, C. Han, D. Sannino, D.D. Dionysiou, Photocatalytic removal of atrazine using N-doped TiO₂ supported on phosphors, *Appl. Catal. B Environ.* 164 (2015) 462–474.
- [12] M.A. Mohamed, W.N.W. Salleh, J. Jaafar, A.F. Ismail, N.A.M. Nor, Photo-degradation of phenol by N-doped TiO₂ anatase/rutile nanorods assembled microsphere under UV and visible light irradiation, *Mater. Chem. Phys.* 162 (2015) 113–123.
- [13] D. Ma, Y. Xin, M. Gao, J. Wu, Fabrication and photocatalytic properties of cationic and anionic S-doped TiO₂ nanofibers by electro spinning, *Appl. Catal. B Environ.* 147 (2014) 49–57.
- [14] N.O. Gopal, H.H. Lo, T.F. Ke, C.H. Lee, C.C. Chou, J.D. Wu, S.C. Sheu, S.C. Ke, Visible light active phosphorus-doped TiO₂ nanoparticles: an EPR evidence for the enhanced charge separation, *J. Phys. Chem. C* 116 (2012) 16191–16197.
- [15] Y. Wang, X. Xue, H. Yang, Preparation and characterization of carbon or/and boron-doped titania nano-materials with antibacterial activity, *Ceram. Int.* 40 (2014) 12533–12537.
- [16] M. Pelaez, A.A. de la Cruz, E. Stathatos, P. Falaras, D.D. Dionysiou, Visible light-activated N-F-codoped TiO₂ nanoparticles for the photocatalytic degradation of microcystin-LR in water, *Catal. Today* 144 (2009) 19–25.
- [17] L. Zeng, W. Song, M. Li, X. Jie, D. Zeng, C. Xie, Comparative study on the visible light driven photocatalytic activity between substitutional nitrogen doped and interstitial nitrogen doped TiO₂, *Appl. Catal. A Gen.* 488 (2014) 239–247.
- [18] T. Ohno, M. Akiyoshi, T. Umebayashi, K. Asai, T. Mitsui, M. Matsumura, Preparation of S-doped TiO₂ photocatalysts and their photocatalytic activities under visible light, *Appl. Catal. A Gen.* 265 (2004) 115–121.
- [19] T. Umebayashi, T. Yamaki, S. Yamamoto, A. Miyashita, S. Tanaka, T. Sumita, K. Asai, Sulfur- doping of rutile-titanium dioxide by ion implantation: photo-current spectroscopy and first-principles band calculation studies, *J. Appl. Phys.* 93 (2003) 5156–5160.

- [20] X.F. Lei, X.X. Xue, H. Yang, C. Chen, X. Lia, M.C. Niu, X.Y. Gao, Y.T. Yang, Effect of calcination temperature on the structure and visible-light photocatalytic activities of (N, S and C) co-doped TiO₂ nano-materials, *Appl. Surf. Sci.* 332 (2015) 172–180.
- [21] N. Todorova, T. Vaimakis, D. Petrakis, S. Hishita, N. Boukos, T.G. kopoulou, M. Giannouri, S. Antiohos, D. Papageorgiou, E.Chaniotakis, C. Trapalis, N and N,S-doped TiO₂ photocatalysts and their activity in NO_x oxidation, *Catal. Today* 209 (2013) 41–46.
- [22] R. Rahimi, S.S. Moghaddam, M. Rabbani, Comparison of photocatalysis degradation of 4-nitrophenol using N, S co-doped TiO₂ nanoparticles synthesized by two different routes, *J. Sol Gel Sci. Technol.* 64 (2012) 17–26.
- [23] E.M. Rockafellow, L.K. Stewart, W.S. Jenks, Is sulfur-doped TiO₂ an effective visible light photocatalyst for remediation? *Appl. Catal. B Environ.* 91 (2009) 554–562.
- [24] A.M. Asiri, M.S. Al-Amoudi, S.A. Bazaid, A.A. Adam, K.A. Alamry, S. Anandan, Enhanced visible light photodegradation of water pollutants over N-,S-doped titanium dioxide and n-titanium dioxide in the presence of inorganic anions, *J. Saudi Chem. Soc.* 18 (2014) 155–163.
- [25] X. Chen, X. Wang, Y. Hou, J. Huang, L. Wu, X. Fu, The effect of postnitridation annealing on the surface property and photocatalytic performance of N-doped TiO₂ under visible light irradiation, *J. Catal.* 255 (2008) 59–67.
- [26] Y. Chen, X. Cao, B. Lin, B. Gao, Origin of the visible-light photoactivity of NH₃- treated TiO₂: effect of nitrogen doping and oxygen vacancies, *Appl. Surf. Sci.* 264 (2013) 845–852.
- [27] Y. Wang, C. Feng, M. Zhang, J. Yang, Z. Zhang, Enhanced visible light photocatalytic activity of N-doped TiO₂ in relation to single-electron-trapped oxygen vacancy and doped-nitrogen, *Appl. Catal. B Environ.* 100 (2010) 84–90.
- [28] J. Senthilnathan, L. Philip, Photocatalytic degradation of lindane under UV and visible light using N-doped TiO₂, *Chem. Eng. J.* 161 (2010) 83–92.
- [29] S. Livraghi, M. Pelaez, J. Biedrzycki, I. Corazzari, E. Giamello, D.D. Dionysiou, Influence of the chemical synthesis on the physicochemical properties of N-TiO₂ nanoparticles, *Catal. Today* 209 (2013) 54–59.

- [30] C.J. Brinker, G.W. Scherer, *Sol-gel science: The physical and chemistry of sol-gel processing*, Academic Press Inc., USA, 1990.
- [31] C. Su, B.Y. Hong, C.M. Tseng, Sol-gel preparation and photocatalysis of titanium dioxide, *Catal. Today* 96 (2004) 119–126.
- [32] M. Crişan, N. Drăgan, D. Crişan, A. Ianculescu, I. Niţoi, P. Oancea, L. Todan, C. Stan, N. Stănică, The effects of Fe, Co and Ni dopants on TiO₂ structure of sol-gel nanopowders used as photocatalysts for environmental protection: a comparative study, *Ceram. Int.* 42 (2016) 3088–3095.
- [33] R. Bleta, P. Alphonse, L. Lorenzato, Nanoparticle route for the preparation in aqueous medium of mesoporous TiO₂ with controlled porosity and crystalline framework, *J. Phys. Chem. C* 114 (2010) 2039–2048.
- [34] H. Shibata, T. Ogura, T. Mukai, T. Ohkubo, H. Sakai, M. Abe, Direct synthesis of mesoporous titania particles having a crystalline wall, *J. Am. Chem. Soc.* 127 (2005) 16396–16397.
- [35] D.S. Kim, S.Y. Kwak, The hydrothermal synthesis of mesoporous TiO₂ with high crystallinity, thermal stability, large surface area, and enhanced photocatalytic activity, *Appl. Catal. A Gen.* 323 (2007) 110–118.
- [36] A.J. Albrbar, A. Bjelajac, V. Djokić, J. Miladinović, D. Janačković, R. Petrović, Photocatalytic efficiency of titania photocatalysts in saline waters, *J. Serbian Chem. Soc.* 79 (2014) 1127–1140.
- [37] Z. Zhang, J. Long, X. Xie, H. Zhuang, Y. Zhou, H. Lin, R. Yuan, W. Dai, Z. Ding, X. Wang, X. Fu, Controlling the synergistic effect of oxygen vacancies and N dopants to enhance photocatalytic activity of N-doped TiO₂ by H₂ reduction, *Appl. Catal. A Gen.* 425–426 (2012) 117–124.
- [38] C. Wang, R. Pagel, J.K. Dohrmann, D.W. Bahnemann, Antenna mechanism and deaggregation concept: novel mechanistic principles for photocatalysis, *C. R. Chimie* 9 (2006) 761–773.
- [39] R. Andreozzi, V. Caprio, A. Insola, R. Marotta, Advanced oxidation processes (AOP) for water purification and recovery, *Catal. Today* 53 (1999) 51–59.
- [40] M.I. Litter, Heterogeneous photocatalysis transition metal ions in photocatalytic systems, *Appl. Catal. B: Environmen.* 23 (1999) 89–114.

- [41] M.R. Hoffmann, S.T. Martin, W. Choi, D.W. Bahnemann, Environmental applications of semiconductor photocatalysis, *Chem. Rev.* 95 (1995) 69-96.
- [42] V. Diesen, Heterogeneous TiO₂ photocatalysis: Fundamental chemical aspects and effects of solid phase alterations, Doctoral thesis in Chemistry, KTH Vetenskap Och Konst (2013).
- [43] M. Pelaez, N.T. Nolan, S.C. Pillai, M.K. Seery, P. Falaras, A.G. Kontos, P.S.M. Dunlop, J.W.J. Hamilton, J.A. Byrne, K. O'Shea, M.H. Entezari, D.D. Dionysiou, A review on the visible light active titanium dioxide photocatalysts for environmental applications, *Appl. Catal. B: Environ.* 125 (2012) 331– 349.
- [44] A.L. Linsebigler, G. Lu, J.T. Yates, Photocatalysis on TiO₂ surfaces: principles, mechanisms, and selected results, *Chem. Rev.* 95 (1995) 735-758.
- [44] M. Grätzel, Photoelectrochemical cells, *Insight J.* 414 (2001) 338-344
- [45] G.S. Mital, T. Manoj, A review of TiO₂ nanoparticles, *Chinese Sci. Bull.* 56 (2011) 1639–1657.
- [46] O. Carp, C.L. Huisman, A. Reller, Photoinduced reactivity of titanium dioxide, *Prog. Solid State Chem.* 32 (2004) 33–177.
- [47] J-Y. Park, C. Lee, K-W. Jung, D. Jung, Structure related photocatalytic properties of TiO₂, *Bull. Korean Chem. Soc.* 30 (2009) 402-404.
- [48] S.G. Kumar, K.S.R. Koteswara Rao, Polymorphic phase transition among the titania crystal structures using a solution-based approach: from precursor chemistry to nucleation process, *Nanoscale*, 6 (2014) 11574-11632.
- [49] U. Diebold, The surface science of titanium dioxide, *Surf. Sci. Rep.* 48 (2003) 53-229.
- [50] X. Chen, S. S. Mao, Titanium dioxide nanomaterials: synthesis, properties, modifications, and applications, *Chem. Rev.* 107 (2007) 2891-2959.
- [51] N.T. Nolan, M.K. Seery, S.J. Hinder, L.F. Healy, S.C. Pillai, A systematic study of the effect of silver on the chelation of formic acid to a titanium precursor and the resulting effect on the anatase-to-rutile transformation of TiO₂, *J. Phys. Chem. C* 114 (2010) 13026-13034.
- [52] N.T. Nolan, M.K. Seery, S.C. Pillai, Spectroscopic investigation of the anatase-to-rutile transformation of sol–gel-synthesized TiO₂ photocatalysts, *J. Phys. Chem. C* 113 (2009)16151-16157.

- [53] S.R. Yoganarasimhan, C.N.R. Rao, Mechanism of crystal structure transformations. Part3. Factors affecting the anatase–rutile transformation, *Trans. Faraday Soc.* 58 (1962) 1579-1589.
- [54] C. Byun, J.W. Wang, L.T. Kim, K.S. Hong, B.W. Lee, Anatase-to-rutile transition of titania thin films prepared by MOCVD, *Mater. Res. Bull.* 32 (1997) 431-440.
- [55] K.J.D. MacKenzie, The effect of reaction atmosphere and electric fields on the anatase–rutile transformation, *Trans. J. Br. Ceram. Soc.* 74 (1975) 121-125.
- [56] Y. Li, T.J. White, S.H. Lim, Low-temperature synthesis and microstructural control of titania nanoparticles, *J. Solid State Chem.* 177 (2004) 1372-1381.
- [57] K.J.D. MacKenzie, The calcinations of titania: the effect of additive on the anatase–rutile transformation, *Trans. J. Br. Ceram. Soc.* 74 (1975) 29-34.
- [58] H. Liu, S. Cheng, M. Wu, J. Zhang, W. Li, C. Cao, Photoelectrocatalytic degradation of sulfosalicylic acid and its electrochemical impedance spectroscopy investigation, *J. Phys. Chem. A* 104 (2000) 7016-7020.
- [59] Y.U. Ahn, E.J. Kim, H.T. Kim, S.H. Hahn, Variation of structural and optical properties of sol–gel TiO₂ thin films with catalyst concentration and calcination temperature, *Mater. Lett.* 57 (2003) 4660-4666
- [60] J. Yang, Y.X. Huang, J.M. Ferreira, Inhibitory effect of alumina additive on the titania phase transformation of a sol–gel-derived powder, *J. Mater. Sci. Lett.* 16 (1997) 1933–1935.
- [61] J. Yang, J.M. Ferreira, On the titania phase transition by zirconia additive in a sol–gel-derived powder, *Mater. Res. Bull.* 33 (1998) 389–394.
- [62] H. Luo, C. Wang, Y. Yan, Synthesis of mesostructured titania with controlled crystalline framework, *Chem. Mater.* 15 (2003) 3841–3846.
- [63] C. Wang, Z. Deng, G. Zhang, S. Fan, Y. Li, Synthesis of nanocrystalline TiO₂ in alcohols, *Powder Technol.* 125 (2002) 39–44.
- [64] K.M. Reddy, C.V. Gopal Reddy, S.V. Manorana, Preparation, characterization, and spectral studies on nanocrystalline anatase TiO₂, *J. Solid State Chem.* 158 (2001) 180-186.

- [65] P.M Kumar, S. Badrinarayanan, M. Sastry, Nanocrystalline TiO₂ studied by optical, FTIR and X-ray photoelectron spectroscopy: correlation to presence of surface states, *Thin Solid Films* 358 (2000) 122-130.
- [66] H. Park, Y. Park, W. Kim, W. Choi, Surface modification of TiO₂ photocatalyst for environmental applications, *J. Photochem. Photobiol. C: Photochem. Rev.* 15 (2013) 1–20.
- [67] J.R. Alvarez Corena, Heterogeneous photocatalysis for the treatment of contaminants of emerging concern in water, Doctoral thesis, Worcester Polytechnic Institute (2015).
- [68] B. Neppolian, H. Choi, S. Sakthivel, B. Arabindoo, V. Murugesan, Solar light induced and TiO₂ assisted degradation of textile dye reactive blue 4, *Chemosphere* 46 (2002) 1173–1181.
- [69] M. Saquib, T.M. Abu, M. Haque, M. Muneer, Photocatalytic degradation of disperse blue 1 using UV/TiO₂/H₂O₂ process, *J. Environ. Manage.* 88 (2008) 300-306.
- [70] A. Ajmal, I. Majeed, R.N. Malik, H. Idriss, M.A. Nadeem, Principles and mechanisms of photocatalytic dye degradation on TiO₂ based photocatalysts: a comparative overview, *RSC Adv.* 4 (2014) 37003-70026.
- [71] D. Bamba, P. Atheba, D. Robert, A. Trokourey, B. Dongui, Photocatalytic degradation of the diuron pesticide, *Environ. Chem. Lett.* 6 (2008) 163-167.
- [72] M.N. Chong, B. Jin, Ch.W.K. Chow, Ch. Saint, Recent developments in photocatalytic water treatment technology: A review, *Water Research* 44 (2010) 2997-3027
- [73] H. Zhu, R. Jiang, Y. Fu, Y. Guan, J. Yao, L. Xiao, G. Zeng, Effective photocatalytic decolorization of methyl orange utilizing TiO₂/ZnO/chitosan nanocomposite films under simulated solar irradiation, *Desalination* 286 (2012) 41–48.
- [74] E.C. Ilinoiu, R. Pode, F. Manea, L.A. Colar, A. Jakab, C. Orha, C. Ratiu, C. Lazau, P. Sfarloaga, Photocatalytic activity of a nitrogen-doped TiO₂ modified zeolite in the degradation of Reactive Yellow 125 azo dye, *J. Taiwan Inst. Chem. Eng.* 44 (2013) 270–278.

- [75] I.K. Konstantinou, T.A. Albanis, TiO₂-assisted photocatalytic degradation of azo dyes in aqueous solution: Kinetic and mechanistic investigations – a review, *Appl. Catal. B Environ.* 49 (2004) 1-14.
- [76] I.K. Konstantinou, V.A. Sakkas, T.A. Albanis, Photocatalytic degradation of propachlor in aqueous TiO₂ suspensions. Determination of the reaction pathway and identification of intermediate products by various analytical methods, *Water Res.* 3 (2002) 2733-2748.
- [77] J. Peral, X. Domenech, D.F. Ollis, Heterogeneous photocatalysis for purification, decontamination and deodorization of air, *J. Chem. Technol. Biot.* 70 (1997) 117-140.
- [78] V. Belessi, D. Lambropoulou, I. Konstantinou, A. Katsoulidis, P. Pomonis, D. Petridis, T. Albanis, Structure and photocatalytic performance of TiO₂ / clay nanocomposites for the degradation of dimethachlor, *Appl. Catal. B: Environ.* 73 (2007) 292-299.
- [79] M. Movahedi, A.R. Mahjoub, S.J. Darzi, Photodegradation of Congo red in aqueous solution on ZnO as an alternative catalyst to TiO₂, *J. Iran. Chem. Soc.* 6 (2009) 570-577.
- [80] O. Moradi, K. Zare, Adsorption of Pb(II), Cd(II) and Cu(II) Ions in Aqueous Solution on SWCNTs and SWCNT –COOH Surfaces: Kinetics Studies, *Fuller. Nanotub. Car. N.* 19 (2011) 628-652.
- [81] J.H. Suna, K.E. Wang, R.X. Sun, S.Y. Dong, Mater. photodegradation of azo dye congo red from aqueous solution by the WO₃-TiO₂/activated carbon (AC) photocatalyst under the UV irradiation, *Chem. Phys.* 115 (2009) 303-308.
- [82] L.V. Bora, R.K. Mewada, Visible/solar light active photocatalysts for organic effluent treatment: Fundamentals, mechanisms and parametric review, *Renew. Sustainable Energy Rev.* 76 (2017) 1393–1421.
- [83] K. Mehrotra, G.S. Yablonsky, A.K. Ray, Macro kinetic studies for photocatalytic degradation of benzoic acid in immobilized systems, *Chemosphere* 60 (2005) 1427–1436.
- [84] I.A. Alaton, I.A. Balcioglu, D.W. Bahnemann, Advanced oxidation of a reactive dye bath effluent: comparison of O₃, H₂O₂/UV-C and TiO₂/UV-A processes, *Water Res.* 36 (2002) 1143–1154.

- [85] Y. Xua, C.H. Langford, Variation of Langmuir adsorption constant determined for TiO₂-photocatalyzed degradation of acetophenone under different light intensity. *J. Photochem. Photobiol. A: Chem.* 133 (2000) 67-71.
- [86] M.L. Chin, A.R. Mohamed, S. Bhatia, Performance of photocatalytic reactors using immobilized TiO₂ film for the degradation of phenol and methylene blue dye present in water stream, *Chemosphere* 57 (2004) 547-554.
- [87] S. Gelover, L.A. Gomez, K. Reyes, M. Teresa Leal, A practical demonstration of water disinfection using TiO₂ films and sunlight, *Water Res.* 40 (2006) 3274-3280.
- [88] E. Pelizzetti, Concluding remarks on heterogeneous solar photocatalysis, *Sol. Energ. Mat. Sol. Cells* 38 (1995) 453-457.
- [89] R.K. Wahi, Z. Liu, J.C. Falkner, V.L. Colvin, Solvothermal synthesis and characterization of anatase TiO₂ nanocrystals with ultrahigh surface area, *J. Colloid Interface Sci.* 302 (2006) 530–536.
- [90] G. Tian, H. Fu, L. Jing, B. Xin, K. Pan, Preparation and characterization of stable biphasic TiO₂ photocatalyst with high crystallinity, large surface area, and enhanced photoactivity, *J. Phys. Chem. C* 112 (2008) 3083–3089.
- [91] H.W. Wang, C.H. Kuo, H.C. Lin, I.T. Kuo, C.F. Cheng, Rapid formation of active mesoporous TiO₂ photocatalysts via micelle in a microwave hydrothermal process, *J. Am. Ceram. Soc.* 89 (2006) 3388–3392.
- [92] Z. Tong, Y. Jiang, D. Yang, J. Shi, Sh. Zhang, Ch. Liua, Z. Jiang, Biomimetic and bioinspired synthesis of titania and titania-based materials, *RSC Adv.* 4 (2014) 12388-12403.
- [93] D.W. Lee, K.H. Lee, Novel eco-friendly synthesis of sucrose-templated mesoporous titania with high thermal stability, *Microporous Mesoporous Mater.* 142 (2011) 98–103.
- [94] Y.S. Chang, Y.C. Lee, J. Yuhara, L.H. Chan, L.G. Teoh, H.M. Chen, Effect of water on the formation of nanostructured mesoporous titania, *Curr. App. Phys.* 11 (2011) 486–491.
- [95] A. Sun, Z. Li, M. Li, G. Xu, Y. Li, P. Cui, Room temperature synthesis of spherical mesoporous titania, *Powder Technol.* 201 (2010) 130–137.

- [96] A. Fujishima, K. Honda, Electrochemical Photolysis of Water at a Semiconductor Electrode, *Nature*, 238 (1972) 37-38.
- [97] P. Periyat, N. Leyland, D.E. McCormack, J. Colreavy, D. Corrc, S.C. Pillai, Rapid microwave synthesis of mesoporous TiO₂ for electrochromic displays, *J. Mater. Chem.* 20 (2010) 3650–3655.
- [98] J. Yu, M. Zhou, B. Cheng, H. Yu, X. Zhao, Ultrasonic preparation of mesoporous titanium dioxide nanocrystalline photocatalysts and evaluation of photocatalytic activity, *J. Mol. Catal. A: Chemical* 227 (2005) 75–80.
- [99] X. Chen, S.S. Mao, Titanium dioxide nanomaterials: synthesis, properties, modifications, and applications, *Chem. Rev.* 107 (2007) 2891-2959.
- [100] S. Acosta, R. Corriu, D. Leclercq, P.H. Mutin, A. Vioux, Novel non-hydrolytic sol-gel route to metal oxide, *J. Sol-Gel Sci. Tehnol.*, 2 (1994) 25-28.
- [101] A. Vioux, Nonhydrolytic sol-gel routes to oxides, *Chem. Mater.* 9 (1997) 2292–2299.
- [102] M. Niederberger, N. Pinna, Metal oxide nanoparticles in organic solvents: synthesis, formation, assembly and application, Springer, 2009.
- [103] M.N. Rahman, Ceramic Processing and Sintering, Marcel Dekker, New York, 2003.
- [104] S. Bagheri, Z.A.M. Hir, A.T. Yousefi, Sh.B.A. Hamid, Progress on mesoporous titanium dioxide: Synthesis, modification and applications, *Microporous Mesoporous Mater.* 218 (2015) 206-222.
- [105] J. Livage, M. Henry, C. Sanchez, Sol-gel chemistry of transition metal oxides. *Prog. Solid State Chem.* 18 (1988) 259–341
- [106] A.Vioux, D.Leclercq, Non-aqueous routes to sol-gel, *Heterogen. Chem. Rev.*3 (1996) 65-73.
- [107] N. Tanasković, Ž. Radovanović, V. Đokić, J. Krstić, S. Drmanić, Dj. Janačković, R. Petrović, Synthesis of mesoporous nanocrystalline titania powders by non- hydrolytic sol-gel method, *Superlattices Microstruct.* 46 (2009) 217–222.
- [108] P. Arnal, R.J. P.Corriu, D. Leclercq, P.H. Mutin, A.A. Vioux, Solution chemistry study of nonhydrolytic sol-gel routes to titania, *Chem. Mater.* 9 (1997) 694–698.

- [109] J. Zhu, Z.F. Bian, J. Ren, Y.M. Liu, Y. Cao., H.X. Li, W.L. Dai, H.Y. He, K.N. Fan, An integrated low temperature approach to highly photoactive nanocrystalline mesostructured titania, *Catal. Commun.* 8 (2007) 971–976.
- [110] Z. Jiang, F. Yang, N. Luo, B.T.T. Chu, D. Sun, H. Shi, T. Xiao, P.P. Edwards, Solvothermal synthesis of N-doped TiO₂ nanotubes for visible-light-responsive photocatalysis, *Chem. Commun.* 47 (2008) 6372–6374.
- [111] H.J. Kim, J.D. Jeon, S.Y. Kwak, Highly dispersed mesoporous TiO₂ spheres via acid treatment and its application for dye-sensitized solar cells, *Powder Technol.* 243 (2013) 130–138.
- [112] J. Li, W. Wan, H. Zhou, J. Li, D. Xu, Hydrothermal synthesis of TiO₂(B) nanowires with ultrahigh surface area and their fast charging and discharging properties in Li-ion batteries, *Chem. Commun.* 47 (2011) 3439–3441.
- [113] Q. Xiang, J. Yu, W. Wang, M. Jaroniec, Nitrogen self-doped nanosized TiO₂ sheets with exposed {001} facets for enhanced visible-light photocatalytic activity, *Chem. Commun.* 47 (2011) 6906–6908.
- [114] R. Zhang, A.A. Elzatahry, S.S. Al-Deyab, D. Zhao, Mesoporous titania: From synthesis to application, *Nano Today* 7 (2012) 344–366.
- [115] Wu. Zhiwang, Lu. Yunfeng, Aerosol-assisted synthesis of mesoporous titania nanoparticles with high surface area and controllable phase composition, *J. Sol-Gel Sci. Technol.* 53 (2010) 287–292.
- [116] I. Janković-Častvan, S. Lazarević, B. Jordović, R. Petrović, D. Tanasković, Dj. Janačković, Electrical properties of cordierite obtained by non-hydrolytic sol-gel method, *J. Eur. Ceram. Soc.* 27 (2007) 3659–3661.
- [117] I. Janković-Častvan, S. Lazarević, D. Tanasković, A. Orlović, R. Petrović, Dj. Janačković, Phase transformation in cordierite gel synthesized by non-hydrolytic sol-gel route, *Ceram. Int.* 33 (2007) 1263–1268.
- [118] C. Guo, M. Ge, L. Liu, G. Gao, Y. Feng, Y. Wang, Directed synthesis of mesoporous TiO₂ microspheres: catalysts and their photocatalysis for bisphenol A degradation, *Environ. Sci. Technol.* 44 (2010) 419–425
- [119] D. Chen, F. Huang, Y.B. Cheng, R.A. Caruso, Mesoporous anatase TiO₂ beads with high surface areas and controllable pore sizes: A superior candidate for high-performance dye-sensitized solar cells, *Adv. Mater.* 21 (2009) 2206–2210.

- [120] R. Dewil, D. Mantzavinos, I. Poulios, M.A. Rodrigo, New perspectives for advanced oxidation processes, *J. Environ. Manage.* 195 (2017) 93-99
- [121] M. Kitano, M. Matsuoka, M. Veshima, M. Anpo, Recent developments in titanium oxide-based photocatalysts: review. *Appl. Catal. A: Gen.*, 325 (2007) 1-14.
- [122] F. Peng, L. Cai, L. Huang, H. Yu, H. Wang, Preparation of nitrogen-doped titanium dioxide with visible light photocatalytic activity using a facile hydrothermal method, *J. Phys. Chem. Sol.* 69 (2008) 1657-1664.
- [123] V. Etacheria, C.D. Valentinc, J. Schneiderd, D. Bahnemannd, S.C. Pillai, Visible-light activation of TiO₂ photocatalysts: Advances in theory and experiments, *J. Photochem. Photobiol. C: Photochem. Rev.* 25 (2015) 1–29.
- [124] W. Choi, A. Termin, M.R. Hoffmann, the role of metal ion dopants in quantum-sized TiO₂: correlation between photoreactivity and charge carrier recombination dynamics, *J. Phys. Chem. B* 98 (1994) 13669-13679.
- [125] N. Serpone, Relative photonic efficiencies and quantum yields in heterogeneous photocatalysis, *J. Photochem. Photobiol A* 104 (1997) 1-12.
- [126] M.M. Mahlambi, C.J. Ngila, B.B. Mamba, Recent developments in environmental photocatalytic degradation of organic pollutants: the case of titanium dioxide nanoparticles- A review, *J. Nanomater.* 2015 (2015) 1-29.
- [127] O. Diwald, T.L. Thompson, T. Zubkov, E.G. Goralski, S.D. Walck, J.T.Jr. Yates, Photochemical activity of nitrogen doped rutile TiO₂ (110) in visible light, *J. Phys. Chem. B* 108 (2004) 6004–6008.
- [128] S. Livraghi, C. Paganini, E. Giamello, A. Selloni, C.D. Valentin, G. Pacchioni, Origin of photoactivity of nitrogen doped titanium dioxide under visible light, *J. Am. Chem. Soc.* 128 (2006) 15666–15671.
- [129] L.G. Devi, S.G. Kumar, Exploring the critical dependence of adsorption of various dyes on the degradation rate using Ln³⁺-TiO₂ surface under UV/solar light, *Appl. Surf. Sci.* 261 (2012) 137–146.
- [130] G. Shao, F. Wang, T. Ren, Y. Liu, Z. Yuan, Hierarchical mesoporous phosphorus and nitrogen doped titania materials: Synthesis, characterization and visible-light photocatalytic activity, *Appl. Catal. B: Environ.* 92 (2009) 61–67.

- [131] A. Charanpahari, S.S. Umare, S.P. Gokhale, V. Sudarsan, B. Sreedhar, R. Sasikala, Enhanced photocatalytic activity of multi-doped TiO₂ for the degradation of methyl orange, *Appl. Catal. A: Gen.* 443–444 (2012) 96–102.
- [132] E.A. Kozlova, T.P. Lyubina, M.A. Nasalevich, A.V. Vorontsov, A.V. Miller, V.V. Kaichev, V.N. Parmon, Influence of the method of platinum deposition on activity and stability of Pt/TiO₂ photocatalysts in the photocatalytic oxidation of dimethyl methylphosphonate, *Catal. Commun.* 12 (2011) 597–601.
- [133] S. Yin, T. Sato, Photocatalytic activity of platinum loaded fibrous titania prepared by solvothermal process, *J. Photochem. Photobiol. A: Chemistry* 169 (2005) 89–94
- [134] J. Liu, R. Han, Y. Zhao, H. Wang, W. Lu, T. Yu, Y. Zhang, Enhanced Photoactivity of V–N Co doped TiO₂ Derived from a Two-Step Hydrothermal Procedure for the Degradation of PCP–Na under Visible Light Irradiation, *J. Phys. Chem. C* 115 (2011) 4507–4515.
- [135] T. Ohno, T. Mitsui, M. Matsumura, Photocatalytic activity of S-doped TiO₂ photocatalyst under visible light, *Chem. Lett.* 32 (2003) 364–365
- [136] L. Pan, J. Zou, X. Zhang, L. Wang, Water-mediated promotion of dye sensitization of TiO₂ under visible light, *J. Am. Chem. Soc.* 133 (2011) 10000–10002.
- [137] F. Zuo, L. Wang, T. Wu, Z. Zhang, B. Borchardt, P. Fen, Self-doped Ti³⁺ enhanced photocatalyst for hydrogen production under visible light, *J. Am. Chem. Soc.* 132 (2010) 11856–11857.
- [138] S.Y. Lee, S.J. Park, TiO₂ photocatalyst for water treatment applications, *J. Ind. Eng. Chem.* 19 (2013) 1761–1769.
- [139] R.F. Chen, C.X. Zhang, J. Deng, G.Q. Song, Preparation and photocatalytic activity of Cu²⁺-doped TiO₂/SiO₂, *Int. J. Min. Met. Mater.* 16 (2009) 220–225.
- [140] J.C. Xu, M. Lu, X.Y. Guo, H.L. Li, Zinc ions surface doped titanium dioxide nanotubes and its photocatalysis activity for degradation of methyl orange in water, *J. Mol. Catal. A* 226 (2005) 123–127.
- [141] C.T. Hsieh, W.S. Fan, W.Y. Chen, J.Y. Lin, Adsorption and visible-light-derived photocatalytic kinetics of organic dye on co-doped titania nanotubes prepared by hydrothermal synthesis, *Sep. Purif. Technol.* 67 (2009) 312–318.

- [142] S.G. Kumar, L.G. Devi, Review on modified TiO₂ photocatalysis under UV/Visible light: Selected results and related mechanisms on interfacial charge carrier transfer dynamics, *J. Phys. Chem. A* 115 (2011) 13211–13241.
- [143] H. Zhang, G. Chen, D.W. Bahnemann, Photoelectrocatalytic materials for environmental applications, *J. Mater. Chem.* 19 (2009) 5089–5121
- [144] A.W. Morawski, M. Janus, B. Tryba, M. Inagaki, K. Kałucki, TiO₂ anatase modified by carbon as the photocatalyst under visible light, *C. R. Chim.* 9 (2006) 800–805.
- [145] C. Jin, S. Qiu, Y. Zhu, Y. Xie, Phosphorous-modified TiO₂ with excellent thermal stability and its application to the degradation of pollutants in water, *Chin. J. Catal.* 32 (2011) 1173–1179
- [146] D. Chen, Z. Jiang, J. Geng, Q. Wang, D. Yang, Carbon and nitrogen co-doped TiO₂ with enhanced visible-light photocatalytic activity, *Ind. Eng. Chem. Res.* 46 (2007) 2741–2746.
- [147] H. Dong, G. Zeng, L. Tang, Ch. Fan, Ch. Zhang, X. He, Y. He, An overview on limitations of TiO₂-based particles for photocatalytic degradation of organic pollutants and the corresponding countermeasures, *Water Res.* 79 (2015) 128–146.
- [148] S.Z. Chen, P.Y. Zhang, D.M. Zhuang, W.P. Zhu, Catalytic combustion of methane over NiO/Ce_{0.75}Zr_{0.25}O₂ catalyst, *Catal. Commun.* 5 (2004) 677–680.
- [149] Y. Nosaka, M. Matsushita, J. Nishino, A.Y. Nosaka, Nitrogen-doped titanium dioxide photocatalysts for visible response prepared by using organic compounds, *Sci. Tech. Adv. Mater.* 6 (2005) 143–148.
- [150] S. Livraghi, M. Chierotti, E. Giamello, G. Magnacca, M.C. Paganini, G. Cappelletti, C. Bianchi, Nitrogen-Doped titanium dioxide active in photocatalytic reactions with visible light: a multi-technique characterization of differently prepared materials, *J. Phys. Chem. C* 112 (2008) 17244–17252.
- [151] S. Sato, Photocatalytic activity of NO_x-doped TiO₂ in the visible light region, *Chem. Phys. Lett.* 123 (1986) 126–128.
- [152] R. Ashai, T. Morikawa, T. Ohwaki, K. Aoki, Y. Taga, Visible-light photocatalysis in nitrogen-doped titanium oxides, *Science* 293 (2001) 269–271.

- [153] A.T. Kuvarega, R.W.M. Krause, B.B. Mamba, Nitrogen/palladium-codoped TiO₂ for efficient visible light photocatalytic dye degradation, *J. Phys. Chem. C* 115 (2011) 22110–22120.
- [154] G. Liu, X. Wang, Z. Chen, H.M. Cheng, G.Q. Lu, The role of crystal phase in determining photocatalytic activity of nitrogen doped TiO₂, *J. Colloid Interface Sci.* 329 (2009) 331–338.
- [155] C. Di Valentin, E. Finazzi, G. Pacchioni, A. Selloni, S. Livraghi, M.C. Paganini, E. Giamello, N-doped TiO₂: theory and experiment, *Chem. Phys.* 339 (2007) 44–56.
- [156] N. Serpone, Is the band gap of pristine TiO₂ narrowed by anion- and cation-doping of titanium dioxide in second-generation photocatalysts? *J. Phys. Chem. B* 110 (2006) 24287–24293.
- [157] A. Zaleska, Doped-TiO₂: A Review, *Recent Pat. Eng.* 2 (2008) 157-164
- [158] H. Irie, Y. Watanabe, K. Hashimoto, Nitrogen- concentration dependence on photocatalytic activity of TiO₂-xNx Powders, *J. Phys. Chem. B* 107 (2003) 5483-5486.
- [159] M. M. Dubinin, *Progress in Surface and Membrane Science*, Academic Press, New York, 1975.
- [160] G. Liu, L. Wang, H.G. Yang, H.-M. Cheng, G.Q. Lu, Titania-based photocatalysts-crystal growth, doping and heterostructuring, *J. Mater. Chem.* 20 (2010) 831-843
- [161] C.D. Valentin, G. Pacchioni, A. Selloni, S. Livraghi, E. Giamello, Characterization of paramagnetic species in N-doped TiO₂ powders by EPR spectroscopy and DFT calculations, *J. Phys. Chem. B* 109 (2005) 11414–11419.
- [162] T. Phongamwong, M. Chareonpanich, J. Limtrakul, Role of chlorophyllin Spirulina on photocatalytic activity of CO₂ reduction under visible light over modified N-doped TiO₂ photocatalysts, *Appl. Catal. B: Environ.* 168–169 (2015) 114–124.
- [163] Ch.W. Dunnill, I.P. Parkin, Nitrogen-doped TiO₂ thin films: photocatalytic applications for healthcare environments, *Dalton Trans.* 40 (2011) 1635-1640.

- [164] F.E. Oropeza, J. Harmer, R.G. Egdell, R.G. Palgrave, A critical evaluation of the mode of incorporation of nitrogen in doped anatase photocatalysts, *Phys. Chem. Chem. Phys.* 12 (2010) 960–969.
- [165] J. Ananpattarachai, P. Kajitvichyanukul, S. Seraphin, Visible light absorption ability and photocatalytic oxidation activity of various interstitial N-doped TiO₂ prepared from different nitrogen dopants, *J. Hazard. Mater.* 168 (2009) 253–261
- [166] S.A. Ansari, M.M Khan, M. O. Ansari, M.H. Cho, Nitrogen-doped titanium dioxide (N-doped TiO₂) for visible light photocatalysis, *New J. Chem.* 40 (2016) 3000-3009.
- [167] A. Ghicov, J.M. Macak, H. Tsuchiya, J. Kunze, V. Haeublein, L. Frey et al., Ion implantation and annealing for an efficient N-doping of TiO₂ nanotubes, *Nano Lett.* 6 (2006) 1080–1082.
- [168] J.M. Mwabora, T. Lindgren, E. Avendaño, T.F. Jaramillo, J. Lu, S.E. Lindquist, C.G. Granqvist, Structure composition and morphology of photoelectron chemically active TiO₂-xNx thin films deposited by reactive DC magnetron sputtering, *J. Phys. Chem. B* 108 (2004) 20193–20198.
- [169] X.B. Chen, C.C. Burda, Photoelectron spectroscopic investigation of nitrogen-doped titania nanoparticles, *J. Phys. Chem. B* 108 (2004) 15446–15449.
- [170] C. Burda, Y. Lou, X. Chen, A.C.S. Samia, J. Stout, J.L. Gole, Enhanced nitrogen doping in TiO₂ nanoparticles, *Nano Lett.* 3 (2003) 1049–1051.
- [171] F. Peng, L. Cai, L. Huang, H. Yu, H. Wang, Preparation of nitrogen-doped titanium dioxide with visible light photocatalytic activity using a facile hydrothermal method, *J. Phys. Chem. Sol.* 69 (2008) 1657-1664.
- [172] Y. Aita, M. Komatsu, S. Yin, T. Sato, Phase-compositional control and visible light photocatalytic activity of nitrogen-doped titania via solvothermal process, *J. Solid State Chem.* 177 (2004) 3235–3238.
- [173] J.L. Gole, J.D. Stout, C. Burda, Y.B. Lou, X.B. Chen, Highly efficient formation of visible light tunable TiO₂-xNx photocatalysts and their transformation at the nanoscale, *J. Phys. Chem. B* 108 (2004) 1230–1240.
- [174] T. Ihara, M. Miyoshi, Y. Iriyama, O. Matsumoto, S. Sugihara, Visible-light-active titanium oxide photocatalyst realized by an oxygen-deficient structure and by nitrogen doping, *Appl. Catal. B: Environ.* 42 (2003) 403-409.

- [175] K. Kobayakawa, Y. Murakami, Y. Sato, Visible-light active N-doped TiO₂ prepared by heating of titanium hydroxide and urea J. Photochem. Photobiol. A: Chem. 170 (2005) 177.
- [176] X. Fang, Z. Zhang, Q. Chen, H. Ji, X. Gao, Dependence of nitrogen doping on TiO₂ precursor annealed under NH₃ flow, J. Solid State Chem. 180 (2007) 1325–1332.
- [177] X. Li, P. Liu, Y. Mao, M. Xing, J. Zhang, Preparation of homogeneous nitrogen-doped mesoporous TiO₂ spheres with enhanced visible-light photocatalysis, Appl. Catal. B: Environ. 164 (2015) 352–359.
- [178] A.V. Emeline, V.N. Kuznetsov, V.K. Rybchuk, N. Serpone, Visible-light-active titania photocatalysts: the case of N-doped TiO₂—properties and some fundamental issues, Int. J. Photoenergy 2008 (2008) 258394–258413.
- [179] Y. Irokawa, T. Morikawa, K. Aoki, S. Kosaka, T. Ohwaki, Y. Taga, Photodegradation of toluene over TiO_{2-x}N_x under visible light irradiation, Phys. Chem. Chem. Phys. 8 (2006) 1116–1121.
- [180] G. Liu, F. Li, Z. Cheng, G. Qing Lu, H-M. Cheng, The role of NH₃ atmosphere in preparing nitrogen-doped TiO₂ by mechanochemical reaction, J. Solid State Chem. 179 (2006) 331–335.
- [181] S. Mozia, M. Tomaszewska, B. Kosowska, B. Grzmil, A.W. Morawski, K. Kałucki, Decomposition of nonionic surfactant on a nitrogen-doped photocatalyst under visible-light irradiation, J. Appl. Catal. B: Environ. 55 (2005) 195–200.
- [182] In- C. Kang, Q. Zhang., J. Kano, S. Yin, T. Sato, F. Saito, Synthesis of nitrogen doped TiO₂ by grinding in gaseous NH₃, J. Photochem. Photobiol. A: Chemistry 189 (2007) 232–238.
- [183] W. Balcerski, S.Y. Ryu, M.R. Hoffmann, Visible- light photoactivity of nitrogen-doped TiO₂: Photo-oxidation of HCO₂H to CO₂ and H₂O, J. Phys. Chem. C 111 (2007) 15357–15362.
- [184] F. Peng, L. Cai, H. Yu, H. Wang, J. Yang, Synthesis and characterization of substitutional and interstitial nitrogen-doped titanium dioxides with visible light photocatalytic activity, J. Solid. State. Chem. 181 (2008) 130–136

- [185] J. Wang, D.N. Tafen, J.P. Lewis, Z. Hong, A. Manivannan, M. Zhi, M. Li, N. Wu, Origin of photocatalytic activity of nitrogen-doped TiO₂ nanobelts, *J. Am. Chem. Soc.* 131 (2009) 12290–12297.
- [186] K. Kalantari, M. Kalbasi, M. Sohrabi, S.J. Royae, Synthesis and characterization of N-doped TiO₂ nanoparticles and their application in photocatalytic oxidation of dibenzothiophene under visible light, *Ceram. Int.* 42 (2016) 14834–14842.
- [187] T. Umebayashi, T. Yamaki, H. Itoh, K. Asai, Band gap narrowing of titanium dioxide by sulfur doping, *Appl. Phys. Lett.* 81 (2002) 454–456.
- [188] Y. Cui, H. Du, L. Wen, Origin of visible- light induced photocatalytic properties of S-doped anatase TiO₂ by first-principles investigation, *Solid State Commun.* 149 (2009) 634–637.
- [189] M. Harb, P. Sautet, P. Raybaud, Anionic or cationic S-doping in bulk anatase TiO₂: Insights on optical absorption from first principles calculations, *J. Phys. Chem. C* 117 (2013) 8892–8902.
- [190] S. Sun, J. Zhang, P. Gao, Y. Wang, X. Li, T. Wu, Y. Wang, Y. Chen, P. Yang, Full visible-light absorption of TiO₂ nanotubes induced by anionic S₂²⁻ doping and their greatly enhanced photocatalytic hydrogen production abilities, *Appl. Catal. B: Environ.* 206 (2017) 168–174.
- [191] S. Abu Bakar, C. Ribeiro, A comparative run for visible-light-driven photocatalytic activity of anionic and cationic S-doped TiO₂ photocatalysts: A case study of possible sulfur doping through chemical protocol, *J. Mol. Catal. A: Chem.* 421 (2016) 1–15.
- [192] A. Sclafani, Comparison of the photoelectronic and photocatalytic activities of various anatase and rutile forms of titania in pure liquid organic phases and in aqueous solutions, *J. Phys. Chem.* 100 (1996) 13655–13661.
- [193] Y.R. Do, K. Lee, K. Dwight, W. Wold, The Effect of WO₃ on the Photocatalytic Activity of TiO₂, *J. Solid State Chem.* 108 (1994) 198–201.
- [194] C. McManamon, J. O’Connell, P. Delaney, S. Rasappa, J.D. Holmes, M.A. Morris, A facile route to synthesis of S-doped TiO₂ nanoparticles for photocatalytic activity, *J. Mol. Catal. A: Chem.* 406 (2015) 51–57.

- [195] T. Tachikawa, S. Tojo, K. Kawai, M. Endo, M. Fujitsuka, T. Ohno, K. Nishijima, Z. Miyamoto, T. Majima, Photocatalytic oxidation reactivity of holes in the sulfur and carbon-doped TiO₂ powders studied by time resolved diffuse reflectance spectroscopy, *J. Phys. Chem. B*, 108 (2004) 19299-19306.
- [196] Y.H Lina, H.T. Hsuehb, C.W. Changa, H. Chua, The visible light-driven photodegradation of dimethyl sulfide on S-doped TiO₂: Characterization, kinetics, and reaction pathways, *Appl. Catal. B: Environ.* 199 (2016) 1–10
- [197] C.W. Dunnill, Z.A. Aiken, A. Kafizas, J. Pratten, M. Wilson, D.J. Morgan, et al., White light induced photocatalytic activity of sulfur-doped TiO₂ thin films and their potential for antibacterial application, *J. Mater. Chem.* 19 (2009) 8747-8754.
- [198] P. Periyat, S.C. Pillai, D.E. McCormack, J. Colreavy, S.J. Hinder, Improved High-Temperature Stability and Sun-Light-Driven Photocatalytic activity of sulfur-doped anatase TiO₂, *J. Phys. Chem. C* 112 (2008) 7644–7652.
- [199] L. Szatmáry, S. Bakardjieva, J. Šubrt, P. Bezdička, J. Jirkovský, Z. Bastl, V. Brezová, M. Korenko, Sulphur doped nanoparticles of TiO₂, *Catal. Today* 161 (2011) 23-28.
- [200] F. Huang, A. Yan, H. Zhao, Influences of doping on photocatalytic properties of TiO₂ photocatalyst, *Semiconductor Photocatalysis - Materials, Mechanisms and Applications*, INTECH, 2016.
- [201] M. Maitri, K. Sivaranjani, D.S. Bhange, B. Saha, P. Chakraborty, A.K. Viswanath, C.S. Gopinath, Structure, electronic structure, optical, and dehydrogenation catalytic study of (Zn_{1-z}In_z)(O_{1-x}N_x) solid solution, *Chem. Mater.* 22 (2010) 565–578.
- [202] J. Graciani, A. Nambu, J. Evans, J.A. Rodriguez, J.F. Sanz, Au ↔ N synergy and N-doping of metal oxide-based photocatalysts, *J. Am. Chem. Soc.* 130 (2008) 12056–12063.
- [203] W. Wang, Y. Ni, C. Lu, Z. Xu, Hydrogenation temperature related inner structures and visible-light-driven photocatalysis of N-F co-doped TiO₂ nanosheets, *Appl. Surf. Sci.* 290 (2014) 125–130.

- [204] V. Etacheri, M.K. Seery, S.J. Hinder, S.C. Pillai. Nanostructured $\text{Ti}_{1-x}\text{S}_x\text{O}_{2-y}\text{N}_y$ heterojunctions for efficient visible-light-induced photocatalysis. *Inorg. Chem.* 51 (2012) 7164–7173.
- [205] J. Wang, Hui Li, Hongyi Li, C. Zou, Mesoporous $\text{TiO}_{2-x}\text{A}_y$ (A = N, S) as a visible-light- response photocatalyst, *Solid State Sci.* 12 (2010) 490–497.
- [206] J.A. Rengifo-Herrera, K. Pierzchala, A. Sienkiewich, L. Forro, J.E. Moser, C. Pulgarin, Synthesis, characterization, and photocatalytic activities of nanoparticulate N, S-codoped TiO_2 having different surface-to-volume ratios, *J. Phys. Chem. C* 114 (2010) 2717–2723.
- [207] M. Grandcolas, J. Ye, Preparation of fine, uniform nitrogen- and sulfur-modified TiO_2 nanoparticles from titania nanotubes, *Sci. Tech. Adv. Mater.* 11 (2010) 1-6
- [208] B. Naik, K.M. Parida, C.S. Gopinath, Facile Synthesis of N- and S-incorporated nanocrystalline TiO_2 and direct solar-light-driven photocatalytic activity, *J. Phys. Chem. C* 114 (2010) 19473–19482.
- [209] N. Yao, C. Wu, L. Jia, S. Han, B. Chi, J. Pu, L. Jian, Simple synthesis and characterization of mesoporous (N, S)-codoped TiO_2 with enhanced visible light photocatalytic activity, *Ceram. Int.* 38 (2012) 1671–1675.
- [210] Y. Zhang, P. Liu, H. Wu, Development of high efficient visible light-driven N,S-codoped TiO_2 nanowires photocatalysts, *Appl. Surf. Sci.* 328 (2015) 335–343.
- [211] M. Behpour, V. Atouf, Study of the photocatalytic activity of nanocrystalline S,N-codoped TiO_2 thin films and powders under visible and sun light irradiation, *Appl. Surf. Sci.* 258 (2012) 6595–6601.
- [212] J. Ju, X. Chen, Y. Shi, J. Miao, D. Wu, Hydrothermal preparation and photocatalytic performance of N, S-doped nanometer TiO_2 under sunshine irradiation, *Powder Technol.* 237 (2013) 616–622.
- [213] J. Yu, M. Zhoua, B. Cheng, X. Zhao, Preparation, characterization and photocatalytic activity of in situ N, S-co doped TiO_2 powders, *J. Mol. Catal. A Chem.* 246 (2006) 176–184.
- [214] A. Albrbar, V. Djokić, A. Bjelajac, J. Kovač, J. Ćirković, M. Mitrić, Dj. Janačković, R. Petrović, Visible-light active mesoporous, nanocrystalline N,S-

- doped and co-doped titania photocatalysts synthesized by non-hydrolytic sol-gel route, *Ceram. Int.* 42 (2016) 16718–16728.
- [215] H. Kisch, S. Sakthivel, M. Janczarek, D. Mitoraj, A low-band gap, nitrogen modified titania visible-light photocatalyst, *J. Phys. Chem. C* 111 (2007) 11445–11449.
- [216] V. Nadtochenko, N. Denisov, A. Gorenberg, Yu. Kozlov, P. Chubukov, J.A. Rengifo, C. Pulgarin, J. Kiwi, Correlations for photocatalytic activity and spectral features of the absorption band edge of TiO₂ modified by thiourea, *Appl. Catal. B Environ.* 91 (2009) 460–469.
- [217] M.J. Kim, K.H. Choo, H.S. Park, Photocatalytic degradation of seawater organic matter using a submerged membrane reactor, *J. Photochem. Photobiol. A* 216 (2010) 215-220.
- [218] M.N. Chong, B. Jin, C.W.K. Chow, C. Saint, Recent developments in photocatalytic water treatment technology: a review, *Water Res.* 44 (2010) 2997-3027.
- [219] M. Makita, A. Harata, Photocatalytic decolorization of rhodamine B dye as a model of dissolved organic compounds: Influence of dissolved inorganic chloride salts in seawater of the Sea of Japan, *Chem. Eng. Process.* 47 (2008) 859-863.
- [220] G. Wang, L. Xu, J. Zhang, T. Yin, H. Deyan, Enhanced photocatalytic activity of TiO₂ powders (P25) via calcination treatment, *Int. J. Photoenergy* 2012 (2012) 1-9.
- [221] M. Kosmulski, Compilation of PZC and IEP of sparingly soluble metal oxides and hydroxides from literature. *Adv. Colloid Interface Sci.* 152 (2009) 14-25.
- [222] S. Milonjić, A. Ruvarac, M. Šušić, The heat of immersion of natural magnetite in aqueous solutions, *Thermochim. Acta* 11 (1975) 161-266.
- [223] R. Al-Rasheed, D.J. Cardin, Photocatalytic degradation of humic acid in saline waters. Part 1. Artificial seawater: influence of TiO₂, temperature, pH, and air-flow, *Chemosphere* 51 (2003) 925-933.
- [224] D. Mijin, M. Radulović, D. Zlatić, P. Jovančić, Photocatalytic degradation of textile dye C.I. reactive orange 16 in TiO₂ water suspension by simulated solar light, *Chem. Ind. Chem. Eng. Q.* 13 (2007) 179-185.

- [225] R. Al-Rasheed, D. J. Cardin, Photocatalytic degradation of humic acid in saline waters. Part 2. Effect of various photocatalytic materials, *Appl. Catal. A: Gen.* 246 (2003) 39-48.
- [226] C. Guillard, E. Puzenat, H. Lachheb, A. Houas, J.M. Herrmann, Why Inorganic Salts Decrease the TiO₂ Photocatalytic Efficiency, *Int. J. Photoenergy* 7 (2005) 1-9.
- [227] D.C. Hurum, A.G. Agrios, K.A. Gray, T. Rajh, M.C. Thurnauer, Explaining the enhanced photocatalytic activity of Degussa P25 mixed-phase TiO₂ using EPR, *J. Phys. Chem., B* 107 (2003) 4545-4549.
- [228] X. Wang, Y. Liu, Z. Hu, Y. Chen, W. Liu, G. Zhao, Degradation of methyl orange by composite photocatalysts nano-TiO₂ immobilized on activated carbons of different porosities, *J. Hazard. Mater.* 169 (2009) 1061-1067.
- [229] Z. Sun, L. Zheng, S. Zheng, R. L. Frost, Preparation and characterization of TiO₂/acid leached serpentinite tailings composites and their photocatalytic reduction of chromium(VI), *J. Colloid Interf. Sci.* 404 (2013) 102-109.
- [230] A. V. Emeline, V. K. Ryabchuk, N. Serpone, Dogmas and misconceptions in heterogeneous photocatalysis. Some enlightened reflections, *J. Phys. Chem., B* 109 (2005) 18515-18521.
- [231] J. Zhu, J. Yang, Z.F. Bian, J. Ren, Y.M. Liu, Y. Cao, H.X. Li, H.Y. He, K.N. Fan, Nanocrystalline anatase TiO₂ photocatalysts prepared via a facile low temperature nonhydrolytic sol-gel reaction of TiCl₄ and benzyl alcohol, *Appl. Catal. B: Environ.* 76 (2007) 82-91.
- [232] S. Lee, I.S. Cho, D.K. Lee, D.W. Kim, T.H. Noh, C.H. Kwak, S. Park, K.S. Hong, J. K. Lee, H.S. Jung, Influence of nitrogen chemical states on photocatalytic activities of nitrogen-doped TiO₂ nanoparticles under visible light, *J. Photochem. Photobiol. A* 213 (2010) 129-135.
- [233] K.A. Michalow, D. Logvinovich, A. Weidenkaff, M. Amberg, G. Fortunato, A. Heel, T. Graule, M. Rekas, Synthesis, characterization and electronic structure of nitrogen-doped TiO₂ nanopowder, *Catal. Today* 144 (2009) 7-12.
- [234] C. Song, X. Zhang, C. Jia, P. Zhou, X. Quan, C. Duan, Highly sensitive and selective fluorescence sensor based on functional SBA-15 for detection of Hg²⁺ in aqueous media, *Talanta* 81 (2010) 643-649.

- [235] K.S.W. Sing, D.H. Everett, R.A.W. Haul, L. Moscou, R.A. Pierotti, J. Rouquerol, T. Siemieniewska, Reporting physisorption data for gas/solid systems with special reference to the determination of surface area and porosity, *Pure Appl. Chem.* 57 (1985) 603–619.
- [236] G. Zhang, Y.C. Zhang, M. Nadagouda, C. Han, K. O’Shea, S.M. El-Sheikh, A. A. Ismail, D.D. Dionysiou, Visible light-sensitized S,N and C co-doped polymorphic TiO₂ for photocatalytic destruction of microcystin-LR, *Appl. Catal. B: Environ.* 144 (2014) 614–621.
- [237] X. Bu, Y. Wang, J. Li, C. Zhang, Improving the visible light photocatalytic activity of TiO₂ by combining sulfur doping and rectorite carrier, *J. Alloy. Compd.* 628 (2015) 20–26.
- [238] J. Lv, T. Sheng, L. Su, G. Xu, D. Wang, Z. Zheng, Y. Wu, N, S co-doped-TiO₂/fly ash beads composite material and visible light photocatalytic activity, *Appl. Surf. Sci.* 284 (2013) 229–234.
- [239] J.C. Yu, W. Ho, J. Yu, H. Yip, P.K. Wong, J. Zhao, Efficient visible-light-induced photocatalytic disinfection on sulfur-doped nanocrystalline titania, *Environ. Sci. Technol.* 39 (2005) 1175–1179.
- [240] L. Zeng, Z. Lu, M. Li, J. Yang, W. Song, D. Zeng, C. Xie, A modular calcination method to prepare modified N-doped TiO₂ nanoparticle with high photocatalytic activity, *Appl. Catal. B: Environ.* 183 (2016) 308–316.
- [241] D. Dolat, D. Moszyński, N. Guskos, B. Ohtani, A.W. Morawski, Preparation of photoactive nitrogen-doped rutile, *Appl. Surf. Sci.* 266 (2013) 410–419.
- [242] V. Etacheri, M.K. Seery, S.J. Hinder, S.C. Pillai, Oxygen rich titania: a dopant free, high temperature stable, and visible-light active anatase photocatalyst, *Adv. Funct. Mater.* 21 (2011) 3744–3752.
- [243] Y.M. Chiang, D.P. Birnie III, W.D. Kingery, *Physical Ceramics—Principles for Ceramic Science and Engineering*, John Wiley & Sons Inc., New York, 1997.
- [244] Y. Kuroda, T. Mori, K. Yagi, N. Makihata, Y. Kawahara, M. Nagao, S. Kittaka, Preparation of visible-light-responsive TiO_{2-x}N_x photocatalyst by a sol-gel method: analysis of the active center on TiO₂ that reacts with NH₃, *Langmuir* 21 (2005) 8026–8034.

- [245] V. Žunič, M. Vukomanović, S.D. Škapin, D. Suvorov, J. Kovač, Photocatalytic properties of TiO₂ and TiO₂/Pt: a sol-precipitation sonochemical and hydrothermal approach, *Ultrason. Sonochem.* 21 (2014) 367–375.
- [246] D.C.L. Vasconcelos, V.C. Costa, E.H.M. Nunes, A.C.S. Sabioni, M. Gasparon, W. L. Vasconcelos, Infrared spectroscopy of titania sol-gel coatings on 316 L stainless steel, *Mater. Sci. Appl.* 2 (2011) 1375–1382.
- [247] B. Das, R.G. Nair, B. Rajbongshi, S.K. Samdarshi, Investigation of the photoactivity of pristine and mixed phase N-doped titania under visible and solar irradiation, *Mater. Charact.* 83 (2013) 145–151.
- [248] B. Stuart, *Infrared Spectroscopy: Fundamentals and Applications*, John Wiley & Sons Ltd., Chichester, England, 2004.
- [249] E. Pretsch, P. Buhlmann, C. Affolter, *Structure Determination of organic compounds*, Springer-Verlag, Berlin Heidelberg New York, 2000.
- [250] M.J. Velasco, F. Rubio, J. Rubio, J.L. Oteo, DSC and FT-IR analysis of the drying process of titanium alkoxide derived precipitates, *Thermochim. Acta* 326 (1999) 91–97.
- [251] J. Xu, W.L. Dai, J. Li, Y. Cao, H. Li, H. He, K. Fan, Simple fabrication of thermally stable aperture N-doped TiO₂ microtubes as a highly efficient photocatalyst under visible light irradiation, *Catal. Commun.* 9 (2008) 146–152.
- [252] H. Li, J. Li, Y. Huo, Highly active TiO₂N photocatalysts prepared by treating TiO₂ precursors in NH₃/Ethanol fluid under supercritical conditions, *J. Phys. Chem. B* 110 (2006) 1559–1565
- [253] S.T. Hussain, K. Khan, R. Hussain, Size control synthesis of sulfur doped titanium dioxide (anatase) nanoparticles, its optical property and its photocatalytic reactivity for CO₂ + H₂O conversion and phenol degradation, *J. Nat. Gas. Chem.* 18 (2009) 383–391.
- [254] P.V.R.K. Ramacharyulu, D.B. Nimbalkar, J.P. Kumar, G.K. Prasad, S.-C. Ke, N-doped, S-doped TiO₂ nanocatalysts: synthesis, characterization and photocatalytic activity in the presence of sunlight, *RSC Adv.* 5 (2015) 37096-37101.
- [255] A. Fujishima, X. Zhang, D.A. Tryk, TiO₂ photocatalysis and related surface phenomena, *Surf. Sci. Rep.* 63 (2008) 515-582.

- [256] S. Liu, X. Chen, A visible light response TiO₂ photocatalyst realized by cationic S-doping and its application for phenol degradation, *J. Hazard. Mater.* 152 (2008) 48–55.

Curriculum Vitae

Date of birth: April 30, 1981.

Place of birth: Malta

1987-1992: Primary school. ‘Kadeja Alkbra’ in Zliten, Libya.

1993-1995: Elementary school, "Kadeja Alkbra" in Zliten, Libya.

1996-1998: High School. ‘Fatat Altahadi’ in Zliten, Libya.

1999-2003: Bachelor of Engineering. :University "Al-Mergib, Faculty of Engineering, Department for chemical engineering, Khoms, Libya/

2005-2009: Working as an assistant at El-Mergib University, Faculty of Engineering, Department of chemical engineering, Khoms, Libya

2010-2012: Master of Engineering. University of Belgrade, Faculty of Technology and Metallurgy. Supervised by Professor Rada. Master Dissertation: The investigation of titania photocatalysts efficiency in seawater.

2013-2017: PHD Study. University of Belgrade, Faculty of Technology and Metallurgy. Belgrade, Serbia

Published paper:

[1] A. Albrbar, V. Djokić, A. Bjelajac, J. Kovač, J. Ćirković, M. Mitrić, Dj. Janačković, R. Petrović, Visible-light active mesoporous, nanocrystalline N,S-doped and co-doped titania photocatalysts synthesized by non-hydrolytic sol-gel route, *Ceram. Int.* 42 (2016) 16718–16728.

[2] A. Albrbar, A. Bjelajac, V. Djokić, J. Miladinović, Dj. Janačković, R. Petrović, Photocatalytic efficiency of titania photocatalysts in saline waters, *J. Serb. Chem. Soc.* 79 (2014) 1127-1140.

[3] A. Albrbar, V. Djokić, A. Bjelajac, M. Mitrić, R. Petrović, Dj. Janačković, Influence of the solvent type on properties and photocatalytic activity of titania powders synthesized by the nonhydrolytic sol–gel process, Programme and the book of the abstracts of the 3rd Conference of the Serbian Society for Ceramic Materials, Belgrade, 2015, p.79.

Образац 5.

Изјава о ауторству

Име и презиме аутора _____ Asma Juma Albrbar _____

Број индекса _____ 4040/2013 _____

Изјављујем

да је докторска дисертација под насловом

“Синтеза и карактеризација наноструктурних фотокатализатора на бази азотом и сумпором допираног титан(IV)-оксида за разградњу загађујућих супстанци у води под дејством видљиве светлости” (Synthesis and characterization of nanostructured photocatalysts based on the nitrogen- and sulfur-doped titania for the water pollutants degradation under visible light)

- резултат сопственог истраживачког рада;
- да дисертација у целини ни у деловима није била предложена за стицање друге дипломе према студијским програмима других високошколских установа;
- да су резултати коректно наведени и
- да нисам кршио/ла ауторска права и користио/ла интелектуалну својину других лица.

Потпис аутора

У Београду, 12.09.2017.



Изјава о истоветности штампане и електронске верзије докторског рада

Име и презиме аутора Asma Juma Albrbar

Број индекса 4040/2013

Студијски програм Хемијско инжењерство

Наслов рада “Синтеза и карактеризација наноструктурних фотокатализатора на бази азотом и сумпором допираног титан(IV)-оксида за разградњу загађујућих супстанци у води под дејством видљиве светлости” (Synthesis and characterization of nanostructured photocatalysts based on the nitrogen- and sulfur-doped titania for the water pollutants degradation under visible light)

Ментор проф. Др Рада Петровић

Изјављујем да је штампана верзија мог докторског рада истоветна електронској верзији коју сам предао/ла ради похрањена у **Дигиталном репозиторијуму Универзитета у Београду**.

Дозвољавам да се објаве моји лични подаци везани за добијање академског назива доктора наука, као што су име и презиме, година и место рођења и датум одбране рада.

Ови лични подаци могу се објавити на мрежним страницама дигиталне библиотеке, у електронском каталогу и у публикацијама Универзитета у Београду.

Потпис аутора

У Београду, 12.09.2017.



Изјава о коришћењу

Овлашћујем Универзитетску библиотеку „Светозар Марковић“ да у Дигитални репозиторијум Универзитета у Београду унесе моју докторску дисертацију под насловом:

“Синтеза и карактеризација наноструктурних фотокатализатора на бази азотом и сумпором допираног титан(IV)-оксида за разградњу загађујућих супстанци у води под дејством видљиве светлости” (Synthesis and characterization of nanostructured photocatalysts based on the nitrogen- and sulfur-doped titania for the water pollutants degradation under visible light)

која је моје ауторско дело.

Дисертацију са свим прилозима предао/ла сам у електронском формату погодном за трајно архивирање.

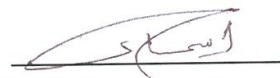
Моју докторску дисертацију похрањену у Дигиталном репозиторијуму Универзитета у Београду и доступну у отвореном приступу могу да користе сви који поштују одредбе садржане у одабраном типу лиценце Креативне заједнице (Creative Commons) за коју сам се одлучио/ла.

1. Ауторство (CC BY)
2. Ауторство – некомерцијално (CC BY-NC)
3. Ауторство – некомерцијално – без прерада (CC BY-NC-ND)
4. Ауторство – некомерцијално – делити под истим условима (CC BY-NC-SA)
5. Ауторство – без прерада (CC BY-ND)
6. Ауторство – делити под истим условима (CC BY-SA)

(Молимо да заокружите само једну од шест понуђених лиценци.
Кратак опис лиценци је саставни део ове изјаве).

Потпис аутора

У Београду, _____ 12.09.2017.



1. **Ауторство.** Дозвољава се умножавање, дистрибуцију и јавно саопштавање дела, и прераде, ако се наведе име аутора на начин одређен од стране аутора или даваоца лиценце, чак и у комерцијалне сврхе. Ово је најслободнија од свих лиценци.

2. **Ауторство – некомерцијално.** Дозвољава се умножавање, дистрибуцију и јавно саопштавање дела, и прераде, ако се наведе име аутора на начин одређен од стране аутора или даваоца лиценце. Ова лиценца не дозвољава комерцијалну употребу дела.

3. **Ауторство – некомерцијално – без прерада.** Дозвољава се умножавање, дистрибуцију и јавно саопштавање дела, без промена, преобликовања или употребе дела у свом делу, ако се наведе име аутора на начин одређен од стране аутора или даваоца лиценце. Ова лиценца не дозвољава комерцијалну употребу дела. У односу на све остале лиценце, овом лиценцом се ограничава највећи обим права коришћења дела.

4. **Ауторство – некомерцијално – делити под истим условима.** Дозвољава се умножавање, дистрибуцију и јавно саопштавање дела, и прераде, ако се наведе име аутора на начин одређен од стране аутора или даваоца лиценце и ако се прерада дистрибуира под истом или сличном лиценцом. Ова лиценца не дозвољава комерцијалну употребу дела и прерада.

5. **Ауторство – без прерада.** Дозвољава се умножавање, дистрибуцију и јавно саопштавање дела, без промена, преобликовања или употребе дела у свом делу, ако се наведе име аутора на начин одређен од стране аутора или даваоца лиценце. Ова лиценца дозвољава комерцијалну употребу дела.

6. **Ауторство – делити под истим условима.** Дозвољава се умножавање, дистрибуцију и јавно саопштавање дела, и прераде, ако се наведе име аутора на начин одређен од стране аутора или даваоца лиценце и ако се прерада дистрибуира под истом или сличном лиценцом. Ова лиценца дозвољава комерцијалну употребу дела и прерада. Слична је софтверским лиценцама, односно лиценцама отвореног кода.